UNIVERSITY OF CALIFORNIA,

IRVINE

Integrated Planar Optical Devices Based on Silicon Nitride Waveguides

DISSERTATION

submitted in partial satisfaction of the requirements

for the degree of

DOCTOR OF PHILOSOPHY

in Electrical and Computer Engineering

by

Qiancheng Zhao

Dissertation Committee:

Professor Ozdal Boyraz, Chair

Professor Payam Heydari

Professor Mohammad Al Faruque

2017

TABLE OF CONTENTS

LIST OF FIGURES

ACKNOWLEDGEMENTS

On the very outset of this dissertation, I would like to present my deepest gratitude to my advisor, Dr. Ozdal Boyraz, who supported me at every bit and without whom it is impossible for me to accomplish the end task. During the past five years, his erudition flourished my desire of knowledge; his intelligence inspired my work; and yet his trust and patience encouraged me to overcome every challenge. His edification not only guided me towards academic achievements in my Ph.D. study but also will help me for the rest of my life.

Besides my advisor, I would like to thank the rest of my thesis committee. It is an honor for me to have Dr. Payam Heydari and Dr. Mohammad Al Faruque in my committee, who provide invaluable opinion and suggestions to my research and dissertation.

My sincere thanks also go to my colleagues, Yuewang Huang, Salih Kagan Kalyoncu, Rasul Torun, Parinaz Sadri-Moshkenani, Mohammad Wahiduzzaman Khan, Imam-Uz Zaman, who helped me in many ways through my research and life in Irvine.

My wife, Mom, Dad, family members and friends, without whom I was nothing; they not only assisted me financially but also extended their support morally and emotionally.

Lastly, I offer my regards and blessings to all of those who supported me in any respect during the completion of this dissertation.

CURRICULUM VITAE

Qiancheng Zhao

EDUCATION

Doctor of Philosophy in Electrical and Computer Engineering **December 2017**
University of California, Irvine Irvine, California, USA

Master of Science in Electrical Engineering **June, 2014**
University of California, Irvine Irvine, California, USA

Bachelor of Science in Optical Engineering **June, 2012**
Zhejiang University Hangzhou, Zhejiang, China

RESEARCH EXPERIENCE

Optical Leaky Wave Antenna*:* experimentally demonstrate directive radiation from a silicon nitride (Si_3N_4) waveguide-based OLWA. Establish experimental setups and characterize the radiation beam angle, beam width, frequency dependence, and polarization effects.

Plasmonic Enhanced Radiation Defects Detection in Memory Cell: design surface patterns in the STT-RAM layer to enhance the plasmonic resonance, and investigate the optical readout in the far field domain to detect radiation-induced defects buried in the STT-RAM layers.

Silicon Nitride Trench Waveguide: fabricate the silicon nitride trench waveguides and characterize the propagation loss, nonlinear coefficient, dispersion parameters, and evanescent intensity ratio. Apply the trench waveguides in optomechanical trapping and waveguide nonlinearity enhancement with colloidal particles.

Plasmo-thermomechanical infrared detector*:* design and fabricate antennas that can absorb infrared energy and transduce into heat, causing the suspended wire temperature to increase. The thermo-mechanically actuated nanowires interact with the waveguide evanescent field and affect the waveguide output power.

PROFESSIONAL MEMBERSHIP

Student member of Institute of Electrical and Electronics Engineers (IEEE).

Student member of The Optical Society (OSA).

Student member of the Internal Society for Optical Engineering (SPIE).

PUBLICATIONS IN JOURNALS

[J11] **Qiancheng Zhao**, Parinaz Sadri-Moshkenani, Mohammad Wahiduzzaman Khan, Rasul Torun, and Ozdal Boyraz, "*On-Chip Bimetallic Plasmo-Thermomechanical Detectors for Mid-Infrared Radiation*," IEEE Photonics Technol. Lett., vol. 29, no. 17, pp. 1459–1462, Sep. 2017.

[J10] **Qiancheng Zhao**, Caner Guclu, Yuewang Huang, Filippo Capolino, and Ozdal Boyraz. "*Experimental Demonstration of Directive Si 3 N 4 Optical Leaky Wave Antennas with Semiconductor Perturbations*." Journal of Lightwave Technology 34, no. 21 (2016).

[J9] **Qiancheng Zhao**, Yuewang Huang, and Ozdal Boyraz, "*Optical properties of V-groove silicon nitride trench waveguides*," J. Opt. Soc. Am. A 33, 1851-1859 (2016).

[J8] **Qiancheng Zhao**, Caner Guclu, Yuewang Huang, Filippo Capolino, Regina Ragan, and Ozdal Boyraz. "*Plasmon optical trapping using silicon nitride trench waveguides*." JOSA B 33, no. 6 (2016): 1182-1189.

[J7] Yuewang Huang, **Qiancheng Zhao**, Salih K. Kalyoncu, Rasul Torun, and Ozdal Boyraz. "*Silicon-on-sapphire mid-IR wavefront engineering by using subwavelength grating metasurfaces*." JOSA B 33, no. 2 (2016): 189-194.

[J6] Shah Rahman, Rasul Torun, **Qiancheng Zhao**, and Ozdal Boyraz, "*Electronic control of optical tweezers using space-time-wavelength mapping*," J. Opt. Soc. Am. B 33, 313-319 (2016).

[J5] Y. Huang**, Q. Zhao**, L. Kamyab, A. Rostami, F. Capolino, and O. Boyraz, "*Sub-micron silicon nitride waveguide fabrication using conventional optical lithography*," Opt. Express 23, 6780-6786 (2015).

[J4] Huang, Yuewang**, Qiancheng Zhao**, Salih K. Kalyoncu, Rasul Torun, Yumeng Lu, Filippo Capolino, and Ozdal Boyraz. "*Phase-gradient gap-plasmon metasurface based blazed grating for real time dispersive imaging*." Applied Physics Letters 104, no. 16 (2014): 161106.

[J3] Huang, Yuewang, Salih K. Kalyoncu, **Qiancheng Zhao**, Rasul Torun, and Ozdal Boyraz. "*Silicon-on-sapphire waveguides design for mid-IR evanescent field absorption gas sensors*." Optics Communications 313 (2014): 186-194.

[J2] Kalyoncu, Salih K., Rasul Torun, Yuewang Huang, **Qiancheng Zhao**, and Ozdal Boyraz. "*Fast Dispersive Laser Scanner by Using Digital Micro Mirror Arrays*." Journal of Micro and Nano-Manufacturing 2, no. 2 (2014): 021004

[J1] LIN, Fu-Chun, Xu-Xia WANG, **Qian-Cheng ZHAO**, and Hao LEI. "Templates and Analysis Methods for Small Animal High-resolution Diffusion Magnetic Resonance Imaging." Progress in Biochemistry and Biophysics 6 (2012): 005.

PUBLICATIONS IN CONFERENCES

[C16] Parinaz Sadri-Moshkenani, Mohammad Wahiduzzaman Khan, **Qiancheng Zhao**, Ilya Krivorotov, Mikael Nilsson, Nader Bagherzadeh, Ozdal Boyraz, "*Plasmonic detection of possible defects in multilayer nanohole array consisting of essential materials in simplified STT-RAM cell*," Proc. SPIE 10346, Plasmonics: Design, Materials, Fabrication, Characterization, and Applications XV, 1034639, 2017

[C15] **Qiancheng Zhao**, Mohammad Wahiduzzaman Khan, Parinaz Sadri-Moshkenani, Rasul Torun, Imam-Uz Zaman, and Ozdal Boyraz. "*Plasmo-thermomechanical suspended nanowire array detectors for mid-infrared spectrum*." In Infrared Sensors, Devices, and Applications VII, vol. 10404, p. 104040L. International Society for Optics and Photonics, 2017.

[C14] **Qiancheng Zhao**, Parinaz Sadri-Moshkenani, Mohammad Wahiduzzaman Khan, Rasul Torun, Iman-Uz Zaman, and Ozdal Boyraz, "*Infrared Detection Using Plasmonically Enhanced Thermomechanically Actuated Nanowire Arrays*," in Conference on Lasers and Electro-Optics, OSA Technical Digest (online) (Optical Society of America, 2017), paper JTh2A.114.

[C13] **Qiancheng Zhao**, Mohsen Rajaei, and Ozdal Boyraz, "*Silicon Nitride on Silicon-on-Insulator: a Platform for Integration Active Control over Passive Components*," in Conference on Lasers and Electro-Optics, OSA Technical Digest (online) (Optical Society of America, 2016), paper JW2A.125.

[C12] **Qiancheng Zhao**, Mohsen Rajaei, Ilya Krivorotov, Mikael Nilsson, Nader Bagherzadeh, and Ozdal Boyraz, "*Optical Investigation of Radiation Induced Conductivity Changes in STT-RAM Cells*," in Conference on Lasers and Electro-Optics, OSA Technical Digest (online) (Optical Society of America, 2016), paper FM3B.2.

[C11] **Qiancheng Zhao,** Yuewang Huang, Rasul Torun, Shah Rahman, Tuva C. Atasever, and Ozdal Boyraz. "*Numerical investigation of silicon nitride trench waveguide*." In SPIE Optical Engineering+ Applications, pp. 95860O-95860O. International Society for Optics and Photonics, 2015.

[C10] **Qiancheng Zhao**, Yuewang Huang, Caner Guclu, Filippo Capolino, and Ozdal Boyraz. "*Optical Leaky Wave Antenna Experiment Demonstration and Electronic Modulation Investigation*." In CLEO: Science and Innovations, pp. JTh2A-43. Optical Society of America, 2015.

[C9] **Qiancheng Zhao**, Caner Guclu, Yuewang Huang, Filippo Capolino, and Ozdal Boyraz. "*Plasmon Optical Trapping in Silicon Nitride Trench Waveguide*." In CLEO: Science and Innovations, pp. JTu5A-80. Optical Society of America, 2015.

[C8] **Qiancheng Zhao**, Caner Guclu, Yuwang Huang, Salvatore Campione, Filippo Capolino, and Ozdal Boyraz. "*Experimental demonstration of directive Si3N4 optical leaky wave antennas with semiconductor perturbations at near infrared frequencies*." In SPIE OPTO, pp. 93651K-93651K. International Society for Optics and Photonics, 2015.

[C7] Yuewang Huang, **Qiancheng Zhao**, Nicholas Sharac, Regina Ragan, and Ozdal Boyraz. "*Highly nonlinear sub-micron silicon nitride trench waveguide coated with gold nanoparticles*." In SPIE Optics+ Optoelectronics, pp. 95030H-95030H. International Society for Optics and Photonics, 2015.

[C6] Shah Rahman, Rasul Torun, **Qiancheng Zhao**, Tuva Atasever, and Ozdal Boyraz. "*Electronically-controlled optical tweezing using space-time-wavelength mapping*." In SPIE Optical Engineering+ Applications, pp. 95810E-95810E. International Society for Optics and Photonics, 2015.

[C5] Ozdal Boyraz, **Qiancheng Zhao**, Caner Guclu, Filippo Capolino, and Regina Ragan, "Silicon Nitride Waveguides for Plasmon Optical Trapping and Sensing Application," Progress In Electromagnetics Research Symposium, PIERS 2015 Conference, July 2015, Prague, Czech republic (Invited).

[C4] Y. Huang, **Q. Zhao**, L. Kamyab, A. Rostami, F. Capolino, and O. Boyraz, "*Sub-micron silicon nitride waveguide fabrication using conventional optical lithography*," in Advanced Photonics for Communications, OSA Technical Digest (online) (Optical Society of America, 2014), p. JT3A.27.

[C3] Y. Huang, **Q. Zhao**, K. Salih, R. Torun, Y. Lu, F. Capolino, and O. Boyraz, " Phase-gradient gap-plasmon metasurface based blazed grating for real time dispersive imaging," CLEO 2014 conference, CLEO: STu1M.7, 2014.

[C2] Huang, Yuewang, Shiming Gao, Salih K. Kalyoncu, En-kuang Tien, Qi Song, **Qiancheng Zhao**, Rasul Torun, and Ozdal Boyraz. "*Wavelength conversion bandwidth enhancement through quasi-phase-matching in a width modulated silicon waveguide*." In Optical Fiber Communication Conference, pp. JTh2A-33. Optical Society of America, 2013.

[C1] S. K. Kalyoncu, Y. Huang, R. Torun, **Q. Zhao**, and O. Boyraz, "Fast Dispersive Laser Scanner by Using Digital Micro Mirror Arrays," in CLEO: 2013, OSA Technical Digest (online) (Optical Society of America, 2013), paper JTu4A.30.

AWARDS

Student Travel Grant. 2016

Broadcom Fellowship (an industry fellowship to award engineering students for research). 2014

Fellowship in Department of Electrical Engineering and Computer Science, UC, Irvine. 2012

National Fellowship (The Ministry of Education of the People's Republic of China). 2009

ABSTRACT OF THE DISSERTATION

Integrated Planar Optical Devices Based on Silicon Nitride Waveguides

By

Qiancheng Zhao

Doctor of Philosophy in Electrical and Computer Engineering

University of California, Irvine, 2017

Professor Ozdal Boyraz, Chair

Silicon nitride is a subject of growing interest with the potential of delivering planar integrated optical devices as a complementary part of silicon photonics. The material has a moderate refractive index, wide optical transparency window, lack of two-photon absorption, and low nonlinear susceptibility. Thanks to its CMOS fabrication compatibility, the freedom of integrating different materials into Si_3N_4 renders the platform omnipotent. This dissertation is dedicated to developing Si_3N_4 based optical devices integrated with Si nanowires, fishbone antennas, bowtie antennas and gold nanoparticles to achieve active and passive optical functionalities. To be specific, the thesis covers Si_3N_4 based optical leaky wave antennas that emit narrow beams towards desired directions in free space, bimetallic fishbone waveguide-based detectors that detect optical radiations plasmonically and thermo-mechanically, and trench waveguides that can be equipped with bowtie antennas for optical trapping or with gold nanoparticles for nonlinearity enhancement.

The purpose of the first part of the dissertation is to experimentally demonstrate emission from a leaky wave antenna and to investigate the possible modulation method in tuning the radiation beam. The optical leaky wave antenna is composed of a Si_3N_4 waveguide and periodic Si nanowires. The antenna has a single directive radiation peak at the angle of 85.1° in the measured range from 65° to 112° at the wavelength of 1550 nm. The side lobes are at least 7 dB lower than the main peak. The peak radiation angle moves to the broad side as the wavelength increases. The device can find promising applications in optical communications, especially for multi-wavelength space division multiplexing owing to its capability of beam scanning with frequency. The study on the optical leaky wave antenna proves the functionality of off-plane emission from a waveguide and explores the potential electronic modulation methods.

The second part of the dissertation presents a plasmo-thermomechanical radiation detector. The goal of the second work is to investigate if thermomechanical vibrations can be detected in an on-chip optical readout system. To study the problem, I designed a device that is composed of a Si_3N_4 waveguide and 13 fishbone nanowires suspended above the waveguide. Each wire is 12.54 μm long and consists of 16 nanoantennas with a period of 660 nm. Under the illumination of 660 nm light, the detector shows a responsivity of 3.954×10^{-3} $\mu m^2/\mu W$. The noise equivalent power, dominated by the waveguide coupling instability, is 3.01 $\mu W/\sqrt{Hz}$. The 3dB bandwidth of the device is 9.6 Hz corresponding to a time constant of 16.6 ms. Besides the demonstrated radiation detector for visible wavelength, another device for mid-infrared wavelength has also been designed and optimized for fabrication. This study verifies the possibility of using on-chip waveguide-based readout system to detect the mechanical vibration that is induced by radiation.

The third part of the dissertation focuses on Si_3N_4 trench waveguides. The objective of this part is to thoroughly explore the optical properties of the trench waveguides and investigate their applications. The trench waveguide shape is determined by the silicon wet etching properties and thus can be controlled in either triangle or trapezoidal shape. Experimental results show that the propagation loss of the TM mode can be as low as 0.8 dB/cm. The nonlinear parameter of the waveguide is measured to be 0.3 W^{-1}/m. Coating gold nanoparticles can enhance the waveguide nonlinearity. The trench waveguide is promising for liquid sensing thanks to its unique structure that can combine fluidic channel and waveguide together. Explorations on the trapezoidal trench waveguide and bowtie antennas also show that the platform is suitable for trapping nanoparticles. Switching between trapping and releasing the particles can be done by changing the mode polarization states from the TE mode to the TM mode. This work provides an in-depth study of the trench waveguides from optical properties, fabrication, to applications.

This study expands the knowledge and capabilities of conventional silicon photonics and paves way for novel devices pertinent to communications and sensing. In particular, this thesis shows that the use of Si_3N_4 based planar optical circuits, the operational bandwidth of silicon photonics can cover wavelengths shorter than $1.1\mu m$ for novel applications. The presented work on new optical planar emitters, waveguides, detectors, optical trapping, and microfluidics at wavelengths from visible to mid-wave infrared will be beneficial to both future research and industry applications.

Chapter 1

Introduction

1.1 Introduction

Ever since Stewart E. Miller first developed the field of integrated photonics in 1969 [1], the photonic circuitry has expanded substantially. However, the number of the optical components per photonic integrated circuits has not grown as fast as its microelectronic counterparts in the first three decades of the field. However, the developments in the field have been accelerated in the past twenty years because of the incessant demands for fast Internet traffic and the slowdown of Moore's Law, which states that the number of transistors in a dense integrated circuit doubles approximately every two years. During the past two decades, tremendous progress has been made in photonic integrated circuits, as researchers started refocusing on this technology as an alternative for electrical components to continue the rapid evolution of communications [2]. Owing to the advantages of CMOS-compatibility, large-scale fabrication and availability of sophisticated assembly processes, silicon (Si) photonics has become one of the most promising candidates for the next generation of communication technology. These advantages, coupled with the high refractive index contrast in Si photonics platforms, enable the commercialization [3] of densely integrated electro-photonic devices due to their small footprints, large volume production, and thus low cost [4].

Despite the fabrication convenience of Si photonics, Si the material itself suffers some drawbacks, e.g., losses, nonlinearity, opaqueness at short wavelengths, and fabrication

tolerance, which challenge the development of the platform. Thus, Si-based materials have mostly been investigated as a supplement. Silicon nitride (Si_3N_4) is also a CMOS-compatible material with moderate refractive index and superior optical properties to Si, which makes it niche for optical passive devices. Since the first demonstration of waveguiding in Si_3N_4 films on a SiO_2 buffer on Si wafers in 1977 [5], many Si_3N_4 optical components have been developed and characterized in the period before Millennium [6]–[11]. Interest in the Si_3N_4 material continued to thrive when near-infrared (NIR) applications were demonstrated by Sandia Labs (USA) [12] and the University of Trento (ITA) [13] in 2005, a development which was followed by several works focused on optimizations of fabrication recipes [14] and waveguide geometries [15], pushing the waveguide propagation loss below 0.1 dB/cm at NIR C-band [16]. In the meantime, development at visible [17], [18] and mid-infrared wavelengths [16] have also been on-going. In recent years, research interest in Si_3N_4 has shifted to multilayer integration and 3D photonics to include silicon-on-insulator (SOI) devices on the same chip [20]–[25].

The interest in using Si_3N_4 material for photonics lies in but is not limited to the following reasons: (i) the high optical transparency window enabling applications in both visible and infrared spectrums; (ii) the lack of the two photon absorption and low nonlinear susceptibility $\chi^{(3)}$ [26] making Si_3N_4 ideal for high power applications; (iii) the small thermo-optic coefficient rendering it robust against temperature changes [27]; (iv) the moderate refractive index between Si and SiO_2 guaranteeing tight mode confinement and less scattering loss at the same time; (v) the low refractive index contrast (compared with Si to SiO_2) equipping the resulting devices with tolerance to fabrication errors; and (vi)

CMOS-compatibility that can realize the integration of Si_3N_4, Si, SiO_2 and even metals all in one platform.

Among all the reasons mentioned above, it is the last reason that makes Si_3N_4 platform omnipotent. Thanks to the Si fabrication process, the freedom of integrating different materials into Si_3N_4 platform gives the platform a power to have functionalities that passive optical devices cannot possess. Motivated by past studies and a curiosity to exploit the frontier of the Si_3N_4 platform, this dissertation is dedicated to developing Si_3N_4 based optical devices that can include other materials, e.g., Si nanowire, fishbone metal antenna, bowtie antennas and gold nanoparticles. To be specific, the thesis covers silicon-based optical leaky wave antennas that can emit radiations like vertical-external-cavity surface-emitting-laser (VECSEL), metallic fishbone waveguide-based detectors that detect optical radiations plasmo-thermomechanically, and trench waveguides that can be equipped with bowtie antennas for optical trapping or with gold nanoparticles for nonlinearity enhancement. The author hopes to help carry forward Si_3N_4 platform and Si photonics by contributing a relatively tiny effort to the expanding human knowledge.

1.2 Organization of the Dissertation

The dissertation is organized as follows. Chapter 1 presents a brief introduction to Si_3N_4 photonic platforms and the objective of this research. Chapter 2 lays down the background of electromagnetics and wave optics, including Maxwell's equations, wave equation, wave guiding in dielectric slabs, skin-effect and photo-thermal effect. In Chapter 3, a Si-based optical leaky wave antenna is presented. The optical leaky wave antenna is composed of a Si_3N_4 waveguide and an array of Si nanowires. Both the theoretical modeling and fabrication procedure are given in this chapter. The optical leaky wave antenna can emit

light vertically into space. Its radiation pattern is experimentally characterized. The potential modulation method on the radiation pattern is also investigated. In Chapter 4, a plasmo-thermomechanical radiation detector is demonstrated. The detector is composed of a Si_3N_4 waveguide with suspended fishbone nanowire array that is made of Au and Ni. Both mechanical modeling and electromagnetic modeling are given, along with the fabrication procedures. The experiment results are also presented in this chapter. Chapter 5 covers Si_3N_4 trench waveguides. The trench waveguide has a different cross-section from a regular waveguide. It has the inborn advantage of combining microfluidics and optics together. Its optical properties, including mode distribution, waveguide nonlinearity, evanescent intensity ratio, and dispersion are thoroughly analyzed in this chapter. Experimental results of the waveguide propagation loss and nonlinear parameters are presented. Two applications of the trench waveguide have been investigated, including the waveguide nonlinearity enhancement and optical trapping. The dissertation ends with a general conclusion of the all the works and a discussion of possible future research directions.

Chapter 2

Fundamentals of Electromagnetics and Waveguide Optics

2.1 Maxwell's Equations

The electromagnetic theory is described by Maxwell's equations that were published in 1873 [28]. The differential forms of Maxwell's equations in SI unit are summarized in equations (2.1.1) through (2.1.4):

$$\nabla \times \vec{E} + \frac{\partial \vec{B}}{\partial t} = 0 \qquad \text{(Faraday's law)} \qquad (2.1.1)$$

$$\nabla \times \vec{H} = \vec{J} + \frac{\partial \vec{D}}{\partial t} \qquad \text{(Ampere's law)} \qquad (2.1.2)$$

$$\nabla \cdot \vec{D} = \rho \qquad \text{(Gauss's law)} \qquad (2.1.3)$$

$$\nabla \cdot \vec{B} = 0 \qquad \text{(Gauss's law for magnetic)} \qquad (2.1.4)$$

where $\vec{E}$ is the electric field intensity (V/m), $\vec{H}$ is the magnetic field intensity (A/m) and can be expressed as:

$$\vec{H} = \frac{\vec{B}}{\mu_0} - \vec{M} \qquad (2.1.5)$$

where $\vec{M}$ is the magnetization density (A/m), $\vec{B}$ is the magnetic flux intensity (Wb/m^2), $\vec{J}$ is the current density (A/m^2), ρ is the charge density (C/m^3), $\vec{D}$ is the electric flux density (C/m^2) and is related with $\vec{E}$ is the following way:

$$\vec{D} = \varepsilon_0 \vec{E} + \vec{P} \qquad (2.1.6)$$

where $\vec{P}$ is the electric polarization density (C/m^2), ε_0 is the permittivity of free space (8.85

× 10^{-12} F/m), and μ_0 is the permeability of free space (4π ×10^{-7} H/m).

Electromagnetic fields are derived from the presence of charges and the movement of charge, so $\vec{J}$ and ρ are the ultimate sources that induce the electric and magnetic fields. The magnetization density $\vec{M}$, however, does not exist in nature, as it is a mere mathematical convenience [29]. The above equations are derived in a vacuum condition. To describe the electromagnetic properties of general materials, equations (2.1.1) through (2.1.6) must be supplemented with relations that comprehend the properties of media other than free space.

$$\vec{J} = \sigma \vec{E} \tag{2.1.7}$$

$$\vec{B} = \mu_r \mu_0 \vec{H} = \mu \vec{H} \tag{2.1.8}$$

$$\vec{P} = \varepsilon_0 (\varepsilon_r - 1) \vec{E} \tag{2.1.9}$$

where σ is the conductivity of the medium (S/m), μ_r is the relative permeability, and ε_r is the relative permittivity. Both μ_r and ε_r are unitless quantities.

2.2 Wave Equation

It is apparent that Faraday's law and Ampere's law are coupled in a way that a changing magnetic field will produce an electric field, and a changing electric field will produce a magnetic field. Combining the two laws yields the wave equation which is the key to solve Maxwell's equations. Taking the curl of the Faraday's law produces

$$\nabla \times \left(\nabla \times \vec{E} \right) = -\nabla \times \frac{\partial \vec{B}}{\partial t} \tag{2.2.1}$$

Since $\vec{B} = \mu\vec{H}$ and $\vec{H}$ can be derived from $\vec{E}$ using Ampere's law, mathematics tricks can be applied to eliminate magnetic components from the right side of equation (2.2.1):

$$-\nabla\times\frac{\partial\vec{B}}{\partial t} = -\frac{\partial\left(\nabla\times\mu\vec{H}\right)}{\partial t} = -\mu\frac{\partial}{\partial t}\left(\vec{J}+\frac{\partial\vec{D}}{\partial t}\right) \tag{2.2.2}$$

If the region of wave propagation is assumed source free, in other words, $\vec{J}$ is zero, then combining equation (2.2.2) and (2.2.1) allows the equations to be express only in terms of $\vec{E}$:

$$\nabla\times\left(\nabla\times\vec{E}\right) = -\mu\varepsilon\frac{\partial^2\vec{E}}{\partial^2 t} \tag{2.2.3}$$

Using the vector identity $\nabla\times\left(\nabla\times\vec{E}\right) = \nabla\left(\nabla\cdot\vec{E}\right) - \nabla^2\vec{E}$ and Gauss's law $\nabla\cdot\vec{E} = 0$ in a source-free medium, the wave equation for the electric field is expressed as:

$$\nabla^2\vec{E} - \mu\varepsilon\frac{\partial^2\vec{E}}{\partial t^2} = 0 \tag{2.2.4}$$

Similarly, the wave equation for the magnetic field is

$$\nabla^2\vec{H} - \varepsilon\mu\frac{\partial^2\vec{H}}{\partial t^2} = 0 \tag{2.2.5}$$

2.3 Energy Density and Poynting Vector

The energy density and the power flow carried by electromagnetic waves can be derived by calculating the energy dissipation per unit volume $\vec{J}\cdot\vec{E}$. According to Ampere's law, the work done by the electromagnetic wave is

$$\vec{J}\cdot\vec{E} = \vec{E}\cdot\left(\nabla\times\vec{H}\right) - \vec{E}\cdot\frac{\partial\vec{D}}{\partial t} \tag{2.3.1}$$

Employing the vector identity $\nabla \cdot \left(\vec{E} \times \vec{H} \right) = \vec{H} \cdot \left(\nabla \times \vec{E} \right) - \vec{E} \cdot \left(\nabla \times \vec{H} \right)$ and Faraday's law, the right side of the equation (2.3.1) then becomes

$$\vec{J} \cdot \vec{E} = -\nabla \cdot \left(\vec{E} \times \vec{H} \right) - \vec{H} \cdot \frac{\partial \vec{B}}{\partial t} - \vec{E} \cdot \frac{\partial \vec{D}}{\partial t} \tag{2.3.2}$$

Rearranging the above equation shows

$$\frac{\partial U}{\partial t} + \nabla \cdot \vec{S} = -\vec{J} \cdot \vec{E} \tag{2.3.3}$$

where U and $\vec{S}$ are defined as:

$$U = W_e + W_m \tag{2.3.4}$$

$$W_e = \frac{1}{2} \vec{E} \cdot \vec{D} = \frac{1}{2} \varepsilon E^2 \tag{2.3.5}$$

$$W_m = \frac{1}{2} \vec{B} \cdot \vec{H} = \frac{B^2}{2\mu} \tag{2.3.6}$$

$$\vec{S} = \vec{E} \times \vec{H} \tag{2.3.7}$$

The scalar U (joules/m^3) represents the energy density of the electromagnetic field and it is composed of the energy density stored in electric field W_e and energy density stored in magnetic field W_m. The vector $\vec{S}$ (joules/m^{2}s), representing the energy flux, is called the Poynting vector [30].

2.4 Time-Harmonic Fields and Wave Propagation

A simplification of Maxwell's equations can be made if the time variation is assumed to be steady-state sinusoidal or time-harmonic in nature. According to Euler's formula, a sinusoidal waveform can be represented as

$$\cos\phi + i\sin\phi = e^{i\phi} \tag{2.4.1}$$

so the sinusoidal form of a time-harmonic field will vary according to the complex exponential factor $e^{i\omega t}$, leading to a separation of Maxwell's equations in space and time domain:

$$\vec{E}(x,y,z,t) = \vec{E}(x,y,z)e^{i\omega t} \tag{2.4.2}$$

$$\vec{B}(x,y,z,t) = \vec{B}(x,y,z)e^{i\omega t} \tag{2.4.3}$$

After substituting equations (2.4.2) and (2.4.3) into Maxwell's equations and canceling the $e^{i\omega t}$ term, the time-harmonic form of Maxwell's equations is shown:

$$\nabla\times\vec{E} + i\omega\vec{B} = 0 \tag{2.4.4}$$

$$\nabla\times\vec{H} = \vec{J} + i\omega\vec{D} \tag{2.4.5}$$

$$\nabla\cdot\vec{D} = \rho \tag{2.4.6}$$

$$\nabla\cdot\vec{B} = 0 \tag{2.4.7}$$

The wave equations can also be expressed in a time-harmonic fashion by substituting $\partial/\partial t$ with $i\omega$.

$$\nabla^2\vec{E} + \omega^2\mu\varepsilon\vec{E} = 0 \tag{2.4.8}$$

$$\nabla^2\vec{H} + \omega^2\mu\varepsilon\vec{H} = 0 \tag{2.4.9}$$

Here $\omega^2\mu\varepsilon$ can be represented by a term named propagation constant γ:

$$\gamma^2 = -\omega^2\mu\varepsilon \tag{2.4.10}$$

$$\gamma = \alpha + i\beta \tag{2.4.11}$$

where α is the attenuation constant and β is the phase constant. In a lossless medium, $\alpha = 0$

and $\beta = \sqrt{\omega^2 \mu\varepsilon} = \sqrt{\mu_r \varepsilon_r} \cdot \sqrt{\omega^2 \mu_0 \varepsilon_0} = n \cdot 2\pi f \sqrt{\mu_0 \varepsilon_0}$, where n is the refractive index of the medium. Since the speed of light $c \equiv 1/\sqrt{\mu_0 \varepsilon_0}$ and the wavelength in vacuum is $\lambda = f / c$, thus the phase constant can also be expressed as

$$\beta = \frac{2\pi n}{\lambda} \tag{2.4.12}$$

when $n = 1$ the phase constant is the same as the magnitude of the wavevector $\left|\vec{k}\right|$.

2.5 Transverse Helmholtz Equation

The wave equations (2.4.8) and (2.4.9) have six components in a three-dimension space. They can be represented by a unified scalar Helmholtz equation:

$$\nabla^2 \phi(x, y, z) + \omega^2 \mu\varepsilon \phi(x, y, z) = 0 \tag{2.5.1}$$

where ϕ stands for any component from E_x, E_y, E_z, H_x, H_y, and H_z.

Assume $\phi(x, y, z) = \psi(x)\eta(y)\varsigma(z)$ and apply the method of the separation of the variables to the above equation:

$$\frac{1}{\psi(x)} \frac{\partial^2 \psi(x)}{\partial x^2} + \frac{1}{\eta(y)} \frac{\partial^2 \eta(y)}{\partial y^2} + \frac{1}{\varsigma(z)} \frac{\partial^2 \varsigma(z)}{\partial z^2} + \omega^2 \mu\varepsilon = 0 \tag{2.5.2}$$

$$\frac{1}{\eta(y)} \frac{\partial^2 \eta(y)}{\partial y^2} = -k_y^2 \tag{2.5.3}$$

$$\frac{1}{\varsigma(z)} \frac{\partial^2 \varsigma(z)}{\partial z^2} = -k_z^2 \tag{2.5.4}$$

where k_y and k_z are the y and z components of the wave vector $\vec{k}$, respectively. The solutions to equations (2.5.3) and (2.5.4) predict that $\eta(y) \propto \exp(-ik_y y)$ and $\varsigma(z) \propto \exp(-ik_z z)$, thus, $\phi(x, y, z)$ can be expressed as:

$$\phi(x, y, z) = \psi(x)\exp(-ik_y y - ik_z z) \tag{2.5.5}$$

The Helmholtz equation then becomes

$$\frac{\partial^2}{\partial x^2}\psi(x) + (\omega^2 \mu\varepsilon - k_y^2 - k_z^2)\psi(x) = 0 \tag{2.5.6}$$

If the wave travels along the z-axis, then $k_y = 0$ and $k_z = \beta_{eff}$. It is worth noting that β_{eff} is the effective propagation constant, but may not necessarily equal $\omega\sqrt{\mu\varepsilon}$, especially in waveguides. Now the transverse Helmholtz equation is

$$\frac{\partial^2}{\partial x^2}\psi(x) + (\omega^2 \mu\varepsilon - \beta_{eff}^2)\psi(x) = 0 \tag{2.5.7}$$

2.6 Wave Propagation in Confined Dielectric Medium

The wave propagation in free space has been discussed in the above sessions. Due to diffraction, light with a finite cross section will spread as it propagates in free space. High refractive index medium can be used to confine the beam. The modes of the confined propagation are the guided waves or guided modes, and the structures that support guided waves are called waveguides.

Dielectric slabs are among the simplest optical waveguides. They are usually composed of a core layer with a higher refractive index and two cladding layers with lower refractive indices. The core layer is sandwiched between the cladding layers and it is thin. Compared

to the core layer, the cladding layers can be viewed as semi-infinite. The structure of a three-layer slab waveguide is demonstrated in Figure 2-1.

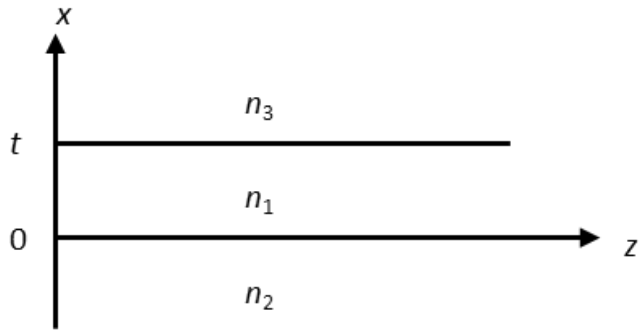

Figure 2-1. Schematic Drawing of a slab waveguide. The waveguide consists of a guiding layer of thickness t with a refractive index of n_1, surrounded by top and bottom cladding medium with refractive indices of n_3 and n_2, respectively.

Here we assume $n_1 > n_2 > n_3$, indicating this is an asymmetric waveguide. When $n_2 = n_3$, the waveguide becomes symmetric. The transverse electric (TE) mode is defined as its electric field is not in the direction of propagation. To be specific, a TE mode has its electric components only in the y-direction. Likewise, a transverse magnetic (TM) mode has its magnetic components only in the y-direction. The field distribution in the three-layer slab waveguide can be generated from Ref. [31]:

$$\psi(x) = \begin{cases} A\exp(qx) & (-\infty < x \le 0) \\ A\left[\cos(hx) + T_2 \sin(hx)\right] & (0 \le x < t) \\ A\left[\cos(hx) + T_2 \sin(hx)\right] \cdot \exp\left[-p(x-t)\right] & (t < x < \infty) \end{cases} \tag{2.6.1}$$

where $\psi(x) = E_y(x)$ for TE mode, and $\psi(x) = H_y(x)$ for TM mode, $q = \sqrt{\beta^2 - n_2^2 k_0^2}$, $h = \sqrt{k_0^2 n_1^2 - \beta^2}$, $p = \sqrt{\beta^2 - n_3^2 k_0^2}$, and

$$T_2 = \left(\frac{n_1}{n_2}\right)^{2s} \cdot \frac{q}{h} \tag{2.6.2}$$

$$T_3 = \left(\frac{n_1}{n_3}\right)^{2s} \cdot \frac{p}{h} \tag{2.6.3}$$

For TE mode s = 0, and for TM mode s = 1. These parameters satisfy the following equation:

$$\tan(ht) = \frac{T_2 + T_3}{1 - T_2 T_3} \tag{2.6.4}$$

Equation (2.6.4) can be written in another format that takes the mode order into consideration:

$$ht = m\pi + \arctan T_2 + \arctan T_3 \tag{2.6.5}$$

where m is the mode order, and $m = 0,1,2\ldots$ Using the equations (2.6.1) through (2.6.5), the effective mode refractive index can be simulated and plotted as a function of the material refractive indices and the waveguide structure.

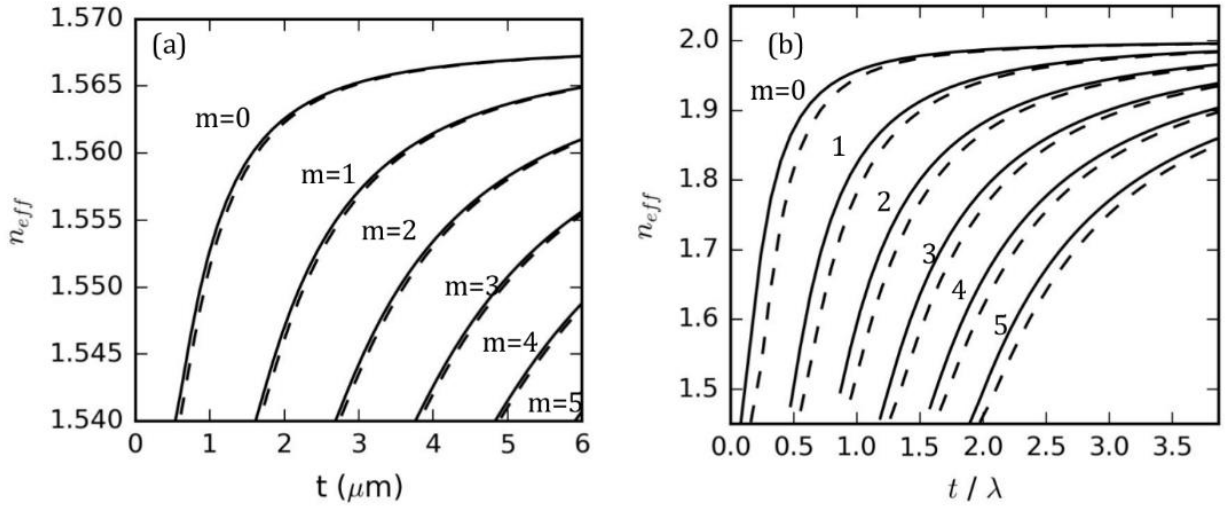

Figure 2-2. (a) Effective mode index as a function of the waveguide thickness t. The wavelength is 632.8 nm, n_1 = 1568, n_2 = 1.538, and n_3 = 1. (b) The effective mode index as a function of t / λ, n_1 = 2, n_2 = 1.45, and n_3 =

1. The solid lines are for TE modes, and the dashed lines are for TM modes. The mode orders are denoted near each curve.

Figure 2-2 plots the effective mode indices for both TE and TM modes from the mode order 0 to mode order 5. The solid lines represent the TE modes, while the dashed lines are for the TM modes.

Although finding the effective index of the one-dimensional three-layer slab waveguide is covered in this chapter, the effective index for two-dimensional waveguides can also be calculated in a similar way. With the help of the effective index theory [32], a two-dimensional waveguide can first be equivalent to one-dimensional three-layer slab waveguide. Then the one-dimensional equivalent waveguide can be solved by the effective mode index of the slab waveguide. It is worth noting that, the polarization of the modes will change when converting the problem from 2D to 1D, and special attenuation must be paid to choose the right polarization.

2.7 Wave Propagation in Conductive Medium

The wave propagation in free space and in waveguides has been discussed. In this session, the waveguide propagation in conductive medium or lossy medium will be elaborated. Start from Ampere's law in time-harmonic form and utilize the relations that $\vec{J} = \sigma \vec{E}$ and $\vec{D} = \varepsilon_0 \varepsilon_r \vec{E}$, where σ is the conductivity and ε_0 is the vacuum permittivity and ε_r is the relative permittivity, simplification of Ampere's law yields:

$$\nabla \times \vec{H} = \sigma \vec{E} + i\omega \varepsilon_0 \varepsilon_r \vec{E} = i\omega \left(\varepsilon' - i\left(\varepsilon'' + \frac{\sigma}{\omega} \right) \right) \vec{E} \tag{2.7.1}$$

Comparison to the solution of the Ampere's law in a loss-free medium $\left(\nabla\times\vec{H}=i\omega\varepsilon\vec{E}\right)$ allows the definition of a complex permittivity which is

$$\varepsilon=\varepsilon'-i\left(\varepsilon''+\frac{\sigma}{\omega}\right)=\varepsilon'-i\varepsilon_e''=\varepsilon'\left(1-i\frac{\sigma_e}{\omega\varepsilon'}\right) \tag{2.7.2}$$

where the real part ε' is the dielectric permittivity and the imaginary part ε_e'' accounts for the loss in the medium. σ_e is the effective conductivity which consists of the static conductivity σ and high-frequency conductivity $\omega\varepsilon''$. For metal, the effective conductivity is due almost entirely to the collision of electrons, meaning $\sigma_e\approx\sigma$ [33]. As we know the propagation constant $\gamma=\alpha+i\beta$ describes the wave propagation phase shift and attenuation. To relate the medium conductivity σ_e with wave propagation attenuation, equation (2.4.10) should be used, and solutions are summarized in following equations.

$$\alpha=\frac{\omega\sqrt{\mu\varepsilon'}}{\sqrt{2}}\left[\sqrt{1+\left(\frac{\sigma_e}{\varepsilon'\omega}\right)^2}-1\right]^{1/2}\ \text{(Np/m)} \tag{2.7.3}$$

$$\beta=\frac{\omega\sqrt{\mu\varepsilon'}}{\sqrt{2}}\left[\sqrt{1+\left(\frac{\sigma_e}{\varepsilon'\omega}\right)^2}+1\right]^{1/2}\ \text{(rad/m)} \tag{2.7.4}$$

Here both α and β have units of 1/m. However, the dimensionless terms neper (Np) and radian (rad) are used to communicate the attenuation and phase meanings.

2.8 Skin Depth

As wave gets attenuated when propagating in metal, a problem arises, that is how far can the wave propagates. Assume a wave travels along the +z direction, its mathematic expression is

$$E(z,t) = \mathrm{Re}\left(E_x^+ e^{-\gamma z} e^{i\omega t}\right) = e^{-\alpha z} E_x^+ \cos(\omega t - \beta z) \tag{2.8.1}$$

where $e^{-\alpha z}$ is known as the wave decay. For good conductors, the wave decays rapidly. The decay of an electromagnetic wave is measured in terms of the skin depth δ. The physical meaning of the skin depth is the distance of penetration where the wave amplitude becomes e^{-1} of its origin. Therefore, the definition of the skin depth is given as

$$\delta = \frac{1}{\alpha} \tag{2.8.2}$$

For a good conductor which is defined such that $\sigma/\omega\varepsilon' \ll 1$, then Equation (2.7.3) reduces to

$$\alpha = \sqrt{\frac{\omega\mu\sigma}{2}} \tag{2.8.3}$$

And the skin depth is then simplified as

$$\delta = \frac{1}{\alpha} = \sqrt{\frac{2}{\omega\mu\sigma}} \tag{2.8.4}$$

Take gold and nickel as examples, their skin depths at two different frequencies are compared in the following table.

Table 2-1 The skin depth of gold and nickel at the wavelengths of 785 nm and 4.3 μm. The data were adopted from Ref.[34]

	785 nm	**4.3 μm**
Gold	13.62 nm	12.58 nm

Nickel	14.49 nm	21.97 nm

2.9 Localized Surface Plasmon Resonance

Plasmonics, based on the interaction processes between electromagnetic radiation and conduction electrons at metallic interfaces, forms a significant part of nanophotonics. At the interface where the permittivity of the media changes the sign, e.g., metal (negative permittivity) and dielectric (positive permittivity), the plasmon is formed at the surface, and therefore, is named surface plasmon (SP). Light coupled with SP forming surface plasmon polaritons (SPPs) whose dispersion relation can be characterized by the following equation [35]:

$$\beta_{SPP} = \frac{\omega}{c}\sqrt{\frac{\varepsilon_m \varepsilon_d}{\varepsilon_m + \varepsilon_d}} \tag{2.9.1}$$

where c is the speed of light, ε_m is the permittivity of the metal, and ε_d is the permittivity of the dielectric. SPPs can propagate along the interface but suffers from heavy attenuation. For the finite size of the interface, e.g., nanoparticle surface, the SPPs are not able to propagate far. Instead, the SPs cause a buildup of electric charge at the edges of the particle. For nanoparticles which are significantly smaller than the wavelength of the exciting light ($\lambda >> R$, where R is the nanoparticle radius), the extinction cross-section of the nanoparticle can be described by the simplified Mie theory [36]:

$$\sigma_{ext}(\omega) = 9\frac{\omega}{c}\varepsilon_d^{3/2} V_0 \frac{\varepsilon_m''(\omega)}{\left[\varepsilon_m'(\omega) + 2\varepsilon_d\right]^2 + \varepsilon_m''(\omega)^2} \tag{2.9.2}$$

where σ_{ext} is the extinction cross-section, $V_0 = (4\pi/3)R^3$ denotes the particle volume, ε_m' and ε_m'' are the real and imaginary parts of the metal permittivity, respectively. The

equation predicts that the absorption band emerges when $\varepsilon_m{}' \approx -2\varepsilon_d$. However, no size dependency of the peak location is involved, which is contradictory to the experimental results. In fact, the oscillating electric field peaks when the size of the particle is in resonant with the incident light. Therefore, size-dependent dielectric functions must be used to accommodate the particle volume factor [37]. For larger particles, the extinction cross-section is dominated by multiple high-order absorption and scattering, thus, full Mie theory must be applied for accurate characterization.

Since the extinction cross-section of the nanoparticles heavily depends on the particle size and shape as well as the dielectric environment, the plasmon resonance is sensitive to the environment change, and thus can be utilized for sensing. What's more, the localized surface plasmon resonances (LSPRs) concentrate the field at the particle extremes. The strong fields at the edges can couple to other particles in close proximity via near-field interaction, which can enhance the fields at the gap between particles in clusters, boosting the sensitivity to environment dielectric variation. Therefore, single nanoparticle and particle clusters are widely used in sensing applications.

Meanwhile, as sufficient fields penetrate the metallic particles, LSPRs are highly lossy. The absorbed electromagnetic energy is dissipated into ohmic losses, generating heat inside the resonator. Hence, LSPRs are often employed in energy harvesting applications thanks to its photo-thermal effects.

2.10 Photo-thermal Effect

As electromagnetic fields dissipate power through the collision of electrons in conductive medium, the absorbed power density in an arbitrary structure is

$$Q\left(\vec{r}\right)=\frac{\omega}{2}\mathrm{Im}\left[\varepsilon\left(\vec{r}\right)\right]\left|\vec{E}\left(\vec{r}\right)\right|^2 \tag{2.10.1}$$

where $\vec{r}$ is the position vector. The absorbed power is proportional to the imaginary part of the dielectric constant and the local field intensity. Once $Q\left(\vec{r}\right)$ is known, the temperature distribution can be calculated using the heat transfer function[38]:

$$\rho\left(\vec{r}\right)c\left(\vec{r}\right)\frac{\partial T\left(\vec{r},t\right)}{\partial t}=\nabla\kappa\left(\vec{r}\right)\nabla T\left(\vec{r},t\right)+Q\left(\vec{r}\right) \tag{2.10.2}$$

where $\rho\left(\vec{r}\right)$, $c\left(\vec{r}\right)$ and $\kappa\left(\vec{r}\right)$ are mass density, specific heat, and thermal conductivity, respectively. $T\left(\vec{r},t\right)$ stands for the time-dependent local temperature. In metals, the thermal processes are typically fast, which means that a steady state is rapidly reached. Therefore, a steady-state condition can be derived as follows:

$$\nabla\left[\kappa\left(\vec{r}\right)\nabla T\left(\vec{r}\right)\right]=-Q\left(\vec{r}\right) \tag{2.10.3}$$

By solving the heat transfer equations, the temperature distribution can be found. Take the one-dimensional biomaterial beam as an example (Figure 4-2), Equation (2.10.3) simplifies to be

$$\frac{d^2T\left(x\right)}{dx^2}+\frac{1}{\kappa}Q\left(x\right)=0 \tag{2.10.4}$$

where $\kappa=\left(\kappa_1t_1+\kappa_2t_2\right)/\left(t_1+t_2\right)$ is the equivalent thermal conductivity. Assuming that the heat source is a point source, meaning $Q(x=0)=P$, and the two ends have a fixed temperature, the solution to the one-dimension case is

$$\Delta T\left(x\right)=\frac{\left(x+l/2\right)}{2\left(\kappa_1t_1+\kappa_2t_2\right)w}\quad\left(-l/2<x<0\right) \tag{2.10.5}$$

$$\Delta T(x) = \frac{(x + l/2)}{2(\kappa_1 t_1 + \kappa_2 t_2) w} \quad (-l/2 < x < 0) \tag{2.10.6}$$

where l is the length of the beam, and w is the width of the beam. It can be found that a point source will yield a linear temperature distribution.

Chapter 3

Silicon Nitride Optical Leaky Wave Antennas

3.1 Introduction

Leaky wave antennas are a class of antennas that use traveling waves to produce narrow radiation beams [39]. The theory and applications of leaky waves (LWs) have been extensively developed since the first known LW antenna introduced by W.W. Hansen in 1940 [40]. A fundamental method of achieving LW radiation is to use a waveguide with periodic features, which consist of a waveguide supporting a slow (guided) wave that has been periodically modulated along the waveguide axis. The periodic modulations create an infinite number of Floquet harmonics, among which one Floquet harmonic will be a fast wave and thus can be leaked as a radiating wave [41], [42]. The LW antennas have the advantage of radiating in either forward or backward directions, as its beam will scan a range of angles by changing frequency. Many LW antennas, including corrugated metal films [43]–[47] and plasmonic nanosphere arrays [48]–[50], utilize periodic structures to enhance radiation in optical frequencies. Besides metallic structures, dielectric-based periodic antennas have also been widely used in millimeter wave [51] and optical applications [52]. Optical leaky wave antennas (OLWAs) can direct light, focus energy, and enhance light-matter interaction. Therefore, they are promising for applications such as free space optical communications [53], space-division multiplexing [54], [55], and tunable grating couplers [56], [57]. The detailed theory of CMOS compatible OLWAs can be found in

Ref. [58]–[60]. The OLWA provides directive radiation at 1550 nm in a dielectric waveguide comprising periodic semiconductor perturbations.

This chapter is organized as follows. Section 3.2 briefly introduces the LW principles. Section 3.3 includes the OLWA fabrication procedure. The experiment setup and the testing results are elaborated in Section 3.4. The radiation pattern is examined to reveal its wavelength-dependence and polarization-dependence. A numerical simulation is also included for verification. In Section 3.6, I summarize the performance of the OLWA and discuss its potential applications.

3.2 Theoretical Modeling of the OLWA

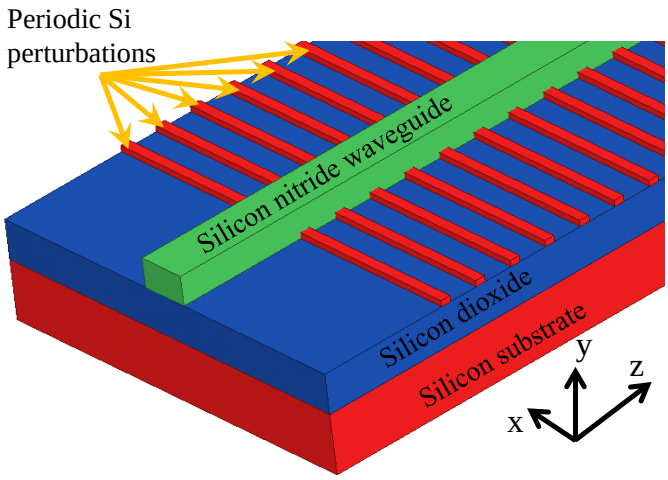

Figure 3-1. Schematic of the OLWA made of a Si_3N_4 waveguide over periodic Si perturbations for possible electronic control.

The geometry of the radiating structure under study is shown in Figure 3-1. The device is designed on a silicon nitride (Si_3N_4) on silicon-on-insulator (SOI) platform that has drawn tremendous interest as a promising solution to integrated optical interconnections in recent years [23], [25], [61]. Silicon nitride is chosen as the dielectric waveguide material

due to its low propagation loss, wide transparent window and silicon-compatible fabrication technology [62]. The slow wave guided by the Si_3N_4 waveguide becomes leaky due to the periodic Si perturbations. The overall leaky mode that propagates in the waveguide can be represented as a superposition of an infinite set of Floquet spatial harmonics travelling with wave numbers $k_{z,n} = \beta_{z,n} + i\alpha_z$ [60], where $\beta_{z,n} = \beta_{z,0} + 2\pi n/d$ and z is assumed to be the direction of propagation. Here, n is an integer from -∞ to +∞ that tags the n-th spatial harmonic, $\beta_{z,0}$ is the fundamental harmonic's phase constant, and d is the period of the perturbations. All spatial harmonics have the same attenuation constant α_z [47], [58], [60] among which, one of them is engineered to be a fast wave that leads to the LW radiation. Usually, this fast harmonic is the n = -1 harmonic, and thus $\beta_{z,-1} = \beta_{z,-1} - 2\pi/d$ such that $\left|\beta_{z,-1}\right| < k_h$, with k_h the wavenumber in the host medium. The leaky harmonic's electric field propagates along the perturbed section of the waveguide as

$$\mathbf{E}(x,y,z) = \mathbf{E}_{-1}(x,y)e^{i\beta_{z,-1}z}e^{-\alpha_z z} \tag{3.2.1}$$

It is important to stress that the leaky wave is not bounded to the waveguide. On a radiation aperture chosen sufficiently above and outside the waveguide, the field can be assumed as only composed of -1 harmonic, since all other harmonics have their field distributions strictly confined in the waveguide core.

The radiated beam from such an antenna can be modeled by using equivalent aperture integration technique, in which most of the radiation is directed to $\theta = \theta_0$ where θ_0 is determined by the expression $\cos\theta_0 = \beta_{z,-1} / k_h$ [58]. We have used the information that the radiated beam is generated by the -1 harmonic. Therefore, the radiation close to the "broadside" direction (e.g., the direction almost orthogonal to the waveguide axis z) is

obtained when $\beta_{z,-1} \ll k_h$. The normalized far-field pattern on the *y*-*z* plane is derived as [58],

$$F(\theta) = \left| \frac{\sin\left[\left(k_h \cos\theta - k_{z,-1}\right)\frac{L}{2}\right]}{\left(k_h \cos\theta - k_{z,-1}\right)\frac{L}{2}} \right| \tag{3.2.2}$$

where L is the length of the radiating aperture assumed equal to the length of the OLWA. The leaky harmonic's wave number $k_{z,-1}$ can be extracted from the full-wave simulations by sampling the field periodically along the perturbed waveguide, and then the phase constant and the attenuation constant can be recovered by fitting curves to the simulated field's phase and amplitude profile as shown in Ref. [58]. We stress that the waveguide has two fundamental modes called TM and TE modes which are respectively defined as (i) the vertically electric field polarized mode which has perfect magnetic conductor symmetry with respect to the *y*-*z* plane and (ii) the horizontally electric field polarized mode which has perfect electric conductor symmetry with respect to *y*-*z* plane. When the waveguide is periodically perturbed, both of these modes may lead to leaky-wave radiation whose far-field pattern can be approximated by Eq. (3.2.2).

3.3 Fabrication of OLWA

The OLWA is fabricated on an SOI wafer [63] with 1 μm thick silicon dioxide (SiO_2) buffer layer. The Si device layer, in which the nanowires are patterned, is thinned to be 150 nm thick by dry etching and coated with back anti-reflection coating (BARC) layer and the photoresist. Lithography is implemented via an ASML 5500 optical stepper, followed by fluorine RIE plasma etching to transfer patterns from the photoresist to the Si device layer.

The fabricated Si nanowires are shown in Figure 3-2(a). The narrow vertical lines are the Si wires which are connected to a Si "skeleton" to prevent the nanowires from being peeled off. The array has 50 nanowires with a spatial periodicity d = 1 μm, and each wire is measured to be 260 nm wide in the z direction. The Si_3N_4 waveguides are then deposited by the low-pressure chemical vapor deposition (LPCVD) method with a stoichiometric recipe, and patterned by standard optical lithography, followed by fluorine RIE etching. The fabricated Si_3N_4 waveguide is shown in Figure 3-2(b), extending horizontally in the SEM image. The waveguide that is used in our experiments is measured to be 1 μm wide (in the x-direction) and 735 nm thick (in the y-direction).

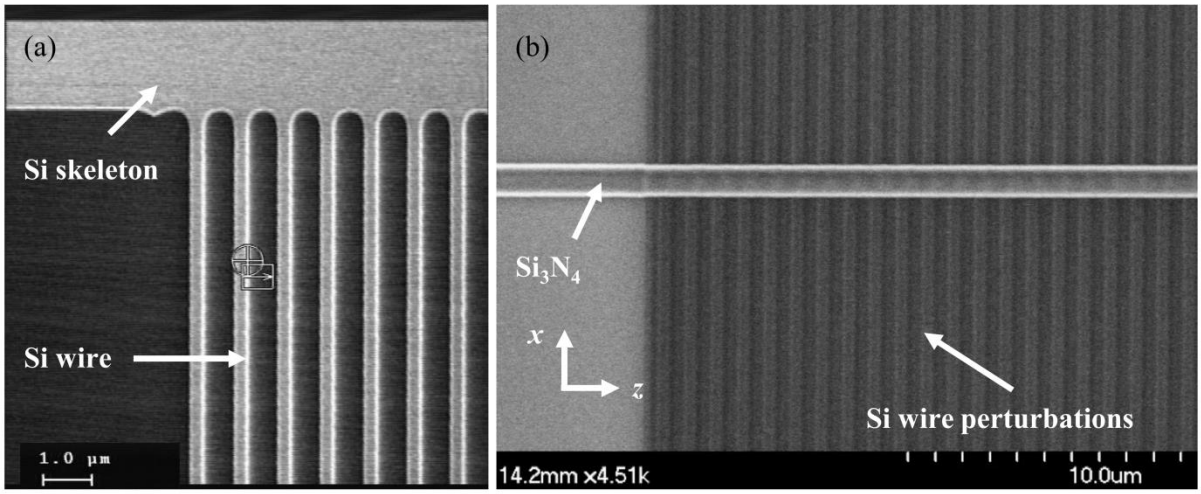

Figure 3-2. (a) Scanning electron microscopy (SEM) image of the fabricated Si perturbations. (b) SEM picture of the fabricated Si3N4 waveguide sitting on the periodic Si perturbations.

3.4 Characterization of OLWA

3.4.1 Measurement Setup and Procedure

The OLWA is designed to radiate in both upward and downward directions normal to the wafer plane. The Si substrate bottom surface is rough and difficult to detect experimentally. Therefore, we only report the characterization of the radiation in the upward direction. The experimental setup that is utilized in the measurement of the far-field patterns is illustrated in Figure 3-3(a). A tunable infrared laser (MLS-2100, Santec) is used as the source, followed by an erbium-doped fiber amplifier (EDFA, AEDFA-C-231-R, Amonics) to boost the power. To feed the antenna, a tapered and lensed fiber (TLF, OZ Optics Ltd.) is employed to butt-couple light into the waveguide facet. The polarization of the light at the TLF is handled by the polarization controller depicted in Figure 3-3(a).

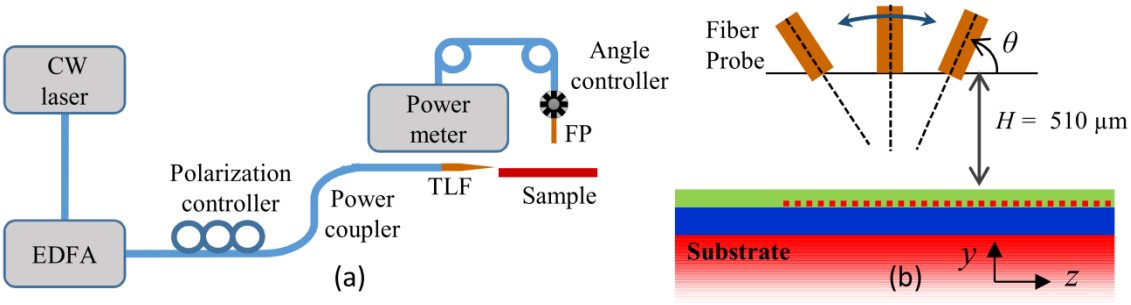

Figure 3-3. (a) Schematic of the OLWA radiation pattern measurement setup. EDFA, TLF, and FP stand for erbium-doped fiber amplifier, tapered lens fiber, and fiber probe, respectively. (b) Schematic of the various FP orientations during the measurement of radiated power at various angular directions. The angle between the radiation detection direction and the waveguide propagation direction is denoted as θ.

On the detection arm, a cleaved SM-28 fiber probe (FP) is used to detect the radiation above the OLWA device. Due to the single mode fiber's small numerical aperture, the FP has a half power beam width of approximately 3° and an antenna directivity of 26 dB. It is a directive detector and thus must be properly oriented. An angle controller is employed to

adjust the FP direction. An optical power meter (1830-C, Newport Corporation) is employed to monitor the power collected by the FP.

Before we start the measurement of the radiation pattern, the FP is oriented at a reference angle θ_f (e.g. $\theta_f = 85°$ that is close to the expected maximum radiation angle) and we make sure it points to the antenna by controlling its position along the *z*-axis to maximize the power reception for that fixed FP orientation. Then the polarization controller preceding the TLF is adjusted for maximizing the reception power at the FP, and this polarization state is not altered during the radiation pattern measurement.

The radiation intensity measurement at a certain angle θ starts by first orienting the FP along θ. Next, the FP is horizontally scanned along the *z*-axis by a mechanical stage via fine-tuning until the maximum power reception is achieved. In doing so, we maintain a constant vertical distance of H = 510 μm between the FP tip to the waveguide surface as shown in Figure 3-3(b). Maximum power reception occurs when the FP points to the antenna since the FP is a directive detector. This maximum power is recorded as $P_{\text{probe}}(\theta, R)$ which is the power received at angle θ and at the distance $R = H/\sin\theta$ between the FP and the OLWA radiation center. The steps above are repeated for every angle θ reported in the radiation pattern. Since the radiation intensity scales proportionally to $1/R^2$, the radiation pattern $P(\theta)$ is then retrieved by

$$P(\theta) = R^2 P_{\text{probe}}(\theta, R) = P_{\text{probe}}(\theta, R)\frac{H^2}{\sin^2\theta} \tag{3.4.1}$$

During the radiation pattern measurement, the reception power data are prone to temporal power drift due to the mechanical instability of the translational stages. Each angular sweep starts with $\theta = 65°$ and ends with $\theta = 110°$ in our experiment. To compensate

for power drift, the power reception at $\theta = 65°$ is measured twice, before and after the angular sweep. The ratio of the power measured at $\theta = 65°$ after the whole angular sweep over the power measured at $\theta = 65°$ before the angular sweep is denoted as η. This ratio reflects the temporal power drift of the system. To compensate the drift, the power measured at each angle is weighted by a factor between 1 and $1/\eta$ by assuming that the drift is linear with time, and assuming that the angle measurements are separated by equal time intervals. It is worth noting that the power drift did not bring the far-field signal below the noise level. It could be removed with better-controlled stages.

The FP tip in our measurement setup is not in the far-field in the strict sense, as a sacrifice to increase the dynamic range of the power reception. The OLWA length is $D = 50\ \mu$m, accordingly, the far field is at distances larger than $2D^2/\lambda_0 \approx 3225\ \mu$m and the reactive near-field boundary is at distances larger than $0.62\left(D^3/\lambda_0\right)^{1/2} \approx 176\ \mu$m [64]. Note that the *effective* OLWA length (i.e., the length where most of the radiation comes from owing to the exponential decay. It could be defined as the effective aperture but in one dimension) is shorter than *D*. However, considering the whole OLWA length *D* in the calculation lets us have a conservative estimation of field boundaries. The measurement distance *H* = 510 μm falls into the Fresnel region, i.e., in the radiating near-field region [64], located between the reactive near-field boundary and the far-field boundary.

3.4.2 Radiation Pattern

The measured and simulated radiation patterns on the *y*-*z* plane, normalized to their individual maxima, are compared in Figure 3-4. The measured radiation pattern at the

wavelength of 1550 nm has its maximum intensity at the angle of 85.1° and a half-power beam width of approximately 5.0°. The radiation peak angle θ_p is calculated as $\theta_p = (\theta_{\text{-3dB},left} + \theta_{\text{-3dB},right}) / 2$ to average out the noise effects, where $\theta_{\text{-3dB}}$ denotes the angle at which the radiation intensity drops to one half of its maximum. Side lobes are at least 7 dB below the dominant main lobe. Since the silicon perturbations are at the base of the waveguide, a significant part of the radiation power will go downwards into the silicon substrate but not only upward, which causes the side lobe ratio in the upward radiation direction to be limited. Note that the bottom surface is rough, therefore it diffuses downward radiation. Radiation configurations could be actually optimized to maximize the upward radiation by also including matching and reflecting layers. Experimental results are compared to the full-wave simulations using the frequency domain finite elements method (implemented in HFSS by Ansys Inc.), assuming that either the fundamental TE or TM mode is propagating in the waveguide. In the simulation model, Si, Si_3N_4 and SiO_2 relative permittivities at 1550 nm are assumed to be 12.11, 3.61, and 2.33, respectively. The far-field radiation patterns are simulated without taking into account the aperture of the FP, i.e., they provide the OLWA radiation pattern without averaging over the FP aperture. However, the averaging effect of the fiber tip may wash out the nulls and slightly broaden the main lobe's beam width in the measured pattern. Experimental results (the blue curve in Figure 3-4) match the simulated radiation pattern only when a TM polarized wave (the red curve in Figure 3-4) is excited in the waveguide in the simulation model. This leads to an initial guess that the TE mode excited in the waveguide does not result in a significant contribution in the measured far-field pattern, as it will be further clarified in the following text. The simulated

radiation pattern has an emission peak at 82.4° with a beam width around 4.0°. Given the experimental limitations, the experimental and numerical results are in good agreement.

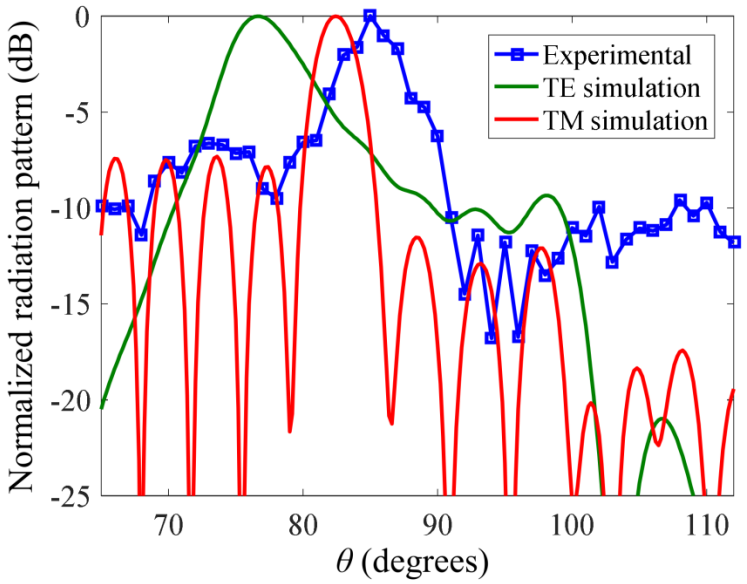

Figure 3-4. Measured (blue) and simulated radiation patterns (on the *y*-*z* plane) generated by TE (green) and TM (red) waveguide modes at 1550 nm wavelength as a function of θ, normalized by their maximum intensities.

The observation that the simulated TM mode radiation pattern matches the experimental far-field pattern rather than the TE mode can be attributed to two different reasons (i) the TM mode radiation pattern has a simulated peak around 82.4° whereas the TE mode radiation pattern is not expected to have any sharp radiation peak around 85.1°, and (ii) the TE mode is expected to suffer heavier attenuation than the TM mode does from the TLF excitation point to the FP. We estimate that the TE mode suffers *at least* 7 dB more power loss, including the wave propagation loss and the inferior radiation gain, than the TM mode. The difference between the attenuation of the TM and TE modes is mainly caused by fabrication imperfections.

To further strengthen our explanation, we discuss next the details of a new set of measurements, aiming to find the dependence of the measured far-field pattern on the polarization of the wave launched at the TLF (Figure 3-3(a)). Due to the experimental limitations, we can use only the measured far-field signature to identify the polarization of the mode in the OLWA. We carry out two sets of far-field pattern measurements corresponding to two *extreme* states of the polarizations: (i) first the polarization of the launched field is varied via the polarization controller (Figure 3-3(a)) to maximize the power received at the reference angle $\theta_{f,1} = 85°$ and then the radiation pattern is measured as explained in Section 3.4.1 without altering this polarization state, namely MaxP state; (ii) again at the same reference angle $\theta_{f,1} = 85°$, the polarization of the wave at the TLF is varied to minimize the power reception and the radiation pattern is measured again for this polarization state, namely MinP state. We then repeat steps (i) and (ii) starting with two other reference angles $\theta_{f,2} = 75°$ and $\theta_{f,3} = 65°$. The motivation of using multiple reference angles arises from the fact that the TM mode may radiate more power than the TE mode at one radiation angle, but it may have less power than TE mode radiation at another angle, as illustrated in Figure 3-4. This is also the reason that the polarization state should be tuned at first and then stays intact while sweeping the angle. By changing the reference angle, the polarization state corresponding to MaxP and MinP will change, so that we catch the far-field signature of distinct waveguide modes that may radiate.

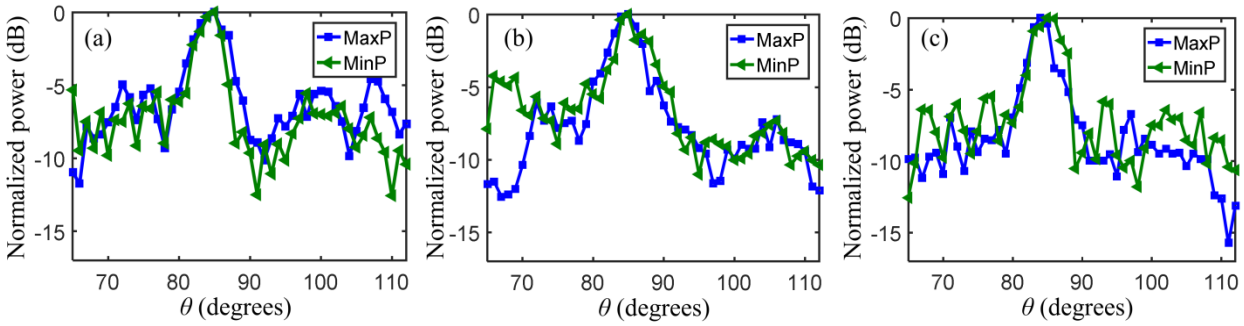

Figure 3-5. Normalized measured radiation patterns (in the *y*-*z* plane), for two polarization states at the waveguide entrance (TLF stage in Figure 3-3(a)) that cause maximum (MaxP) and minimum power (MinP) power reception at the FP with orientation angles (a) $\theta_{f,1}$ = 85°, (b) $\theta_{f,2}$ = 75° and (c) $\theta_{f,3}$ = 65°. The polarization extinction ratios (the difference between the peak radiation intensities of the MaxP and MinP states) for (a), (b) and (c) are 7.4 dB, 11.37 dB, and 10.52 dB, respectively.

Figure 3-5 shows the normalized radiation patterns measured in the MaxP and MinP polarization states with respect to the reference angles $\theta_{f,1}$ = 85°, $\theta_{f,2}$ = 75°, and $\theta_{f,3}$ = 65°. The polarization extinction ratios (difference between the peak radiation intensities of MaxP and the MinP states) are 7.4 dB, 11.37 dB and 10.52 dB, respectively for $\theta_{f,1}$ = 85°, $\theta_{f,2}$ = 75°, and $\theta_{f,3}$ = 65°. The limited extinction ratio may arise from the imperfect polarization control. Theoretically, the OLWA supports both the TE and TM modes and one would expect to observe the different far-field patterns pertaining to the TM and TE input waves among these six radiation patterns in Figure 3-5. However, the manipulation of the wave polarization at the TLF stage does not alter the far-field patterns as observed in Figure 3-5. The TE mode radiation pattern is expected to be different from the TM mode's, yet none of the polarization states in the 6 cases showed a different far-field signature. This supports the claim that the TM mode's radiation pattern, which is in agreement with the simulated

radiation pattern, is detectable, whereas the TE mode suffers from waveguide loss and low radiation directivity in the measured angular range.

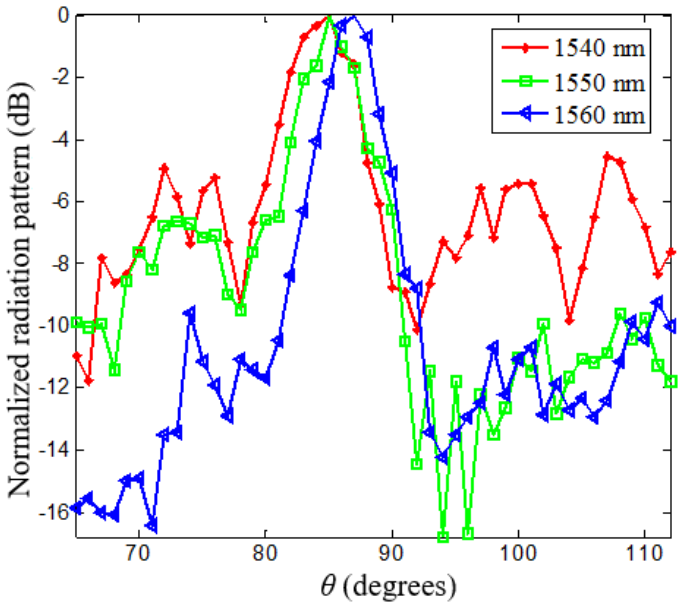

Figure 3-6. Measured normalized radiation patterns at wavelengths 1540 nm, 1550 nm and 1560 nm.

The frequency dependence of the measured radiation pattern is reported in Figure 3-6 for wavelengths of 1540 nm, 1550 nm, and 1560 nm. The radiation pattern at each reported wavelength exhibits a single dominant peak in the angle range between 65° to 112°. The peak locations and half-power beam widths of wavelengths 1540 nm, 1550 nm, and 1560 nm are summarized in Table 3-1. As wavelength increases, the radiation peak angle slightly increases, moving closer to broadside. This is in agreement with the expectations since the leaky-wave mode index in the OLWA slightly decreases as the wavelength decreases.

Table 3-1. Radiation peak angles and half-power beam widths at three operating wavelengths

Wavelength (nm)	Peak angle θp (°)	-3dB bandwidth (°)

1540	84.4	6.2
1550	85.1	5.0
1560	86.8	4.6

3.5 Radiation Modulation

The OLWA is composed of Si nanowires which can be used to tune the radiation pattern. The change of the Si refractive index will alter the wave propagation constant in the waveguide and thus shifts the radiation angle. Plasma dispersion effect [65]–[67] and Franz-Keldysh effect [68] can be used to change the semiconductor refractive indices. In this session, the concept of the electrical modulation of leaky wave radiation is discussed and explored.

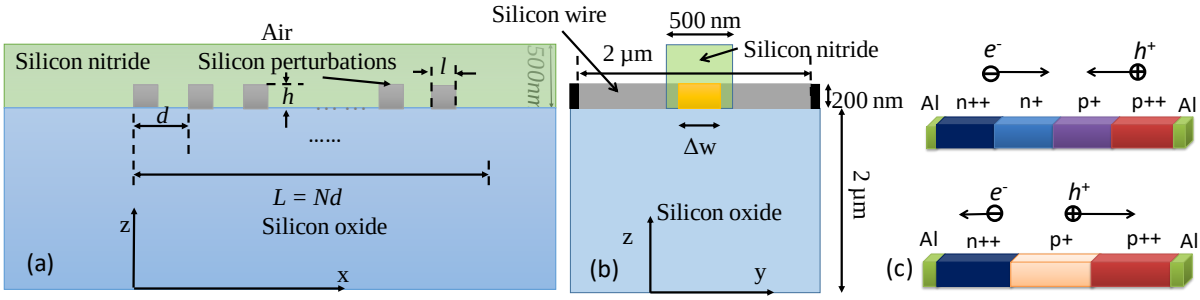

Figure 3-7 (a) Lateral view of the OLWA geometry made of a silicon nitride waveguide along the *x*-axis. The radiation part of the OLWA has a length of *L*. (b) Front view of the OLWA, showing the silicon nitride with a cross-section of 0.5 μm × 0.5 μm and one Si wire embedded. Si wires, 2 μm long with a square cross-section of 200 nm × 200 nm, are embedded in the silicon nitride waveguide, sitting on a 2 μm thick SOI. The yellow region is the modulation region, with a length of Δw in the *y*-direction. The aluminum contacts (black) are connected to the two ends. (c) Structure of the *p*-*n* junction in carrier injection (upper) and *p*-*i*-*n* junction in carrier depletion (lower). The intrinsic region in *p*-*i*-*n* junction is lightly doped to be *p*-type.

In general, the larger the silicon perturbations are, the stronger the modulation effect is. However, larger silicon perturbations also cause stronger wave leakage and hence wider radiation beam. Here an example of OLWA is shown in Figure 3-7. The Si_3N_4 waveguide has a cross-section of 500 nm × 500 nm. The Si perturbation wires are 0.2 μm × 2 μm × 0.2 μm. Each perturbation wire can be viewed as an individual modulator. Since the wires are periodic in space, the analysis applied to one wire is also suitable for all others. Figure 3-7 (b) and (c) illustrate the geometry of the perturbations that can accommodate electrical controls. The upper structure in Figure 3-7 (c) is for carrier injection, whereas the lower one is for carrier depletion.

The geometry used in injection mode is a *p*-*n* junction structure with symmetric doping profile of $N_a = N_d = 10^{16}$ cm^{-3}, and with a length of 0.5 μm in both *n*+ and *p*+ regions. The doping concentrations and lengths are chosen to make the space charge region as wide as the nitride waveguide width. The two ends of the Si wire are heavily doped to 10^{19} cm^{-3} to form good ohmic contact with the aluminum nodes.

Similarly, the optimization of the electrical property in depletion mode gives a structure like a *p*-*i*-*n* diode. P-type Si is preferred to be the "intrinsic" part due to the higher impact on the refractive index. The doping concentration is balanced between refractive index change, modulation width, and the junction breakdown voltage. A moderate doping level of 10^{17} cm^{-3} is found to be optimum. The boundary of the depletion region is defined where the carrier density drops to 1/10 of the doping concentration, and the modulation width is defined as the difference between the maximum and minimum depletion widths. To make the modulation region symmetric to the waveguide, the *n*++ region has a length of 0.8 μm with 10^{19} cm^{-3} dopant concentration. The *p*++ region, 0.5 μm long, is also highly doped to

10^{19} cm^{-3}. The Si-Si_3N_4 surface recombination velocity is chosen to be S_{eff} = 10^2 cm/s for stoichiometric Si_3N_4 [69]. The theoretical refractive index change is 3.4×10^{-4} with 0.178 μm depletion width in DC bias condition.

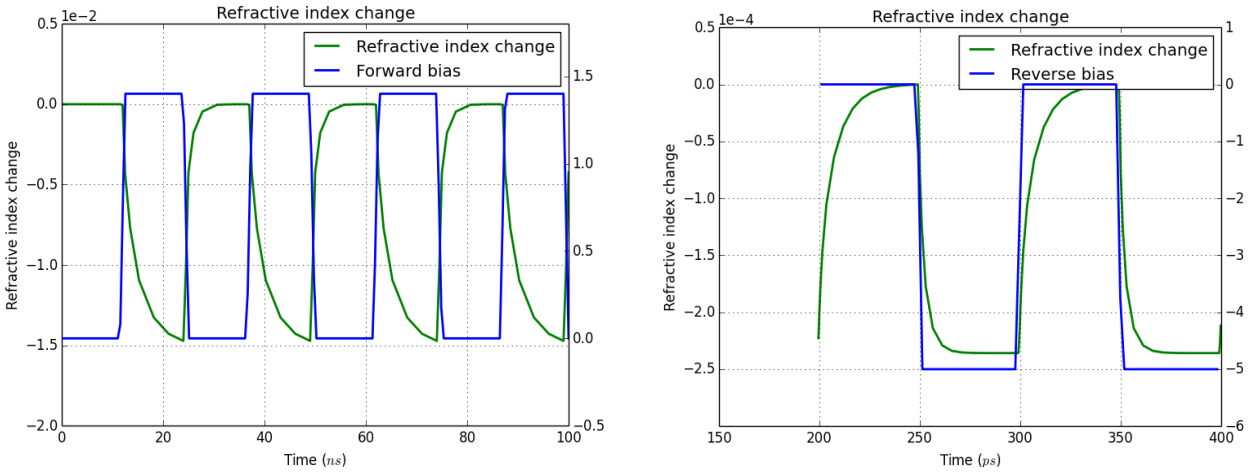

Figure 3-8. (a) Simulation of the average refractive index change in injection mode using a 40 MHz square wave with V_{pp} of 1.4 V and dc offset of 0.7 V. (b) Simulation of the average refractive index change in depletion mode using a 10 GHz square wave with V_{pp} of 5 V and dc offset of -2.5 V. The fluctuation of the refractive index change becomes stable after some time, thus the initial simulation before 200 ps are not included.

Transient simulations show the refractive index step responses in Figure 3-8 for the injection mode and depletion mode. The average refractive index change is simulated by using a 40 MHz square wave for the carrier injection mode and a 10 GHz square wave for the carrier depletion mode. The 10%-90% rise time and fall time for the injection mode are 12 ns and 3 ns, respectively. The rise and fall times for the depletion mode are about 20 ps and 10 ps, respectively. It is apparent that the depletion mode operation can be three orders of magnitude faster than the injection mode which suffers from the minority carrier lifetime issues. The discrepancy between the rise time and the fall time is attributed to the electric field dependent carrier velocity and can be overcome by a pre-emphasized signal

[70]. Although the carrier injection mode has a drawback of low speed, it outweighs depletion mode on the refractive index change. The Δn in the injection mode can be as high as 1.5×10^{-2}, while that in the depletion mode is only 2.5×10^{-4}.

Based on the carrier dynamics in the Si nanowires, the impact of the carrier density change on the far-field radiation pattern of OLWA is investigated. For simplicity, a 2D OLWA mode is simulated, in which the Si domain is modeled with the carrier density-dependent refractive index derived from the 3D Si wire model. We adopt the Si wire geometry (200 nm × 200 nm in the *x*-*z* plane), refractive index, carrier density change and refractive index change from the 3D Si wire model. Compared with our fabricated device, a thinner waveguide (500 nm) is used here to increase the volume ratio of the Si perturbations to the Si_3N_4 waveguide, so that the modulation will be more effective to the change of the refractive index variation in the perturbation region. There are 150 Si perturbations with 200 nm × 200 nm cross-sections in the *x*-*z* plane, and the period *d* is 920 nm along the *x*-direction (Figure 3-7(a)). The simulation results in Figure 3-9 show that the far-field radiation pattern in the *x*-*z* plane has a single sharp peak towards 87.7° with a directivity of 54.65 dB and a beam width of 0.5° at the wavelength of 1550 nm. The beam width is significantly narrower than the measured results, but it is expected because the perturbation-induced scattering loss is weaker in a simplified 2D model than in the 3D model. Therefore, the 2D model leads to smaller leaky wave attenuation constant, longer radiation aperture and hence more directive radiation. When the Si wires have a refractive index change of 1.5×10^{-2}, which can be achieved in the carrier injection mode, the radiation peak angle shifts 0.08°. The tiny angle shift can be further boosted by integrating the OLWA with resonator topologies [59], [60] , such as a Fabry-Perot resonator or a ring-resonator.

High-quality-factor resonators can be put into or pushed out of resonance states by slight variations that are caused by the carrier modulation in Si perturbations, which eventually leads to the modulation of the OLWA's radiation with a large extinction ratio.

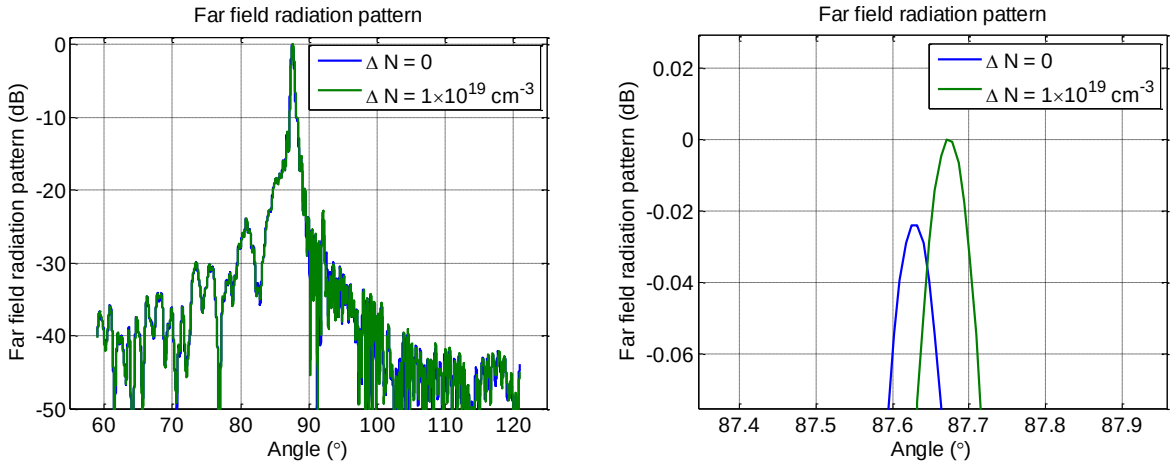

Figure 3-9. (a) Normalized far-field radiation pattern of a 2D OLWA in the *x*-*z* plane with refractive index variation of 1.5×10^{-2} in the Si perturbations. (b) The zoom-in view of the radiation pattern near the peak angle.

3.6 Conclusion

In this chapter, the quasi-far-field radiation pattern of the OLWA has been experimentally characterized in the waveguide symmetry plane. The OLWA has a single directive radiation peak at the angle 85.1° in the range from 65° to 112° at the wavelength of 1550 nm. The sidelobe level is at least 7 dB lower than the main peak. The peak radiation angle scans with frequency as expected from an LW antenna and confirmed experimentally. The selection of the input field polarization significantly modifies the measured radiation intensity, but not the radiation pattern, indicating only one propagation mode (the TM one) is successfully turned into a leaky mode. The reason can attribute to the extra loss on the TE mode mainly introduced by fabrication imperfections.

The device can find promising applications in optical communications, especially for multi-wavelength space division applications owing to its capability of beam scanning with frequency, e.g. launching different wavelengths to multi-core fibers. However, this device may also suffer from limited bandwidth in wavelength–division multiplexing applications, because the radiation angle scans with a wavelength of operation, and thus the reception location varies as the wavelength changes. As for radiation beam modulation, the Si nanowires can be utilized for optical and electronic modulation. I propose using doped Si wires to form *p*-*n* junctions embedded inside the Si_3N_4 waveguide. Refractive index around the *p*-*n* junction regions can be altered by carrier plasma effect, thus changing the radiation intensity at a specific angle. The electrical modulation effects can be further boosted by integrating the OLWA into resonators.

Chapter 4 Silicon Nitride Plasmo-Thermomechanical Infrared Detector

4.1 Introduction

The fundament concept behind the infrared detection is the transduction mechanism that enables the energy conversion from the electromagnetic domain to the others. Depending on the energy transduction mechanism, most of the infrared detectors can be classified as either quantum or thermal detectors [71]. The thermoplasmonics, which takes advantage of the photo-thermal effect induced by resonant light absorption in metallic nanostructures, has become an appealing direction in nanoscale heat sources [72]. Heat transformed by the thermal generators induces temperature change and can be measured via temperature-dependent mechanisms, which include pyroelectricity [73], thermoelectricity [74], conductivity [4], thermo-optics [76], [77], mechanical deflections [78]–[80], etc. Among these mechanical thermal detectors, bimaterial devices play an important role. The bimaterial thermal detectors usually utilize the cantilevers or the suspended membranes that deflect due to thermal expansion. To convert the tiny mechanical deflection into a measurable quantity, optical systems are often employed based on trigonometry [81]–[83] or interferometry [84], [85]. However, these optical systems require discrete bulky lenses and detectors, hence they are difficult to miniaturize. Inspired by the metal-based evanescent field modulators [86] and our achievement of the optical leaky wave antennas (OLWAs) [24], here we propose a novel on-chip plasmo-thermomechanical detector for IR radiation detection.

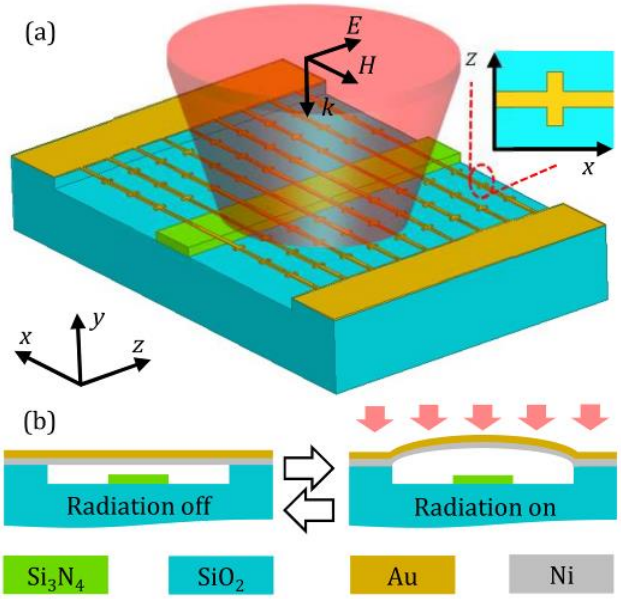

Figure 4-1. Schematic geometry (a) and operation principle (b) of the bilayer plasmo-thermomechanical detector for IR radiation. The inset in (a) shows the top view of the antenna unit cell.

To be specific, the free space target IR radiation is absorbed by the fishbone nanowires and creates thermo-mechanical deflection on the suspended wires. The gap between the nanowires and the underneath waveguide is selected to have an evanescent field interaction that causes attenuation on the waveguided mode. Thus, the change in the target IR radiation intensity is read out by the attenuation of the transmitted power in the waveguides at the probe wavelengths, which can be easily realized by an on-chip photodetector. The proposed design embraces the capability for on-chip integration and the flexibility for operation due to the separation of the target and probe wavelengths.

4.2 Design of the Plasmo-Thermomechanical Device

4.2.1 Device Structure

As demonstrated in Figure 4-1(a), the operation of the detector needs the interplay of three key elements: strip antennas, bimetallic fishbone nanowires, and a waveguide. When the infrared energy is absorbed by the resonant metal strips, the absorbed energy is conducted to the nanowires and creates a thermal gradient. The temperature variation will thermally actuate the nanowires, changing the gap between the nanowires and the waveguide top surface, as illustrated in Figure 4-1(b). In our design, the deformation of the nanowires modulates the evanescent field from the waveguide whose dimension is 1.5 μm × 0.3 μm to guarantee the single TE mode at 1550 nm wavelength. The gap between the nanowires and the waveguide determines the strength of the interaction, which is set to be 50 nm, a separation that has enough evanescent field interaction, and that is also fabrication feasible, e.g., etching the silicon dioxide (SiO_2) sacrifice layer with hydrogen fluoride (HF) acid vapor. For the sake of fabrication compatibility, gold (Au) and nickel (Ni) are used to build the nanowires due to their chemical resistance to HF. Since Au has a larger thermal expansion coefficient (14.2×10^{-6} /K) than Ni (13.4×10^{-6} /K), Au should be placed on top of Ni, so that the nanowire will bend upward to avoid collapsing and sticking to the waveguide surface. The amount of deflection of nanowires is determined by the relative thickness of each layer, the temperature gradient, and the length of the nanowire.

The detection system is modeled and simulated in three parts, being the plasmo-thermal conversion, the thermo-mechanical deflection, and the evanescent field modulation. We use the finite element method based software (COMSOL Multiphysics) to solve all three parts.

4.2.2 Thermo-Mechanical Analysis and Simulation

The composition of the nanowire is first settled by the thermo-mechanical simulation. Au and Ni are employed to build the suspended nanowire, forming a bimetallic structure. Bilayer beams are widely used to sense and control the temperatures [81], [82]. Due to the difference of the thermal expansion coefficients of the materials, stress and constraints will be created, resulting in beam bending. The beam will bend towards the material with a larger thermal expansion coefficient when experiencing a positive temperature difference, and bend towards the material with smaller thermal expansion coefficient if the beam is cooled. This feature can be utilized to thermally actuate the beams and to change structure positions and has been applied in the electron tunneling devices[78], cantilever-based laser displacement sensors[87], interferometers[75], [84], [85] and etc.

The temperature-induced bending of the bilayer beams can be calculated analytically using the following equations[88], [89]:

$$\frac{d^2y}{dx^2} = 6(\gamma_2 - \gamma_1)\frac{t_1 + t_2}{t_2^2 K}\left[T(x) - T_0\right] \tag{4.2.1}$$

$$K = 4 + 6\left(\frac{t_1}{t_2}\right) + 4\left(\frac{t_1}{t_2}\right)^2 + \frac{E_1}{E_2}\left(\frac{t_1}{t_2}\right)^3 \frac{1-\nu_2}{1-\nu_1} + \frac{E_2}{E_1}\left(\frac{t_2}{t_1}\right)\frac{1-\nu_1}{1-\nu_2} \tag{4.2.2}$$

where $y(x)$ is the vertical deflection of the beam at the position x along its length l, t is the thickness of the layers. The subscripts 1 and 2 represent the top and bottom layers, respectively. γ is the thermal expansion coefficient. E stands for Young's modulus. ν is the Poisson's ratio. $T(x)$ is the temperature profile of the beam, and the ambient temperature is denoted by T_0. Given the temperature difference profile $\left[T(x) - T_0\right]$, the differential

equation can then be solved for $y(x)$ and the deflection at the center of the beam $y(0)$ can be found.

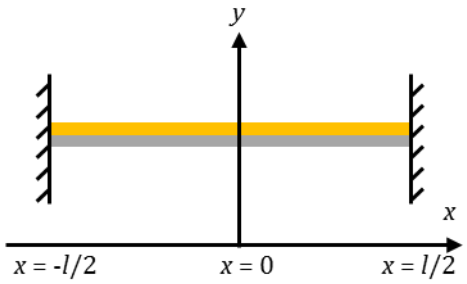

Figure 4-2. Schematic Drawing of the double clamped bilayer beam in the *x*-*y* plane.

Assume the temperature difference is constant, meaning $T(x)-T_0=\Delta T$, the solution to equation (4.2.1) is

$$y(x)=3(\gamma_1-\gamma_2)\cdot\frac{t_1+t_2}{t_2^2K}\cdot\Delta T\cdot\left(\frac{1}{4}l^2-x^2\right) \tag{4.2.3}$$

At the center of the beam, the deflection is

$$y(0)=\frac{3}{4}(\gamma_1-\gamma_2)\cdot\frac{t_1+t_2}{t_2^2K}\cdot\Delta Tl^2 \tag{4.2.4}$$

Another case is when the temperature difference linearly changes with position, which usually happens if a heat source is at the center of the beam. Both ends of the beam are treated as heat sinks. Then the temperature difference profile can be described as $T(x)-T_0=\Delta T\cdot(1-(2|x|/l))$. The solution to this temperature distribution is

$$y(x)=\begin{cases}6(\gamma_2-\gamma_1)\dfrac{t_1+t_2}{t_2^2K}\Delta T\left(\dfrac{1}{2}x^2-\dfrac{x^3}{3l}-\dfrac{l^2}{12}\right) & x>0\\ 6(\gamma_2-\gamma_1)\dfrac{t_1+t_2}{t_2^2K}\Delta T\left(\dfrac{1}{2}x^2+\dfrac{x^3}{3l}-\dfrac{l^2}{12}\right) & x<0\end{cases} \tag{4.2.5}$$

The deflection at the center of the beam is

$$y(0)=\frac{1}{2}(\gamma_1-\gamma_2)\frac{t_1+t_2}{t_2^2K}\Delta Tl^2 \tag{4.2.6}$$

Compared to the linear temperature distribution, parabolic temperature profile assumes a temperature difference profile $T(x)-T_0=\Delta T\cdot\left(1-(2x/l)^2\right)$. Substitute into equation (4.2.1), the solution then becomes

$$y(x)=24(\gamma_2-\gamma_1)\frac{t_1+t_2}{t_2^2K}\cdot\Delta Tl^2\left(-\frac{1}{2}\left(\frac{x}{l}\right)^4+\frac{1}{8}\left(\frac{x}{l}\right)^2-\frac{5}{192}\right) \tag{4.2.7}$$

At the center of the beam, the displacement is

$$y(0)=\frac{5}{8}(\gamma_1-\gamma_2)\frac{t_1+t_2}{t_2^2K}\cdot\Delta Tl^2 \tag{4.2.8}$$

Using Au and Ni as the top and bottom layer for the bilayer beam, the deflection in the beam center can be estimated by equations (4.2.4), (4.2.6) and (4.2.8). The material properties used in the simulations are summarized in the following table.

Table 4-1 Gold and nickel mechanical properties

	***γ* (10^{-6} /K)**[90]	***E* (10^9 Pa)**[91]	***ν* (dimensionless)**[92]
Gold	14.2	78	0.44
Nickel	13.4	200	0.31

Take ΔT =100 K and l = 10 μm as an example, the analytical solution and simulation results of the deflections in the beam center are plotted as functions of the ratio of the top and bottom layer thicknesses, and are compared in Figure 4-3. The simulations have been performed in both 2D and 3D models by a finite-element-based solver (COMSOL Multiphysics). In the 3D simulations, the beam width is assigned to be 200 nm, while in the analytical solution, the beam width is assumed to be infinite in the z direction since it is a 2D model. The 2D simulation results have a maximum 10.4% difference and a maximum 28.6% difference in the linear and parabolic temperature profiles, respectively, compared to analytical simulation. However, when it comes to 3D simulations, the analytical solution is about 4.3 times and about 5.2 times larger than the simulation results in the linear and parabolic temperature profiles, respectively. In fact, the mismatch between the analytical solution and the 3D simulation can be confirmed in the support information of Ref. [84], in which they claimed a 3.7 times difference between the analytical and 3D numerical simulations. The reason for the mismatch attributes to the limitations of Roark's formula in handling 3D model [83].

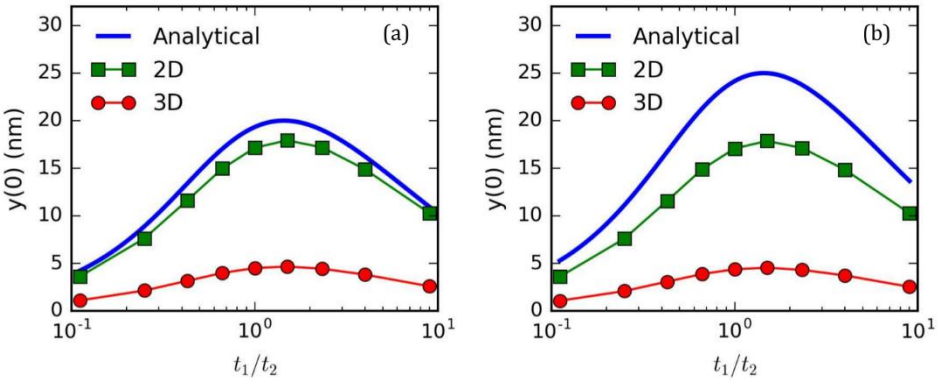

Figure 4-3. The deflection in the center of the bilayer beam as a function of the ratio of the layer thicknesses t_1/t_2 with (a) linear and (b) parabolic temperature difference profiles. The maximum temperature difference ΔT is assumed to be 100 K in the study.

Despite the differences in deflection, both the analytical and numerical results predict the same peak locations. In the analytical solution, when t_1/t_2 reaches 1.46, the deflection curve gets its peak value. In the simulation results, the peaks are located when t_1/t_2 = 1.5. This ratio can be utilized when designing the beam structures to yield the highest actuation.

4.2.3 Electromagnetic Simulation

In full-wave electromagnetic simulations, the mesh size should be smaller than 1/5 of the wavelength to generate accurate and stable results. Consequently, it requires a lot of RAM to model the whole structure and takes much time to finish it. In our actual simulation, we utilize the symmetry and periodicity of the fishbone structure, and assign the corresponding boundary conditions to a smaller portion of the design, to reduce the demand of the computing resources while maintaining the accurate at the same time.

The design of the fishbone nanowire is performed in a unit cell, which repeats itself in the *x* and *z* directions. Although the periodicity breaks at the anchor supports, the simulation of the unit cell still acts as a good approximation of the electromagnetic behavior of the entire wire. The fishbone nanowire, surrounded by air, is suspended 350 nm above a SiO_2 substrate and stretches across the Si_3N_4 waveguide. Its unit cell only contains the SiO_2 substrate in the model since the waveguide width is assumed to be narrower than the nanowire and can be ignored in the unit cell optimization stage. We set the substrate thickness to be 2λ and the air thickness to be 3λ, where λ is the infrared wavelength in free space. Both the substrate and the air are sandwiched in perfectly matched layers (PMLs) to absorb scattering light and minimize reflections at the top and bottom boundaries. The PML thickness is set to be λ.

Figure 4-4 shows the 2D view of the unit cell and annotates the characteristic dimensions. The total metal thickness (in the *y*-direction) is 50 nm, and it includes 30 nm Au layer at the top and 20 nm Ni layer at the bottom. The composition of the metal beam is determined by the conclusion from the thermo-mechanical deflection simulation in the last session.

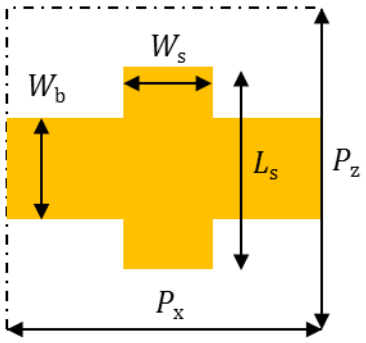

Figure 4-4. The schematic and characteristic dimensions of the fishbone nanowire unit cell. The thickness of the metal t_m is not annotated here.

By feeding the geometry information in the simulation software, the numerical model is depicted as follows.

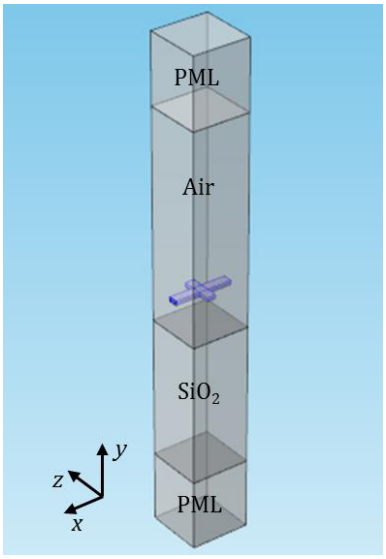

Figure 4-5. The geometry of the numerical model of the fishbone antenna unit cell. The highlighted blue domain is the Au layer.

Before assigning the boundary conditions (BCs) for the numerical model, two assumptions must be stated that lay the cornerstone of the electromagnetic study. First, the infrared radiation is a uniform transverse electromagnetic (TEM) plane wave that is normal to the substrate surface and polarized along the *z*-axis. Second, the unit cell has infinite replicas in the *x* and *z*-axis, meaning that the unit cell is surrounded by the same exact cell. These two assumptions regulate the following boundary condition settings as shown in Figure 4-6.

BC1: The source of the unit cell is provided by a current surface which has only E_z component. The amplitude of the source current is denoted as *amp*. By changing the parameter amp, the desired radiation power density (W/m^2) can be achieved.

BC2: The boundaries perpendicular to the electrical fields are set to be perfect electric conductors (PECs).

BC3: The boundaries parallel to the electrical fields are set to be perfect magnetic conductors (PMCs).

BC4: The top and bottom surfaces of the PMLs are defined to be scattering boundaries. The reflection coefficient of the scattering boundaries is in the order of 10^{-8} at the normal incident angle[93], which guarantees the accuracy.

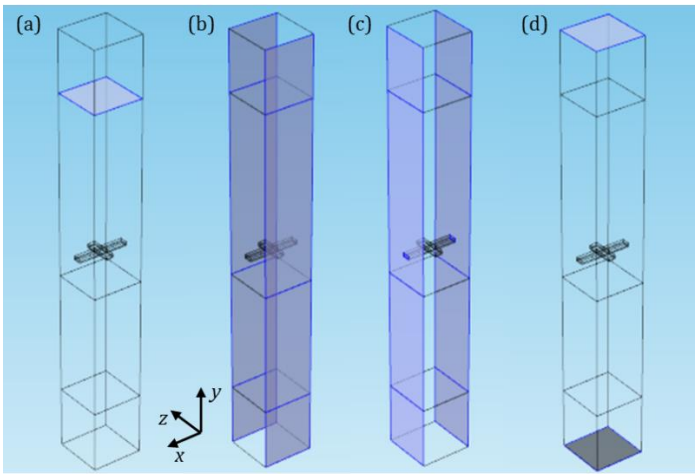

Figure 4-6. Boundary setting for BC1 (a), BC2 (b), BC3 (c), and BC4 (d).

Besides the boundary settings, the domains need to be filled with different materials. The assignment of the materials is illustrated in Figure 4-7.

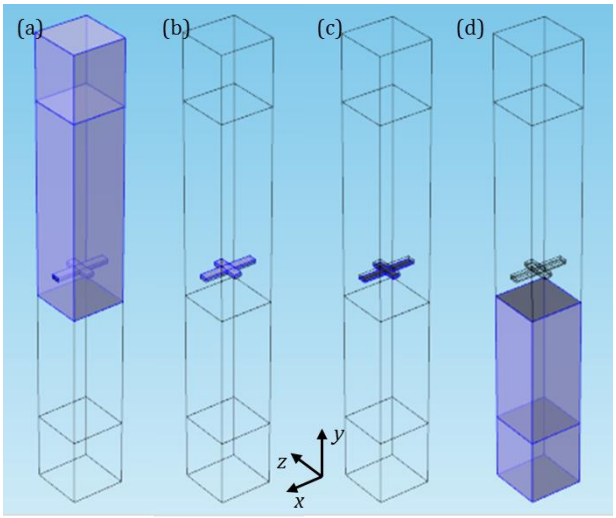

Figure 4-7. Domain settings for (a) air, (b) gold, (c) nickel, and (d) silicon dioxide.

The optical properties of the materials are summarized in the following table.

Table 4-2. Optical properties of the air, SiO_2, Au and Ni that are used in the simulation.

Material	**λ = 785 nm**			**λ = 4.3 μm**		
	ε_r	**μ_r**	**σ [S/m]**	**ε_r**	**μ_r**	**σ [S/m]**
Air	1	1	0	1	1	0
SiO_2	2.1025	1	0	1.907 [94]	1	0
Au	-20.008 – j1.6845 [34]	1	45.6×10^6 [95]	-731.49 – j149.95[34]	1	45.6×10^6 [95]
Ni	-12.949 – j20.422 [34]	1	13.8×10^6 [95]	-225.07 – j130.52 [34]	1	13.8×10^6 [95]

4.2.4 Absorption Coefficient

With all the boundary and material settings settled down, the electromagnetic setting can be carried out. The target of the simulation is to optimize the structure to maximize the absorbed power. Therefore, the absorption coefficient is not only a critical parameter but

also an assessment rubric to judge the structures. The absorption coefficient C_{absp} is defined as

$$C_{absp} = \frac{P_{absp}}{P_{IR}} \tag{4.2.9}$$

where P_{absp} is the total absorbed power, and P_{IR} is the IR power. The P_{absp} can be evaluated by integrating the resistive loss density (emw.Qrh) over the whole simulation domains in COMSOL. P_{IR} can be estimated by multiplying the power density I_{IR} with the cross-section area. The relation between power density of the electromagnetic waves and the source current amplitude (BC1 in Figure 4-6) should be investigated as follows. Given a power density, the amplitude of the source current can be derived from the fitting equations.

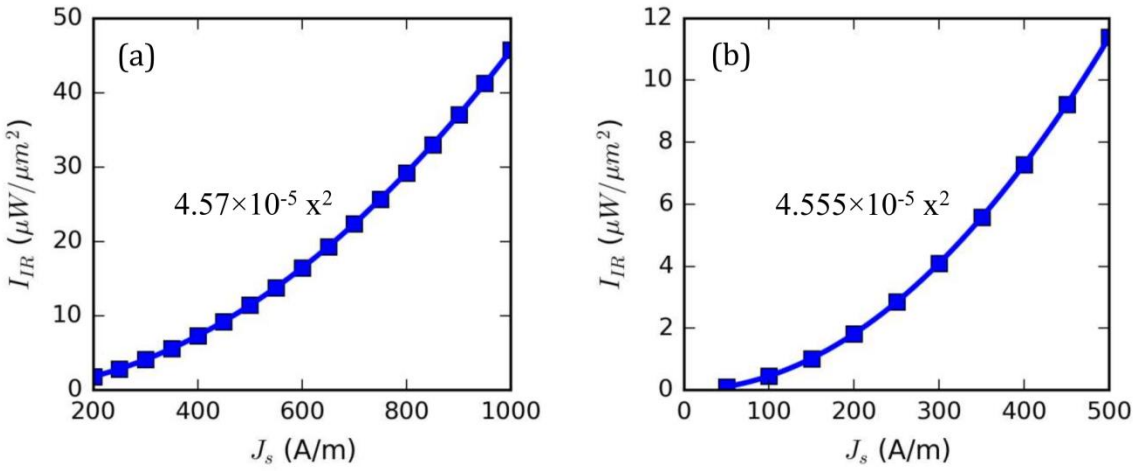

Figure 4-8. The power density I_{IR} as a function of the source current amplitude J_s at (a) 785 nm and (b) 4.3 μm wavelengths. The data are curve fitted with second-order polynomials and equations are denoted in the pictures.

4.2.5 Strip Antenna Optimization

Strip antennas are employed to absorb the infrared radiation. To increase the total absorbed energy, multiple antennas are connected by a single nanobeam, yielding a

fishbone-like nanowire. The fishbone nanowire, surrounded by air, is suspended 350 nm above a SiO_2 substrate and stretches across the Si_3N_4 waveguide. The design of the fishbone nanowire is performed in a unit cell (Figure 4-5) to optimize the strip length L_s, strip width W_s. The beam width W_b is set to be 100 nm in our study. It is worth noting that the nanowire volume contributes to the overall device volume and may lower the temperature increment given the same amount of absorbed energy. Yet the nanowire width is also constrained by the mechanical properties of the metals. For the unit cell, we didn't take the mechanical strength into considerations.

As shown in Figure 4-9, increasing the width of the strip will reduce the resonant wavelength and lower the absorption coefficient. The combination of the L_s = 1.77 μm and W_s = 100 nm yields the highest absorption coefficient of 0.424 for the wavelength of 4.3 μm. For the wavelength of 785 nm, the combination of L_s = 350 nm and W_s = 100 nm exhibits the highest absorption coefficient of 0.338. The optimized antenna for 4.3 μm has a better absorption capability than that for 785 nm.

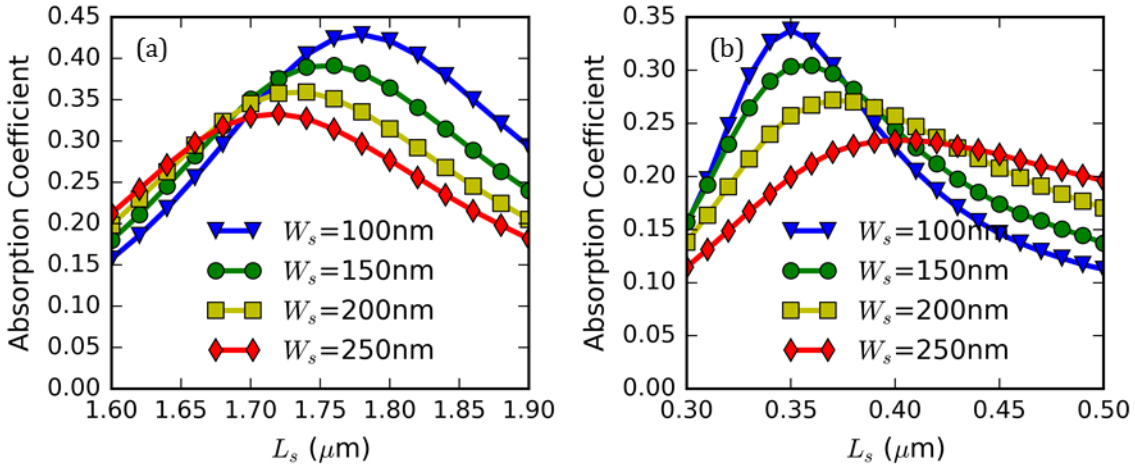

Figure 4-9. The absorption coefficient as a function of the strip length L_s and strip width W_s (a) for a given period of P_x = P_z = 3.1 μm at the wavelength of 4.3 μm, and (b) for a given period of P_x = P_z = 0.66 μm at the wavelength of 785 nm.

4.2.6 Periodicity Optimization

The absorption coefficient is also impacted by the periods of the antenna unit cell. The periods in *x* and *z* directions are optimized simultaneously, meaning P_x = P_z. The optimized strip structure parameters L_s and W_s are fed into the simulation model. From the simulation results shown in Figure 4-10, for the 4.3 μm wavelength, a period of 3.1 μm yields the peak absorption coefficient of 0.424, and a period of 660 nm enables the highest absorption coefficient of 0.338 at the wavelength of 785 nm.

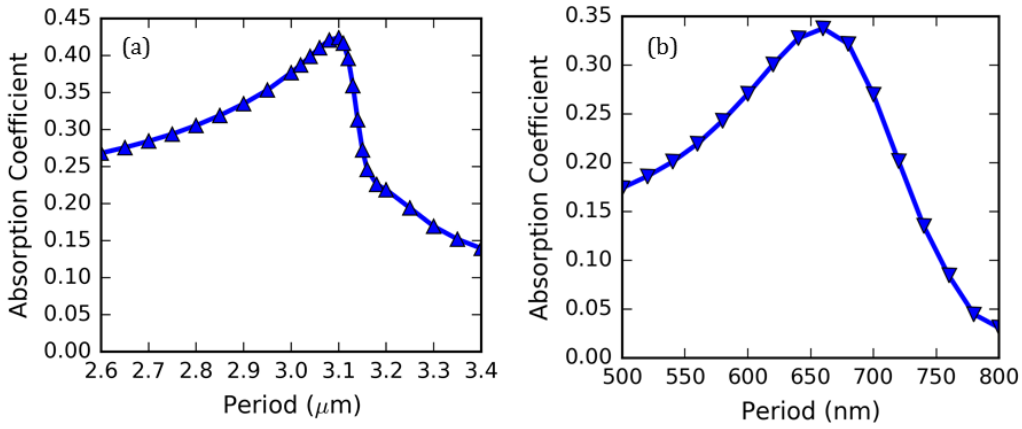

Figure 4-10. The absorption coefficient as functions of the periods (a) for a given strip width L_s = 1.77 μm and W_s = 100 nm at the wavelength of 4.3 μm and (b) for a given strip width L_s = 350 nm and W_s = 100 nm at the wavelength of 785 nm.

4.2.7 Gap between the Antenna and the Substrate

The gap between the waveguide top surface and the suspended nanowire is selected to be 50 nm as a compromise between the wire mechanical strength and the amount of the deflection. As aforementioned, the displacement is proportional to $(t_1+t_2)/t_2^2$, since the ratio of t_1 and t_2 is fixed to be 1.5 in the design, increasing the total thickness will also increase t_2, and leading to a decrease in the mechanical deflection.

The gap between the suspended nanowire and the substrate is 350 nm based on the waveguide thickness. However, this value can be easily shifted due to fabrication error. To etch the SiO_2 sacrifice layer, hydrogen fluoride (HF) will be used. The etching rate of 1:6 buffered oxide etcher (BOE) at 20 °C is about 400 nm/min, therefore a 2 s miss operation will result in about 12 nm fabrication error. In actual fabrication, the HF vapor should be used for the suspended structure, and its etching rate depends on the temperature

difference between the vapor and the substrate. Despite the precise control of the temperature, it is still meaningful to investigate the effect of variation of the gap between the nanowire and the substrate.

The effect of the gap variation on the absorption coefficient is plotted in Figure 4-11. The parameters of the antenna unit cell are chosen from the aforementioned simulations. When the substrate thickness varies from 250 nm to 450 nm, a ±100 nm variation from the designed value, there are only small fluctuations in the absorption coefficients. For the antenna at 4.3 μm, the maximum variation is 7%, while for 785 nm, the variation is 13.4% compared to the absorption coefficient at gap = 350 nm. Since the fabrication induced error will be less than 100 nm, the effect of the gap variation on the absorption coefficient will be negligible.

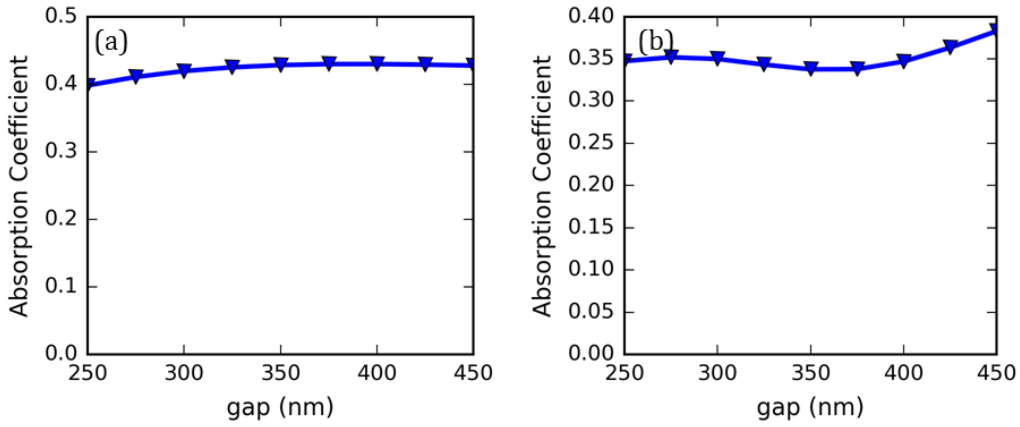

Figure 4-11. The absorption coefficient as a function of the gap between the nanowire and the substrate for the antenna unit cell at (a) 4.3 μm and (b) 785 nm. The antenna unit cell in (a) has L_s = 1.77 μm, W_s = W_b =100 nm, and P_x = P_z = 3.1 μm. The antenna unit cell in (b) has L_s = 350 nm, W_s = W_b = 100 nm, and P_x = P_z = 660 nm.

4.2.8 Sensitivity of the Mid-Infrared Detector at 4.3 μm

With optimized parameters of the unit cells for 4.3 μm wavelength, the design of a fishbone nanowire that includes 6 strip antenna unit cells is demonstrated here. The total length of the wire, l = 18.6 μm, is selected as a compromise of fabrication challenges and the amount of deflection of the wire. The two ends of the nanowire are connected to the metal pads which act as heat sinks, and the temperature of the two ends are assumed to be 293.15 K in simulations. The heat transfer coefficient on the wire surface is assigned to be 5 W/(m^2·K) to mimic the stagnant air cooling condition. For a 4 μW/μm^2 normal incident power density (z-polarized) at 4.3 μm wavelength, the highest temperature on the nanowire can reach 428.16 K, and the temperature profile along the nanowire is quasi-parabolic as depicted in the inset of Figure 4-12(a). Figure 4-12(a) also illustrates that the maximum temperature T_{max} on the nanowire increases linearly with respect to the incident power density. The slope of the curves indicates that the temperature-IR power density conversion ratio η_{TI} is 33.75 K/(μW/μm^2) for this device.

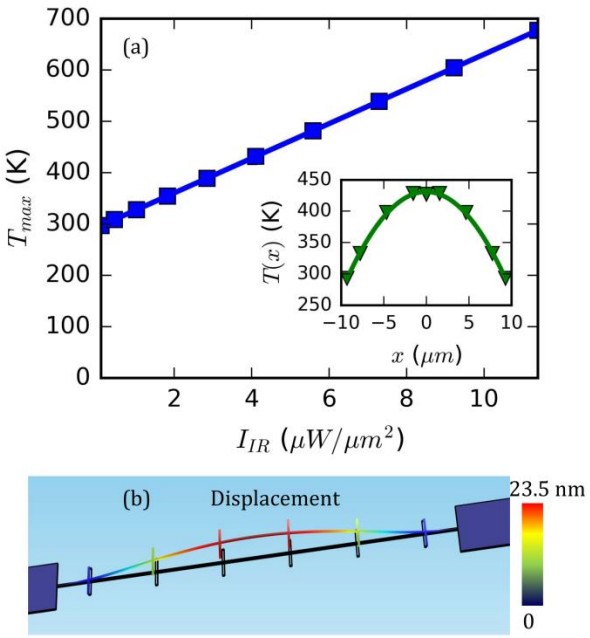

Figure 4-12. (a) The maximum temperature of the nanowire as a function of the IR power density. The inset shows the temperature profile along the nanowire when the input power density is 4 μW/μm². (b) The displacement profile of an 18.6 μm long fishbone nanowire under 4 μW/μm² irradiation power density. The shadow shows the original position of the wire.

The thermal expansion caused by the temperature increment will deflect the nanowire upwards due to the difference in the thermal expansion coefficients of Au and Ni. Since the Si_3N_4 waveguide is located at the center of the nanowire, only the displacement at the beam center is studied here. By feeding the temperature profile generated by the 4 μW/μm² radiation density into the thermomechanical model, the maximum deflection at the center of the nanowire is found to be 23.5 nm as shown in Figure 4-12(b). Since the temperature profile is quasi-parabolic, the displacement-temperature conversion ratio, η_{DT}, can be approximated by equation (4.2.7):

$$\eta_{DT} = \frac{\partial \Delta y(0)}{\partial \Delta T} = -\frac{5}{8}(\gamma_2 - \gamma_1)\frac{t_1 + t_2}{t_2^2 K} l^2 \cdot \zeta \qquad (4.2.10)$$

where l is 18.6 μm for the current device, and ζ is the fitting parameter to match the numerical and simulation results and it is equal to 0.197, and the corresponding η_{DT} is 0.17 nm/K, meaning that a 1 K temperature increment in the beam center will elevate the nanobeam center by 0.17 nm.

The fishbone nanowires are periodically arranged along the waveguide direction (the z direction), to form an OLWA and modulate the propagating wave in the waveguide. Instead of measuring the radiation patterns like we did for OLWAs [24], the change of the waveguide output power, $\Delta P_{wg,out}$, at the radiation *on* and *off* states is of interest here, because it is a measurable quantity by an on-chip photodetector. For a fair comparison, we normalize the variation of the waveguide output power to its input power, yielding the change of the S_{21} parameter, ΔS_{21}. The number of the nanowires, N, affects ΔS_{21} in a way that too few wires limit the modulation strength, while too many wires can attenuate the output power severely, making it challenging to measure ΔS_{21}. If the gap changes from 50 nm to 73.5 nm from the IR radiation *off* to *on* states, a sweep of N finds that ΔS_{21} reaches the maximum when N equals 9, and the peak value is 0.106, as shown in Figure 4-13(a), indicating a modulation depth of 10% on the transmitted power in the waveguide.

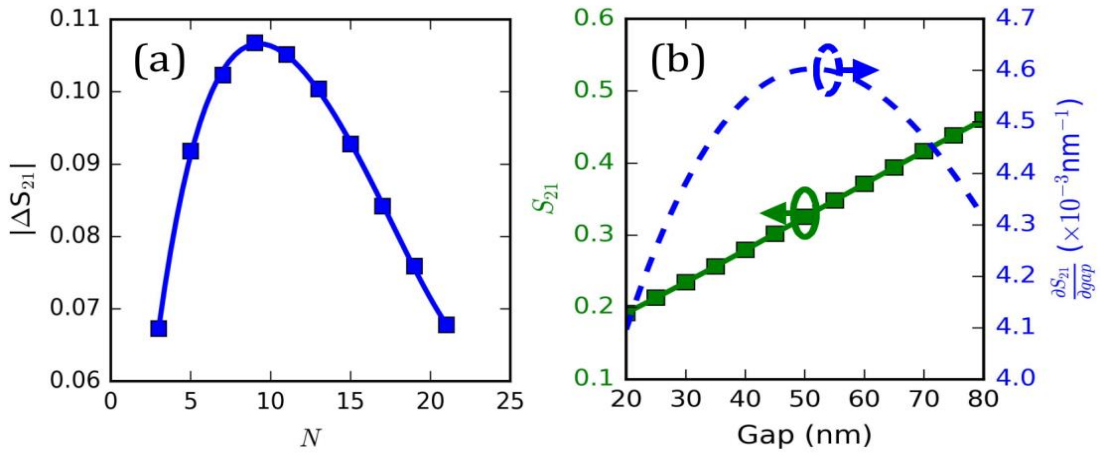

Figure 4-13. (a) The differences of the S_{21} parameters, ΔS_{21}, at gap = 50 nm and gap = 73.5 nm are plotted as a function of the number of nanowires *N*. (b) S_{21} parameter as a function of the gap is shown as the green curve on the left axis. The derivative of S_{21} with respect to the gap is plotted as the dashed blue curve on the right axis.

With the chosen wire number *N*=9, the S_{21} as a function of the change of the gap is studied to reveal the sensitivity of S_{21} to the gap variation, η_{SD}, as shown in Figure 4-13(b). When the gap is 50 nm, 1 nm increment in the gap will result in a 4.6×10^{-3} shift in the S_{21} parameter.

Combining all the conversion ratios from the electromagnetic domain to the thermal domain and then to the mechanical domain and finally back to the optical domain, the figure of merit (FOM) of the device is defined as

$$\mathrm{FOM}=\frac{\partial S_{21}}{\partial I_{\mathrm{IR}}}=\eta_{\mathrm{SD}}\eta_{\mathrm{DT}}\eta_{\mathrm{TI}} \tag{4.2.11}$$

For the proposed device, its FOM is 2.64×10^{-2} $\mu m^2/\mu W$, indicating that 1 $\mu W/\mu m^2$ radiation will result in a 2.64×10^{-2} change in the waveguide S_{21} parameter.

It is worth noting that increasing the waveguide input power can enlarge the output power difference, but it will also heat the nanowire by its own evanescent field, leading to a

larger gap than the designed value and desensitizing the detector. Since the waveguide is narrow compared to the nanowire, the waveguide can be viewed as a point heat source, and the temperature profile along the nanowire changes linearly with respect to positions, following $T(x) - T_0 = \Delta T' \cdot (1-2|x|/l)$, where $\Delta T'$ is the center temperature difference caused by the waveguide heating. With the linear temperature distribution, η_{DT}' becomes

$$\eta_{DT}' = \frac{\partial \Delta y(0)}{\partial \Delta T'} = -\frac{1}{2}(\gamma_2 - \gamma_1)\frac{t_1 + t_2}{t_2^2 K} l^2 \cdot \zeta' \tag{4.2.12}$$

where ζ' is the fitting parameter to match the numerical and theoretical results under the linear temperature distribution, and ζ' equals 0.233 in this study. The corresponding η_{DT}' is 0.16 nm/K. $\Delta T'$ as a function of the waveguide input power P_{in} is depicted in Figure 4-14. When the input power is smaller than 100 μW, $\Delta T'$ will be less than 21 K, causing at most 3.36 nm self-heating deflection, which is an acceptable value.

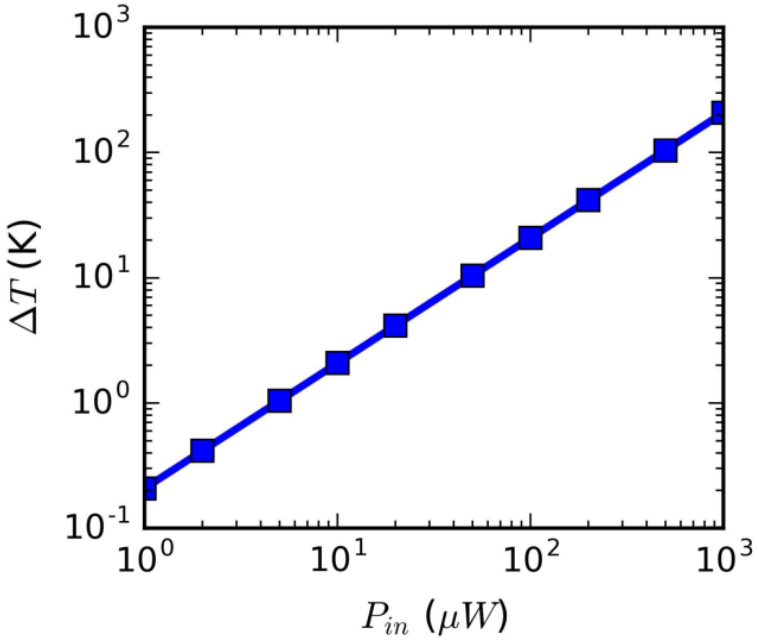

Figure 4-14. The maximum temperature difference $\Delta T'$ at the center of the nanowire as a function of the waveguide input power P_{in}. The gap between the nanowire and the waveguide top surface is 50 nm.

4.2.9 Sensitivity of the Near-Infrared Detector at 785 nm

The analysis for the near-infrared detector at 785 nm wavelength is similar to that of the mid-infrared detector. The total wire length is l = 12.54 μm, 19 times the unit cell period. However, only 16 strip antennas are arranged on the wire, leaving 3×0.66 = 1.98 μm gap in the wire center to make room for the waveguide underneath. The waveguide is 1.5 μm wide, thus the margin of fabrication alignment tolerance is ±240 nm. The two ends of the nanowire are connected to the metal pads which act as heat sinks, and the temperature of the two ends are then set to be 293.15 K. The heat transfer coefficient on the wire surface is assigned to be 5 W/(m^2·K) to mimic the stagnant air cooling condition. For a 68.5 μW/μm^2 normal incident power density (z-polarized) at 785 nm wavelength, the highest temperature on the nanowire can reach 439.65 K, and the temperature profile along the nanowire is depicted in the inset of Figure 4-15(a). Unlike the temperature profile in the fishbone nanowire for 4.3 μm, it is more mesa-like instead of parabolic-like. Figure 4-15(a) also illustrates that the maximum temperature $T_{\max}$ on the nanowire increases linearly with respect to the incident power density. The slope of the curves indicates that the temperature-IR power density conversion ratio η_{TI} is 2.175 K/(μW/μm^2) for this device.

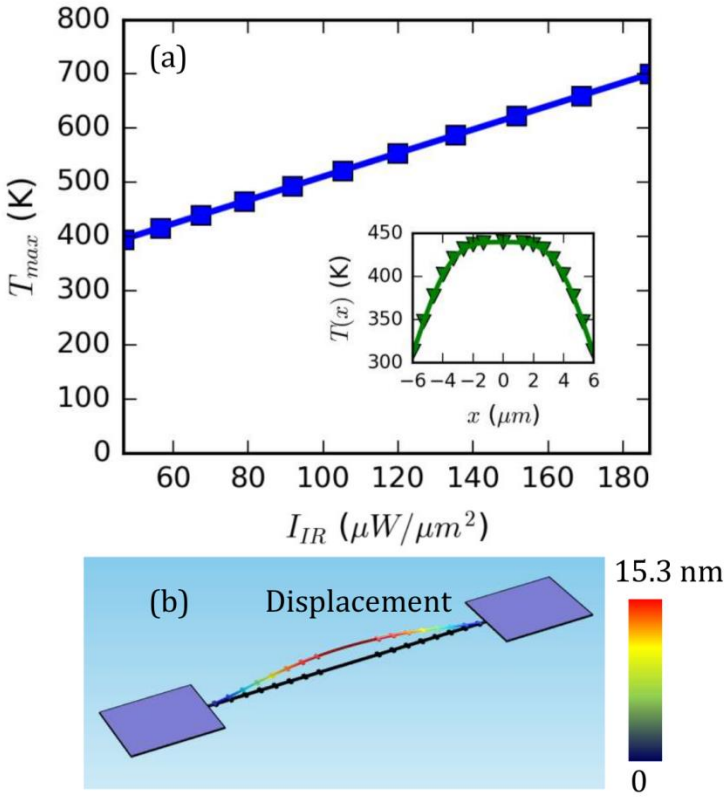

Figure 4-15. The maximum temperature of the nanowire as a function of the IR power density. The inset shows the temperature profile along the nanowire when the input power density is 68.5 μW/μm^2. (b) The displacement profile of a 12.54 μm long fishbone nanowire under 68.5 μW/μm^2 irradiation power density. The shadow shows the original position of the wire.

By feeding the temperature profile generated by the 68.5 μW/μm^2 radiation power density into the thermomechanical model, the maximum deflection at the center of the nanowire is found to be 15.3 nm as shown in Figure 4-15(b). Compare to the example for 4.3 μm wavelength which has a maximum temperature of 428.16 K and a length of 18.6 μm, the case for 785 nm has a similar maximum temperature but shorter length, therefore less displacement. Although the temperature profile is not strictly parabolic, the quasi-parabolic approximation is still used to calculate the displacement-temperature conversion ratio, η_{DT}, from equation (4.2.7):

$$\eta_{DT} = \frac{\partial \Delta y(0)}{\partial \Delta T} = -\frac{5}{8}(\gamma_2 - \gamma_1)\frac{t_1 + t_2}{t_2^2 K} l^2 \cdot \zeta \tag{4.2.13}$$

where l is 12.54 μm for the current device, and ζ is the fitting parameter to match the numerical and simulation results and it is equal to 0.288, and the corresponding η_{DT} is 0.113 nm/K, meaning that a 1 K temperature increment in the beam center will elevate the nanobeam center by 0.113 nm.

Based on the simulation result from Figure 4-15(b), and assume that the gap changes from 50 nm to 65.3 nm from the IR radiation *off* to *on* states, a sweep of N finds that ΔS_{21} reaches the maximum when N equals 11, and the peak value is 0.066, as shown in Figure 4-16(a), indicating a modulation depth of 6.6% on the transmitted power in the waveguide. With the chosen wire number N=11, the S_{21} as a function of the change of the gap is studied to reveal the sensitivity of S_{21} to the gap variation, η_{SD}, as shown in Figure 4-16(b). When the gap is 50 nm, 1 nm increment in the gap will result in a 4.3×10^{-3} shift in the S_{21} parameter.

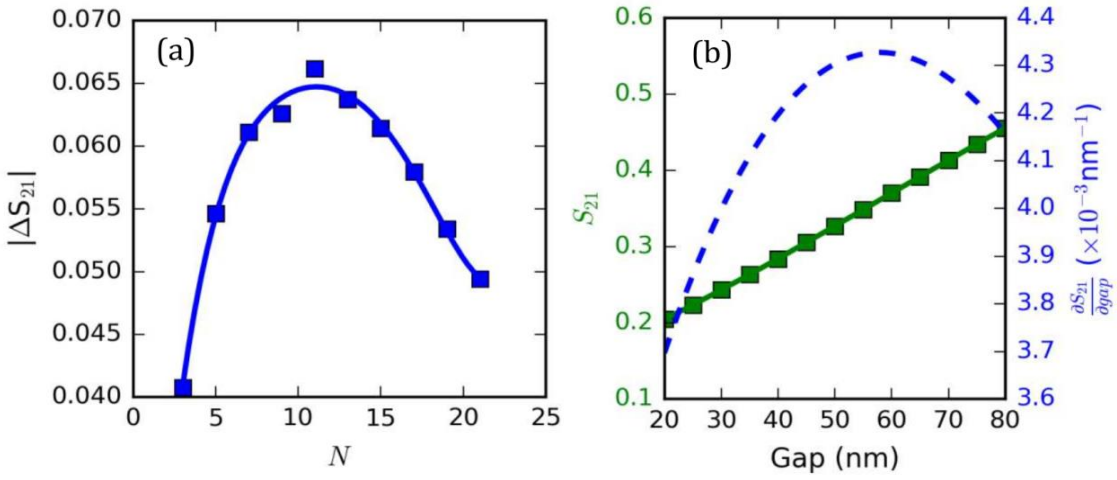

Figure 4-16. (a) The differences of the S_{21} parameters, ΔS_{21}, at gap = 50 nm and gap = 63.5 nm are plotted as a function of the number of nanowires N. (b) S_{21} parameter as a function of the gap is shown as the green curve

on the left axis. The derivative of S_{21} with respect to the gap is plotted as the dashed blue curve on the right axis.

For the proposed device, its FOM is 2.175 K/(μW/μm^2) × 0.113 nm/K × 4.3×10^{-3} /nm = 1.06×10^{-3} μm^2/μW, indicating that 1 μW/μm^2 radiation will result in a 1.06×10^{-3} change in the waveguide S_{21} parameter.

The self-heating problem is also discussed here to avoid desensitization of the device. Since the waveguide is narrow compared to the nanowire, the waveguide can be viewed as a point heat source, and the temperature profile along the nanowire changes linearly with respect to positions, following $T(x) - T_0 = \Delta T' \cdot (1-2|x|/l)$, where $\Delta T'$ is the center temperature difference caused by the waveguide heating. With the linear temperature distribution, η_{DT}' becomes

$$\eta_{DT}' = \frac{\partial \Delta y(0)}{\partial \Delta T'} = -\frac{1}{2}(\gamma_2 - \gamma_1)\frac{t_1 + t_2}{t_2^2 K} l^2 \cdot \zeta' \tag{4.2.14}$$

where ζ' equals 0.3178 in this study. Here, ζ' is found by comparing the analytical and numerical simulation results. For example, the deflection caused by center temperature 319.56 K on a 12.54 μm long nanobridge is 8.306 nm from equation (4.2.6), while numerical simulation only shows 2.64 nm displacement. Therefore ζ' is calculated as 2.64 / 8.306 = 0.3178. The corresponding η_{DT}' is 0.10 nm/K. $\Delta T'$ as a function of the waveguide input power P_{in} is depicted in Figure 4-17. When the input power is smaller than 500 μW, $\Delta T'$ will be less than 26.41 K, causing at most 2.64 nm self-heating deflection, which is an acceptable value.

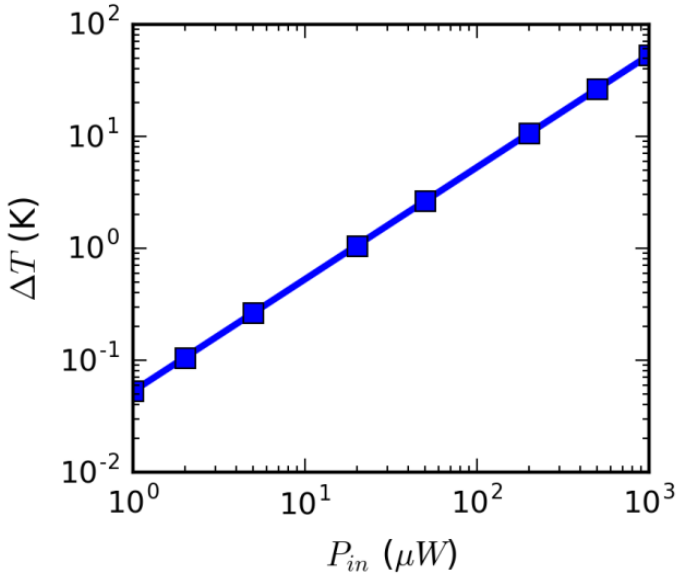

Figure 4-17. The maximum temperature difference $\Delta T'$ at the center of the nanowire as a function of the waveguide input power P_{in}. The gap between the nanowire and the waveguide top surface is 50 nm.

4.2.10 Summary and Comparison of Device Design

In summary, the design procedure is presented in Session 4.2. The design first starts from thermomechanical simulation to find the optimum layer thickness to maximize the deflection. After fixing the layer composition, the unit cell simulation is performed to optimize the length, width and period of the strip antennas. With the chosen period, the photothermal effect of the fishbone nanowire is simulated to find the relation between IR power density and thermal gradient. Thus the conversion ratio from IR power density to maximum temperature difference η_{TI} can be found. From the simulated temperature profile, the deflection caused by thermal coefficient mismatch is investigated next, and so is the conversion ratio from the temperature difference to displacement at the beam center η_{DT}. Knowing the maximum displacement in the radiation *on* and *off* states, the number of the

nanowire is studied to yield the highest change in the waveguide S_{21} parameter (linear scale). By now the device geometry is settled and the FOM of the device is determined by the conversion ratios. Last but not least, the waveguide input power is discussed to avoid self-heating issues. We design two devices at 785 nm and 4.3 μm wavelengths. The performances of the two devices are summarized in the following table.

Table 4-3. Comparison the device parameters and performances at 4.3 μm and 785 nm

Parameters	4.3 μm	785 nm	Notes
L_s	1.77 μm	350 nm	Strip antenna length
W_s	100 nm	100 nm	Strip antenna width
W_b	100 nm	100 nm	Nanobeam width
P_x, P_z	3.1 μm	660 nm	Periods
N_a	6	16	Antenna number
W_w	18.6 μm	12.54 μm	Nanowire width
T_m	20 nm Ni / 30 nm Au	20 nm Ni / 30 nm Au	Nanowire thickness
gap	50 nm	50 nm	Nanowire to waveguide
N_w	9	11	Nanowire number
ΔS_{21}	0.106	0.066	Modulation depth
η_{TI}	33.75 K/(μW/μm^2)	2.175 K/(μW/μm^2)	IR power density to ΔT_{max}
η_{DT}	0.17 nm/K	0.113 nm/K	ΔT_{max} to max displacement
η_{SD}	4.6×10^{-3} /nm	4.3×10^{-3} /nm	max displacement to ΔS_{21}
FOM	2.64×10^{-2} μm^2/μW	1.06×10^{-3} μm^2/μW	Figure of merit
ΔT_{max}	21 K	5.88 K	at P_{in} = 100 μW
ΔT_{max}	104 K	26.41 K	at P_{in} = 500 μW

η_{DT}'	0.16 nm/K	0.10 nm/K	Caused by self-heating

4.3 Device Fabrication

4.3.1 Waveguide Fabrication

Fabrication of the device starts from thermal oxidation of the commercial 4-inch Si wafers (<100>, P-type, 10-20 Ω·cm, 525 μm thickness, Silicon Valley Microelectronics, Inc.). A layer of 4029.7 nm SiO_2 is thermally grown on the Si wafer as the waveguide substrate. The refractive index and extinction coefficient of the film are measured by the ellipsometer (Sopra GES-5) and curved fitted with Cauchy equations.

$$n(\lambda) = 1.448318 + \frac{0.003907}{\lambda^2}$$
$$k(\lambda) = 0.000484 - \frac{0.000254}{\lambda^2} \tag{4.3.1}$$

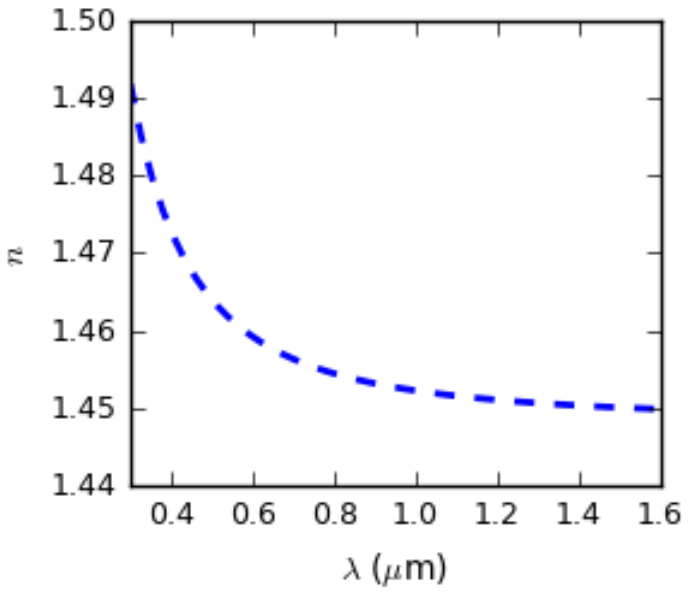

Figure 4-18. Refractive index of the thermally grown SiO_2 film as a function of the wavelength.

The refractive index of the thermally grown SiO_2 film as a function of the wavelength is plotted in Figure 4-18. At λ = 1.55 μm, n = 1.45.

After growing the SiO_2 substrate, A 300 nm Si_3N_4 layer is deposited on top of the substrate using low-pressure chemical vapor deposition (LPCVD) method (Rogue Valley Microelectronics). The layer thickness is measured to be 303.8 nm, provided by the company. The layer refractive index is characterized by Sopra GES-5 ellipsometer and we find that n = 2.09 when λ = 1.55 μm. The refractive index as a function of the wavelength is shown below.

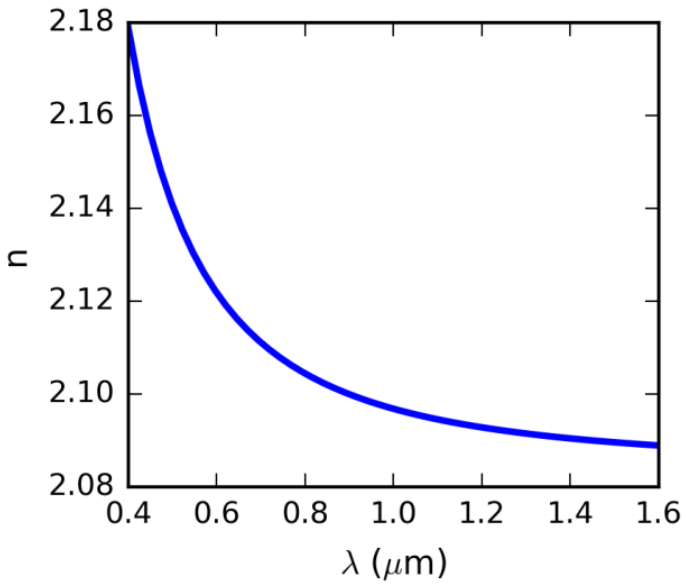

Figure 4-19. Refractive index of the LPCVD Si_3N_4 film as a function of the wavelength.

To fabricate the Si_3N_4 waveguides, the wafers are coated with SPR 700 positive photoresist. The operation is carried out by SVG 8800 track coater because the track coater yields better film uniformity and repeatability than manual operation. Using the stored recipe #1 (Bake 120 °C 15s; Prime 30s; Spin 4400 rpm 30s; Soft bake 95 °C 60s), the

machine coats about 1.2 μm SPR 700 photoresist on the wafer surface. The photoresist is then exposed by Karl Suss MA6 lithography machine in hard contact mode with an exposure time of 3.1s.

The schematic of the waveguide layout is depicted in Figure 4-20. The schematic contains 5×5 dies, each of which has an area of 1.8 cm ×1.8 cm. The diagonal length of the photomask pattern is 5 inch, however, the diameter of the wafer is 4 inch. Therefore, the peripheral patterns may not be located on the wafer or in a low quality. But the center 9 dies are fully located on the wafer and should be of high quality. Each die has 11 group waveguides, and each group has 9 waveguides with their width ranging from 1.1 μm to 1.9 μm. The waveguides are separated by 125 μm space.

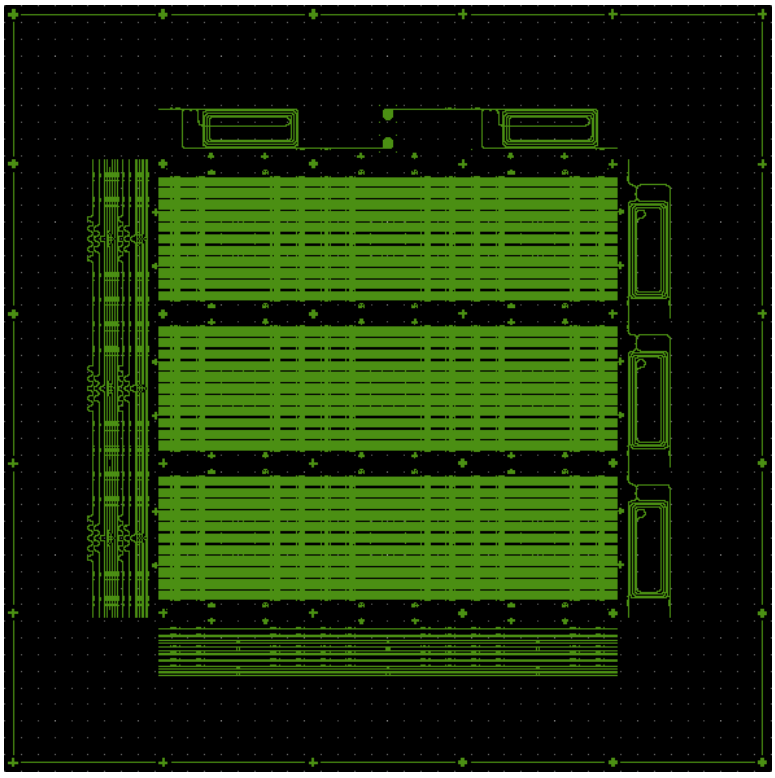

Figure 4-20. Schematic of the waveguide layout.

After being exposed, the wafer is developed by the SVG 8800 track developer machine with the stored recipe #1 (Post-exposure bake 115°C 60s; AZ300T 60s; Hard bake 120°C 60s). The waveguide pattern is then transferred from the photomask to the photoresist. To smooth the photoresist side walls, the developed wafer is descumed in Matrix 105 Plasma Asher at 100 °C for 1 min (Pressure: 3.75 Torr, MFC1 45%, RF power 80W), which results in smoother photoresist side walls. It is worth noting that descum process will also shrink the photoresist mask width by 40 nm. Compared to the designed waveguide width 1.5 μm, 40 nm width reduction is tolerable.

To transfer the waveguide pattern from the photoresist to the Si_3N_4 layer, fluorine reactive ion etching (RIE) method is utilized to etch Si_3N_4 material. The photoresist serves as a mask for Si_3N_4 layer etching. The Si_3N_4 layer is etched 298.6 nm deep with an etching time of 5 min 25s and the recipe Nitride-fast (3 sccm O_2, 30 sccm CHF_3, 0.055 Torr, 200 W RF power). The etching speed of the Nitride-fast recipe is estimated to be 55.13 nm/min. The remaining photoresist is removed by the oxygen plasma etching (Matrix 105 Plasma Asher, recipe: 240°C 3mins 3.75 Torr 45% MCF1, RF power 500 W).

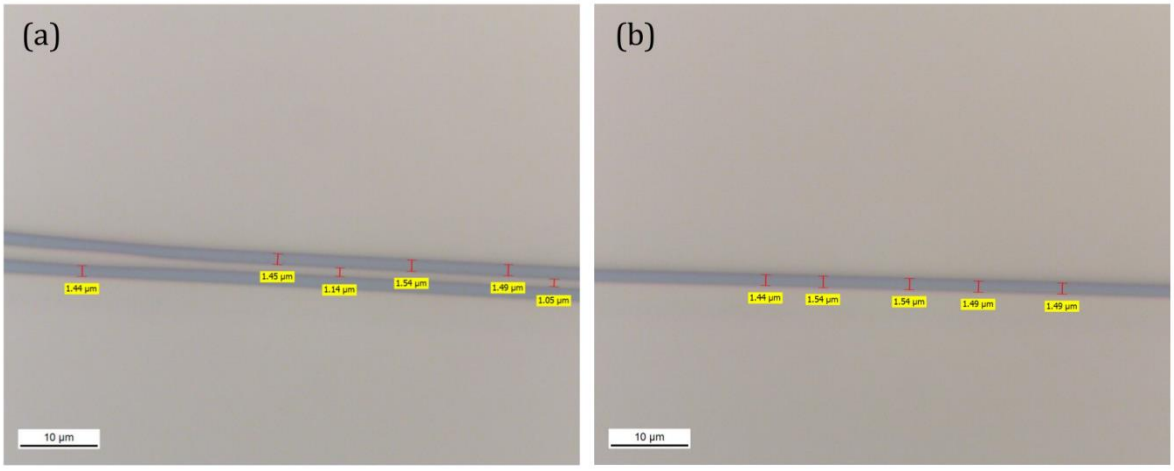

Figure 4-21. (a) Microscope image of the fabricated (a) coupler waveguides and (b) a straight waveguide. The widths of the waveguide and gap are denoted on the pictures.

The microscope image of the fabricated coupler waveguides and straight waveguide are shown in Figure 4-21. The width of the waveguide is about 1.5 μm, while the gap of the coupler waveguides is about 1.1 μm. In the layout design, the measured waveguides are designed to be 1.5 μm and the measured gap is designed to be 1.2 μm. The fabrication results agree well with the designed value.

4.3.2 SiO_2 Sacrifice Layer Deposition and Planarization

To make suspended wires, sacrifice layer must be employed to support the suspended structure first, and then be removed. SiO_2 is used as sacrifice material here due to its ease of deposition and etching. Plasma-enhanced chemical vapor deposition (PECVD) method is used to deposit a layer of 600 nm SiO_2 on the waveguide patterned wafer.

Since the wafer has been patterned with waveguides, the wafer surface will not be flat after depositing 600 nm thick SiO_2 film. Figure 4-22 shows the surface profile of the wafer after depositing the PECVD SiO_2 film, measured by a stylus surface profilometer (Dektak 150, Veeco). The bumps, characteristic waveguide profile, still remain, and their heights are measured to be ~280 nm.

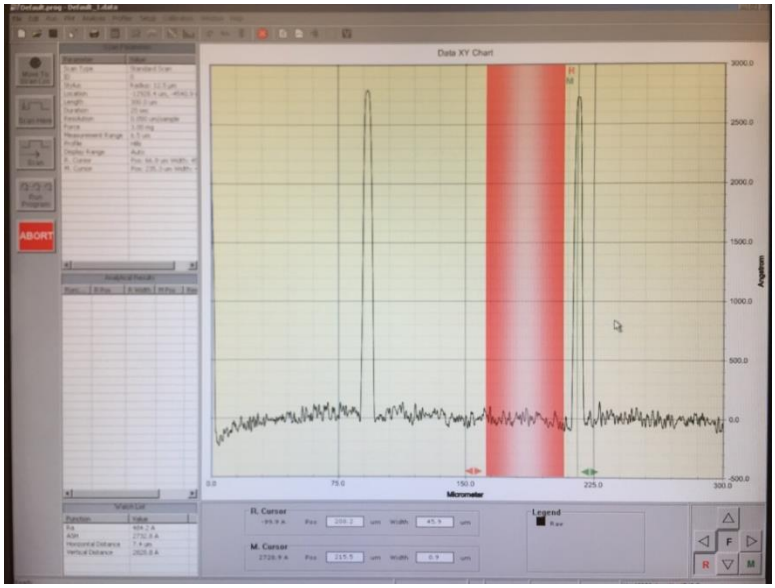

Figure 4-22. The surface profile of the wafer after depositing 600 nm PECVD SiO_2 film.

The bumps should be removed to make a flat platform for the fabrication of the suspension layer. Chemical mechanical polishing (CMP) is used to flatten the wafer surface and to thin the sacrifice layer. For oxide polishing, the slurries are mildly alkaline with a pH value of about 11. The polishing mechanism relies on surface modification of the oxide: leaching of oxide by the slurries softens the top layer, and the mechanical abrasion rate goes up [96]. We apply the commercial slurry that has 20 nm colloidal silica particles (part # 2395.1, ULTRA TEC Mfg. Inc) to the Logitech CDP polishing machine. The parameters of the polishing process are summarized in the following table.

Table 4-4. Settings for chemical mechanical polishing in Logitech CDP machine.

Parameters	Value
Polishing time	3 mins
Slurry feed speed	175 mL/min
Plate speed	10 rpm

Carrier speed	40 rpm
Down load	3 psi, vacuum off
Conditional sweep	on
Sweep frequency	50%
Sweep amplitude	40%

The polishing depth is monitored by measuring the total SiO_2 thickness using the Nanospec film thickness measurement system. Although the SiO_2 in the substrate and the sacrifice layer are fabricated by different methods, thermal oxidation and PECVD methods, and thus have different refractive indices, we treat them as if they had the same refractive index, approximately 1.455. Two sampling methods are used to measure the SiO_2 thickness and characterize the uniformity of the wafers. One is to measure the center of the wafer and 4 peripheral points at the edge of the wafer as shown in Figure 4-23(a). The other one only focuses on the 9 dies regions as demonstrated in Figure 4-23(b). 8 wafers have been polished and characterized by the 5 points and 9 dies methods. Their uniformity is summarized in Table 4-5. Compared to 5 points method, 9 dies method gives smaller thickness variation. Since 9 dies method reflects the actual uniformity of the real device regions, we use the results from the 9 dies method to determine the quality of the polished wafers. If we assume that a uniform wafer should have thickness variation smaller than 60 nm, then 4 out of 8 wafers are considered to be of good quality. Two wafers, #1 and #8, have dirty surfaces after polishing due slurry contamination, thus fail to finish the 9 dies characterization.

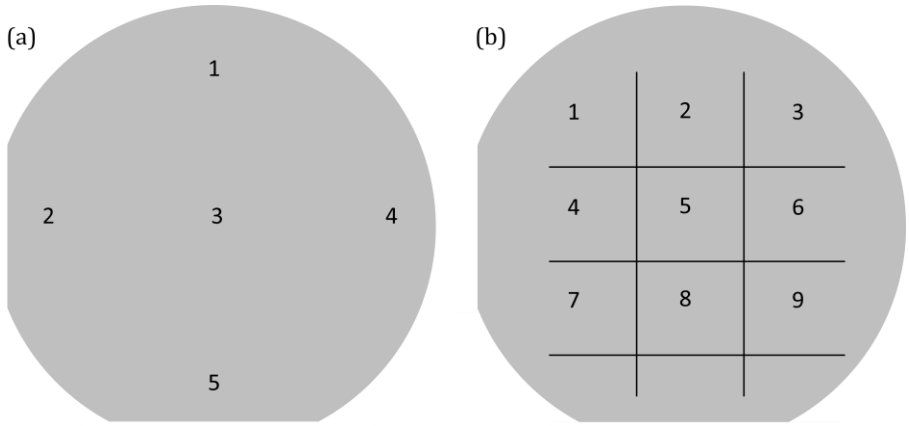

Figure 4-23. Two different methods to characterize the uniformity of the polished wafers.

Table 4-5. Summary of the uniformity of the 8 polished wafers using 5 points and 9 dies methods.

#	Before	5 points			9 dies			Depth	Notes
	Avg (Å)	Center (Å)	Max Δ (Å)	Min Δ (Å)	Avg (Å)	Max Δ (Å)	Min Δ (Å)		
1	46293.8	46392	0	-353					Dirty
2	46251.4	46313	0	-321	46278.33	76.67	-96.33	~0	uniform
3	46351.8	43380	2211	0	43356.89	45.11	-60.89	2994.91	uniform
4	46398.4	43538	379	-1650	43288.11	583.89	-2160.1	3110.29	non uniform
5	46477.8	45616	260	-231	45634.67	211.33	-321.67	843.13	uniform
6	46592.3	43359	0	-527	41610.33	1890.67	-675.33	4981.97	non uniform
7	46537.4	42870	1030	-1166	43383.22	474.78	-494.22	3154.18	uniform
8	46490.2	43910	2996	0					Dirty

For the sake of next fabrication steps, only the uniform wafers, #2, #3, #5 and #7, should be used. However, it is worth mentioning that the polishing depth differs a lot among these wafers due to the randomness nature of polishing. In addition, the polishing

depth is not accurate because of the approximation of the SiO_2 refractive index. Actual etching depth will be measured by potassium hydroxide (KOH) etching after the wafer dicing step.

4.3.3 Wafer Dicing

To avoid using wafer polishing, dry-etching-based dicing method is adopted in the fabrication. The idea is to carve a deep trench on the silicon substrate, and then use the trenches as guidelines when cleaving the wafers. Since the silicon substrate was covered with the silicon oxide and silicon nitride layers, extra steps must be done to open windows in the oxide and nitride layers. To do so, the wafers will go through another lithography cycle to define the dicing patterns on the photoresist. We use AZnoLF 2020 negative photoresist and spin coating process is done by the SVG track coater machine with a modified #2 recipe (AZnoLF 2020, Bake 120 °C 15s; Prime 30s; Spin 1800 rpm 30s; Soft bake 110 °C 60s). The track coater will coat a 3 μm thick photoresist film on the wafers. The photoresist film is then exposed 19 s in the Karl Suss Lithography machine in the hard contact mode. After exposure, the SVG track developer machine is employed to develop the photoresist with a stored recipe #2 (AZnoLF 2020, Post-exposure bake 110°C 60s; MF26A 60s; Hard bake 120°C 60s).

After defining the dicing patterns, the exposed oxide and nitride layers are etched away by the Advanced Oxide Etcher (AOE) with a recipe named OXIDAPIC (C_4F_8 7 sccm, Ar 10 sccm, CHF_3 33 sccm, pressure 10 mTorr, ICP power 700 W, RIE power 200 W). The AOE has a fast etching speed on SiO_2 and Si_3N_4, about 400 nm/min. The desired etching depth was 4.6 μm (4 μm + 600 nm), and the etching time is estimated to be 11 mins 30s. The

etching ratio of the SiO_2 to the photoresist is 2.95. Therefore, it is safe to use a 3 μm photoresist protection layer for 4 μm oxide etching. The residual photoresist is removed by the oxygen plasma.

After the dicing trench windows have been carved out, we still could not etch the silicon substrate without protection on the silicon oxide layer. Since the upper oxide layer in our design was part of devices, they need to be protected during the silicon etching process. The protection layer is the still the negative photoresist AZnoLF 2020. The spin coating and lithography process are the same as the one described above. Silicon is etched by fast deep reactive ion etching (FDRIE) with a recipe named UCLA DSE SMOOTH NANO (He 174 sccm, C_4F_8 10 sccm, H_2 8sccm, pressure 4 MTorr, RIE power200, ICP power 1250). The etching speed was estimated to be ~6.1 μm/min. After 30 mins etching, 186 μm deep trenches are formed. The deeply etched slots divided the wafers into several dies, as shown in Figure 4-24(a).

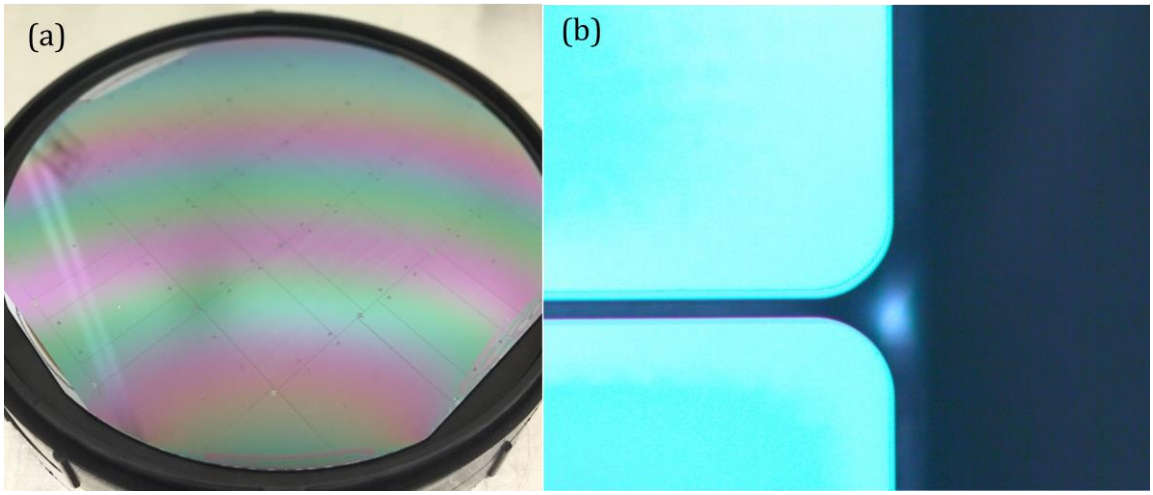

Figure 4-24. (a) the photo of the wafer with deep trenches to divide the wafer into several dies. (b) the edge of a cleaved die.

By using cleaving pliers, the wafers are diced into several dies. Photoresist protection is not removed until cleaving is finished. Then oxygen plasma is used to remove the residual photoresist. By using the dry etching for dicing, the edges of each die can be smooth as shown in Figure 4-24(b).

4.3.4 SiO_2 Sacrifice Layer Thinning

Once the wafer has been diced into pieces, the SiO_2 sacrifice layer can be scrutinized by performing etching and surface profiling on one die. The principle is based on the selective KOH wet etching on SiO_2. The die to be examined will be patterned with a photoresist window, through which KOH aqueous solution can contact and etch the SiO_2 sacrifice layer. Since KOH does not etch Si_3N_4, the waveguide will remain on the sample surface. After removing the protective photoresist layer, surface profiling will be performed to measure the distance between the waveguide top and the surrounding mesas, and then the sacrifice layer thickness can be determined since the waveguide height is known. The examination flow is illustrated as follows.

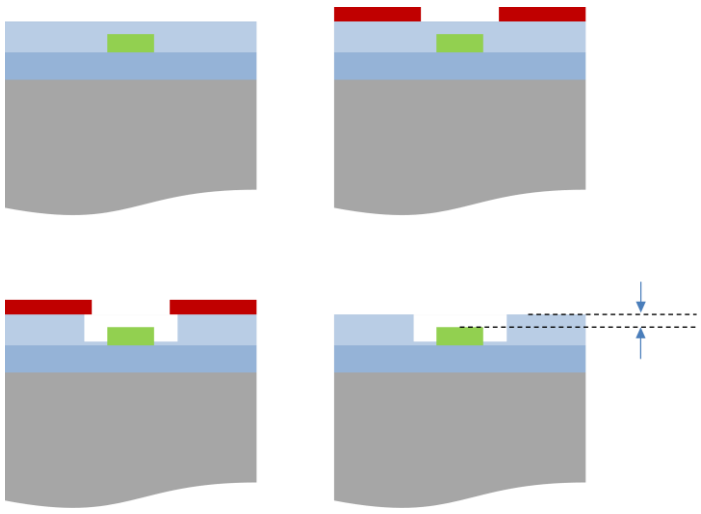

Figure 4-25. The fabrication flow to find the SiO_2 sacrifice layer thickness. The brownish red represents photoresist. The light blue represents PECVD SiO_2 sacrifice layer. The darker blue represents the thermal oxide. The gray represents the Si substrate.

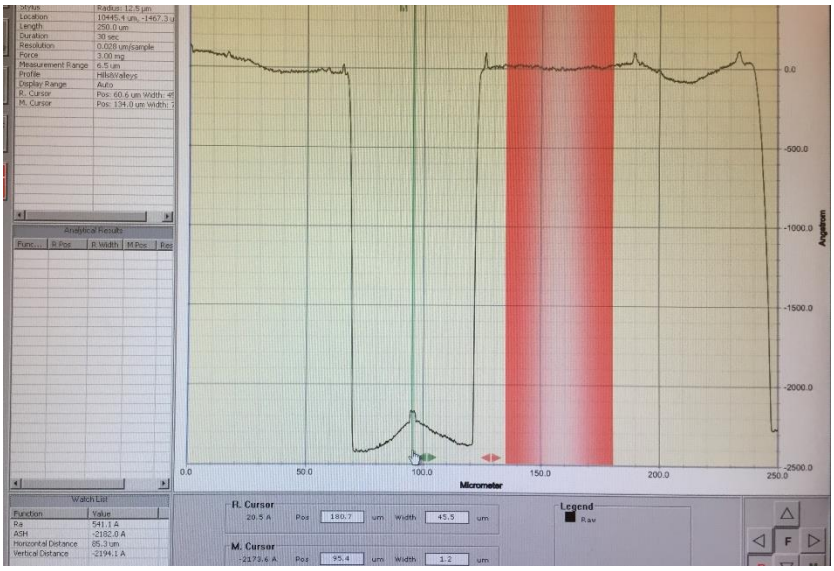

Figure 4-26. The surface profile of the trench and waveguide. The vertical distance between the surrounding mesa and the waveguide top surface is 219.4 nm.

Following the inspection procedure, the vertical distance between the waveguide top surface and the surrounding mesas is found to be 219.4 nm as shown in Figure 4-26. In our design, the vertical distance should be 50 nm. Therefore, the SiO_2 sacrifice layer needs to be thinned by 169.4 nm. Fluorine RIE (Oxford 80) is used for etching SiO_2 layer. The final vertical distance is measured to be 61.96 nm after sacrifice layer thinning.

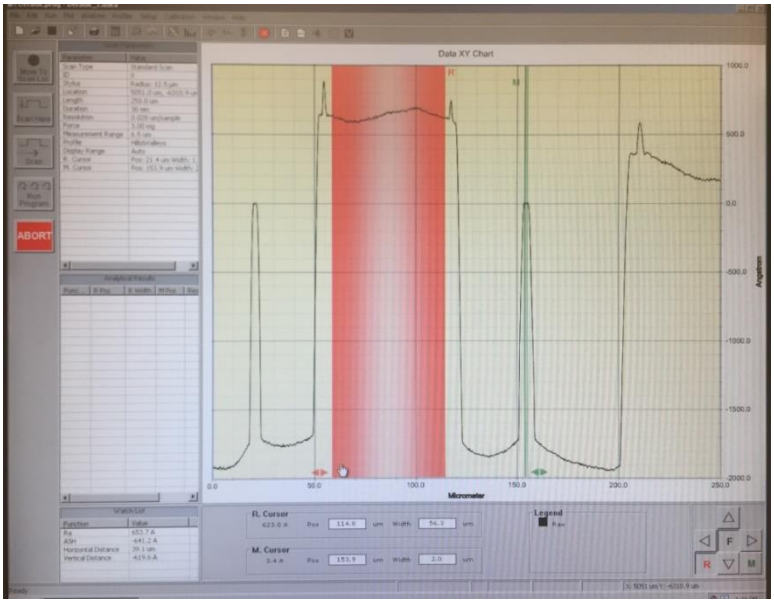

Figure 4-27. The surface of the trench and the waveguide after sacrifice layer thinning. The vertical distance between the waveguide and the surrounding mesa is 61.96 nm.

4.3.5 Fishbone Antenna Fabrication

After planarization and SiO_2 thinning, the dies are ready for the fabrication of the fishbone antennas. However, it is difficult to locate the Si_3N_4 waveguides due to the planarization of the sample surface and low contrast between SiO_2 and Si_3N_4. Therefore, it is necessary to fabricate alignment markers for the subsequent E-beam lithography. The alignment markers are 20 μm × 20 μm squares, defining the region to be exposed by the electron beams. To be successfully identified by the Ebeam writer machine, the alignment markers should be made of Au and be at least 100 nm thick. The fabrication flow of the alignment markers is summarized in the following table.

Table 4-6. The fabrication flow of the Ebeam alignment markers

Steps	**Parameters**

Photoresist coating	Spin coater AZnoLF 2020 (step1: speed 500/ ramp 100/ time 5s; step2: speed 4000/ ramp 1000/ time 45s; step3: speed 1000/ ramp 1000/ time 5s; step4: speed 0/ ramp 500/ time 0)
Lithography	Karl Suss hard contact, exposure time 6.5s
Photoresist Develop	Post-exposure bake 110°C 60s; MF26A 60s; Hard bake 120°C 60s
Ebeam Metal Deposition	3 nm Ti, 100 nm Au
Liftoff	NMP (1-methyl-2-pyrrolidone) soak @ 80 °C, magnetic swirl 300 rpm: 2 hr
Wafer Cleaning	Acetone 30 s; Methanol 30 s; Isopropanol 30 s; DI water 30 s;

The Ebeam alignment marker should be successfully identified in the SEM machine as shown in Figure 4-28.

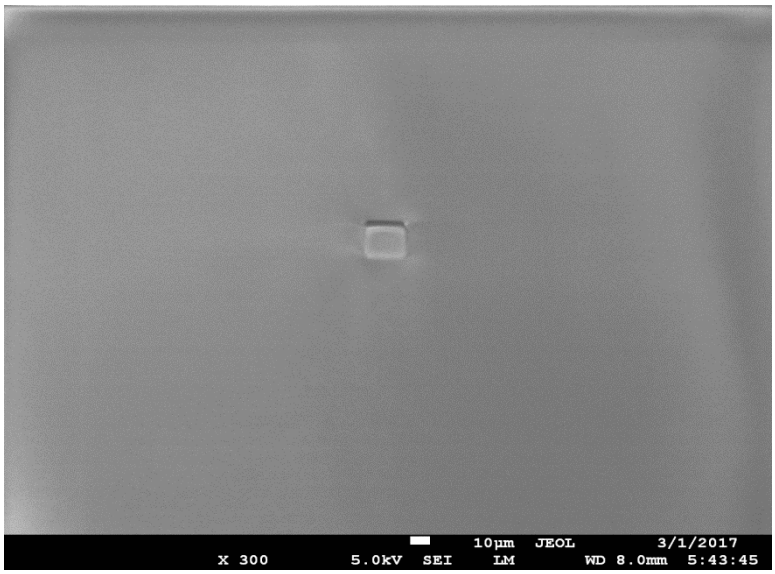

Figure 4-28. SEM image of one Ebeam alignment marker.

Besides fabricating Ebeam alignment markers, dose test is inevitable to optimize the electron beam exposure dose, so that the dimension of the fabricated pattern matches the design. We perform the dose test on a separate sample which has the same substrate

composition and thickness. Specifically, we compare the parameters of strip length L_s, strip width W_s and beam width W_b as described in Figure 4-4. The influence of the dose on the fishbone antennas is illustrated in Figure 4-29. When the dose is 1100 $\mu C/cm^2$, the measured L_s, W_s, and W_b are close to their designed values of 350 nm, 100 nm, and 100 nm, respectively. Thus, 1100 $\mu C/cm^2$ is chosen as the optimum value for real fishbone antenna fabrication. Figure 4-30 depicts the SEM image of a test sample with 1100 $\mu C/cm^2$. The beam width W_b, antenna width W_s, antenna length L_s, and period P_x and P_y are measured to be 106 nm, 109 nm, 348 nm, 671 nm and 665 nm, respectively, close to their designed value, 100 nm, 100 nm, 350 nm, 660 nm, and 660 nm.

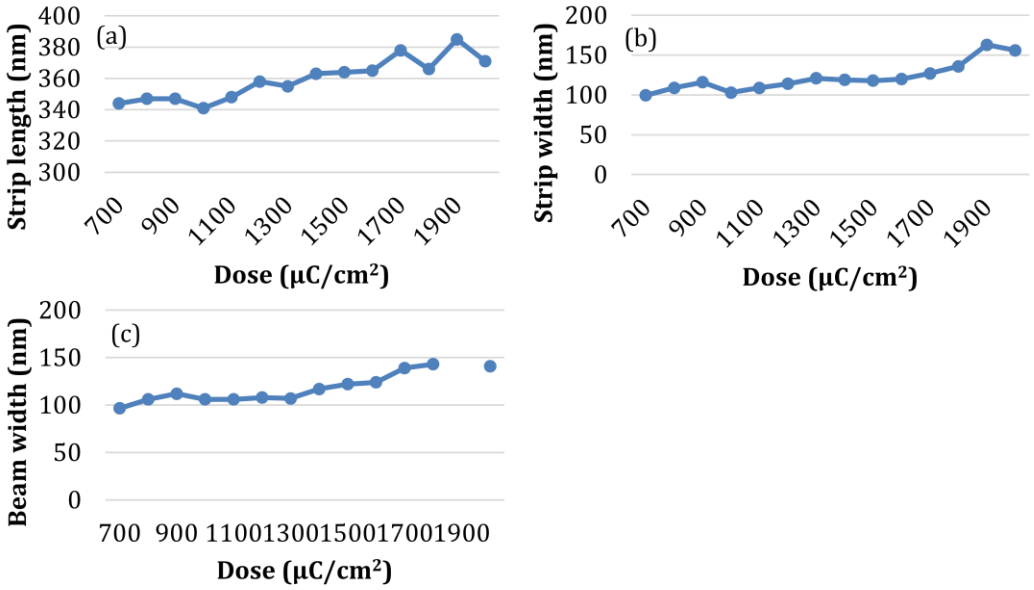

Figure 4-29. The (a) strip length L_s, (b) strip width W_s, and (c) beam width W_b as functions of the electron beam dose.

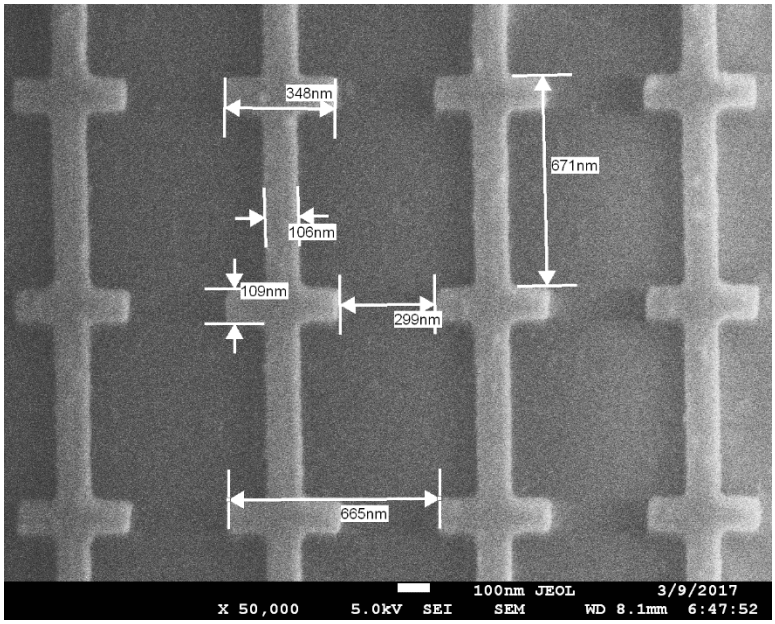

Figure 4-30. SEM image of the fabricated fishbone nanowires in dose test experiments. The sample is fabricated with a dose of 1100 μC/cm^2. The measurements show that the dimensions of the nanowires are close to their designed values.

Similar to fabricating Ebeam alignment marker, the fabrication of the fishbone antennas starts with the spin coating of the PMMA 495 A4 (MicroChem) photoresist. After a layer of about 237 nm PMMA film has been coated on the sample and baked at 180°C for 15 mins, the sample is exposed by the electron beam with a dose of 1100 μC/cm^2. The alignment of the patterns will be automatically performed by the Ebeam writer machine as long as the alignment markers can be identified. The photoresist film is then developed in a mixed solution of MIBK (Methyl isobutyl ketone) and IPA (isopropanol) with a ratio of 1:3 for 60 s followed by being rinsed in IPA for 30s and blow dried with an N_2 gun. 3 nm/20 nm/30 nm Ti/Ni/Au layers are deposited sequentially by the Ebeam metal deposition machine (CHA solution). The microscope image of the photoresist patterns is shown in Figure 4-31. The sample is then immersed in N-Methyl-2-pyrrolidone (NMP) solvent at 80°C for 2 hrs with

magnetic stirring (300 rpm) to lift off the metal. After taking the sample out the NMP solvent and flush the sample with acetone, the sample is cleaned in DI water and blow dried by N_2 gun. The microscope image of the fishbone antenna wires after liftoff is shown in Figure 4-32.

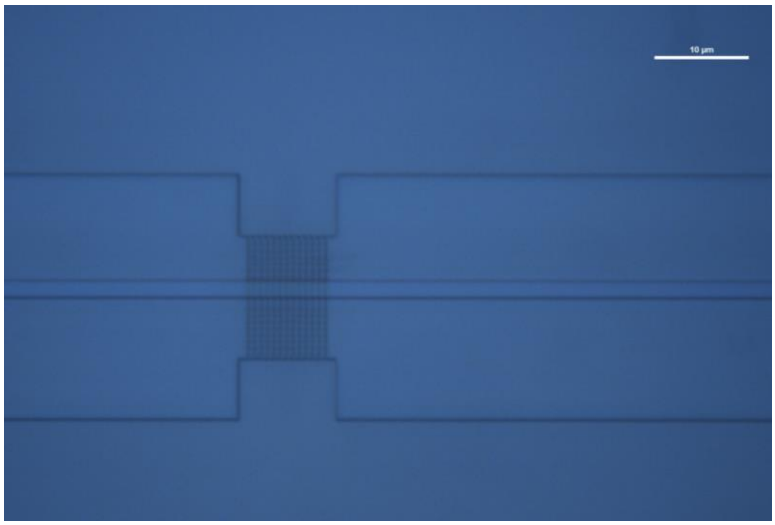

Figure 4-31. Microscope image of the fishbone antenna nanowire array patterns after developing the PMMA 459 A4 photoresist.

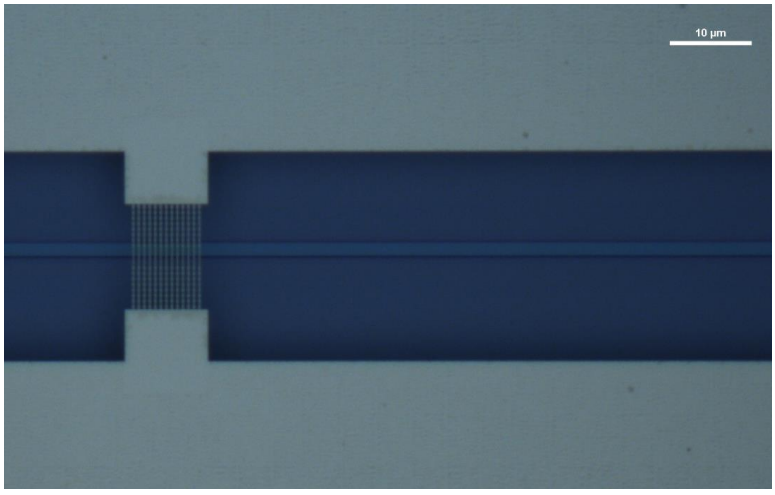

Figure 4-32. Microscope image of the fishbone antenna nanowire array patterns after metal liftoff.

The fishbone patterns are sitting on the SiO_2 sacrifice layer. To make the wires suspended, the sacrifice layer needs to be etched away. Wet etching is preferred because of its isotropy which guarantees to remove SiO_2 in the gap between the wire and the waveguide top surface. Hydro fluoride (HF) acid etches fast on SiO_2 but slowly on Si_3N_4, and thus is used to remove the sacrifice layer. To avoid nanowire sticking to the waveguide top surface, HF vapor etching is preferred over aqueous etching. In HF vapor etching, the etching speed is controlled by the temperature difference between the mounting plate and the ambient air. It is worth noting that the etching speed is not stable and thus a minimum 3 mins etching time is required to reach a steady state. The etching depth is monitored by using the surface profiler to measure the Si_3N_4 waveguide height since the Si_3N_4 can be viewed as intact during HF etching. If the required etch depth is not achieved, another round HF vapor etching has to proceed. Sometimes, several rounds of the etching process may be needed. The final waveguide height is measured to be 292.3 nm as shown in Figure 4-33, indicating an etching depth of 354.26 nm. Since the nanowire beam width is smaller than 150 nm and the etching is isotropic, the SiO_2 in the gap between the nanowire and the waveguide should be etched away.

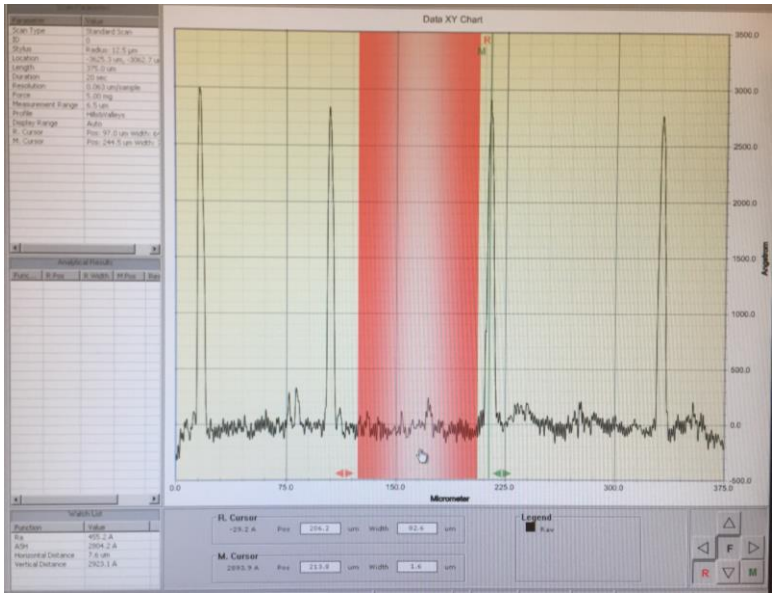

Figure 4-33. The surface profile of the Si_3N_4 waveguides after HF vapor etching.

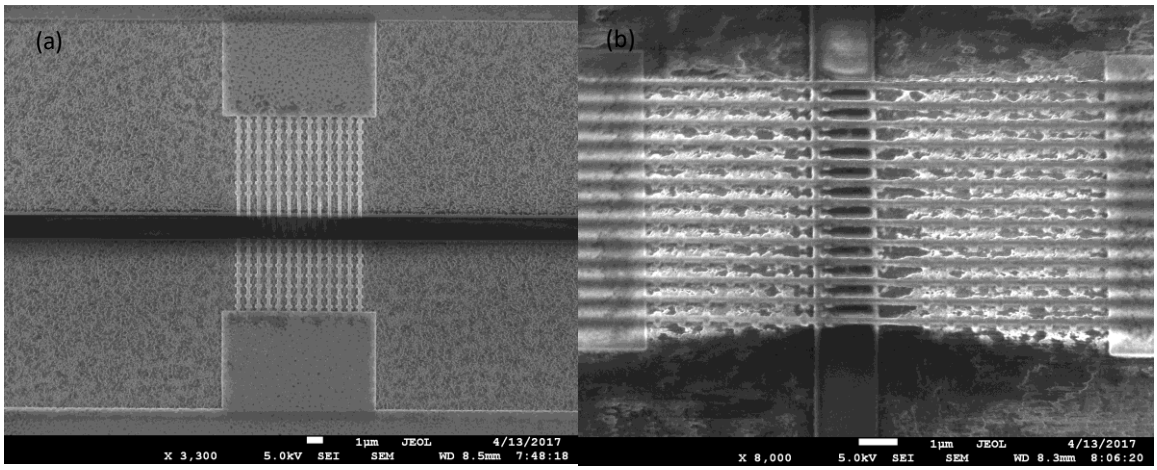

Figure 4-34. (a) Top view and (b) 30° tilted view of a fabricated device.

The SEM images of the final device are shown in Figure 4-34 in both top view and 30° tilted view. The wires are suspended successfully without any breakage indicating the current structure can endure the mechanical stress. The antennas can be clearly identified and the corners are not blunt. The SiO_2 sacrifice layer has been etched away leaving the Si_3N_4 waveguide. Even though the substrate surface is rough due to the HF etching process,

the waveguide surface is relatively smooth. Therefore a low waveguide propagation loss is expected. There is an 800 nm offset between the nanowire array center and the waveguide center line, causing one column of the antennas suspending above the waveguide edge. The misalignment attributes to the auto-alignment program in the Ebeam writer machine, which can be improved by adding more local markers and increasing the thickness of the Au marker for better contrast.

4.4 Device Characterization

4.4.1 Measurement Setup

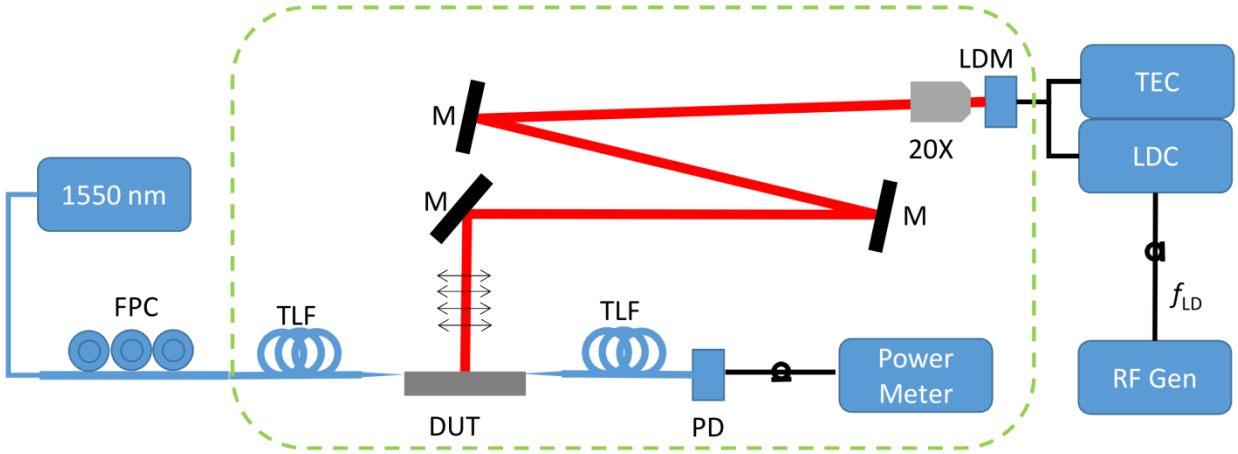

Figure 4-35. Schematic of the experiment setup. 1550 nm: CW laser at 1550 nm wavelength; FPC: fiber polarization controller; TLF: tapered lensed fiber; DUT: device under test; PD: photodiode; M: mirror: 20X: objective lens with 20X magnification; LDM: laser diode mount; TEC: temperature controller; LDC: laser diode controller; RF Gen: radio frequency function generator. The dashed circle encloses the setups that are protected by an air chamber.

Since the device has suspended structures, it is critical to avoid dust stuffing into the gaps between the nanowires and the waveguide top surface. Thus, a laminar flow chamber (PURAIR FLOW-48, Air Science) is used to protect the device and the main setups from dust.

The air flow chamber is equipped with ultra-low particulate air (ULPA) filters that guarantee to capture > 0.12-micron particles with 99.999% efficiency. A continuous wave (CW) laser operating at 1550 nm wavelength serves as the source to provide the probe light. The probe light is coupled into the waveguide via a tapered lensed fiber (TLF, TSMJ-3A-1550-9/125-0.25-7-2.5-14-2-AR, OZOptics). A fiber polarization controller (FPC) is inserted between the laser source and the TLF for polarization manipulation to maximize the coupling. The output light from the waveguide is collected by another TLF with the same model, and the collected power is measured by an optical power meter (1830-C, Newport). In the frequency response experiment, an extra lock-in amplifier (SR510, Stanford Research System) is inserted after the power meter to measure the analog output (not shown in Figure 4-35). The signal light is provided by a laser diode (LD, HL6545MG, Thorlabs) that is mounted in a laser diode mount (LDM, TCLDM9, Thorlabs) which is controlled by a temperature controller (TEC, TED 200C, Thorlabs) and a laser diode controller (LDC, LDC 202C, Thorlabs). A function generator (AFG3102, Tektronix) provides modulation to the LDC to vary the LD current. The generated laser is collected and collimated by an objective lens (20X, NA 0.45, Newport), and then redirected to the chip surface with the help of three mirrors. The radiation beam, or the target beam, is normally incident to the device surface and its polarization aligns with the antenna directions.

The experiment was carried out by using an LD (HL6545MG, Thorlabs) with a wavelength of 660 nm and a tunable optical power up to 120 mW. The reason for using 660 nm wavelength instead of 785 nm wavelength is attributed to two reasons. Due to the mismatch between the fabrication and the design, the spectral response of the fishbone nanowire is blue shifted. In our preliminary tests, the detector could respond to white LED

but not 785 nm laser. Another factor limiting the choice of the LD is power. The 660 nm LD has a nominal power of 120 mW while our 785 nm laser (LP785-SF20, Thorlabs) has a maximal power of 20 mW. Since higher power gives more flexibility for optical characterization while low power may not trigger the device and generate enough signals to beat noise, therefore, the high power 660 nm LD is preferred for the demonstration purpose. In our experiment, 88 mW collimated beam power out of 120 mW LD power can be extracted with an efficiency of 73%. It is worth noting that the choice of the detection wavelength does not change the device operating principle. The detector geometry can also be scaled to accommodate other wavelengths.

4.4.2 Detector Frequency Response

In the frequency response test, a lock-in amplifier (SR510, Stanford Research System) is utilized to lock the power at a certain frequency which is synchronized to the function generator. The function generator provides the same signal, 3 V_{pp} sine wave with 0 offset, to both the lock-in amplifier and the LDC. The LDC keeps a constant current of 110 mA. When it is subject to the sinusoidal modulation, the LDC produces a current fluctuation from 50 mA to 170 mA, corresponding to a radiation power variation from 27 μW to 88 mW. The 660 nm radiation light regulates the waveguide output power that is collected by the power meter. The analog output of the power meter is fed into the lock-in amplifier to link up the synchronization loop. The bandwidth of the power meter depends on the optical power. At microwatt level, the power meter has a bandwidth above 1.5 kHz, which is fast enough for our experiment.

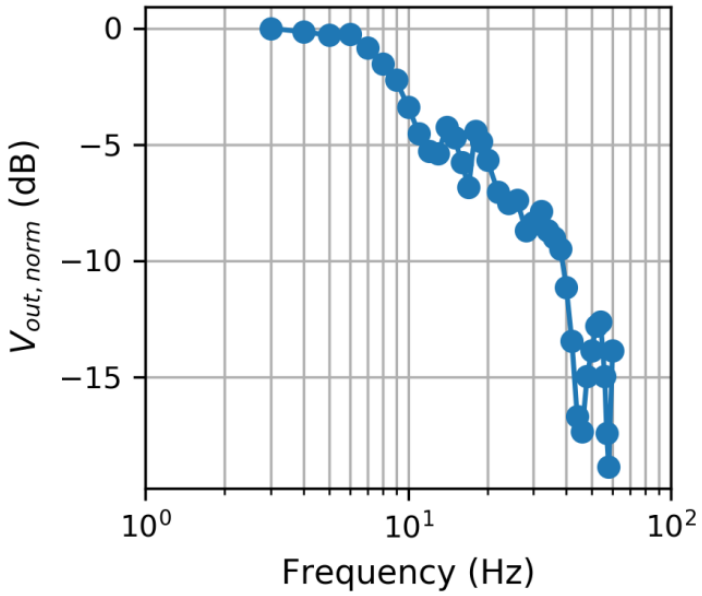

Figure 4-36. Normalized output voltage as a function of the modulation frequency.

By tuning the modulation frequency and recording the voltage reading from the lock-in amplifier, the frequency response of the detector is illustrated in Figure 4-36. Since the photodiode converts the optical power into current which is then converted to voltage with the transimpedance amplifier in the power meter, the voltage reading is proportional to the optical power. From the Bode plot, the 3 dB cutoff frequency, f_{3dB}, is found to be 9.6 Hz corresponding to a time constant $\tau = 1/(2\pi f_{3dB}) = 16.6$ ms. The time constant, τ, like other thermal IR detectors [84], [97], is on the order of milliseconds.

4.4.3 Detector Responsivity

Another important characteristic for the detector is its responsivity, which characterizes how efficiently the detector can respond to optical signals and convert to

measurable quantities. Here, the measurable quantity is the waveguide output power whose fluctuation corresponds to the optical radiation variation.

The experiment is implemented as follows. An electrical sine wave with 0.05 Hz is applied to the LDC generating a sinusoidal light. Using the modulated light instead of the static light can help avoid power drift problem that is often caused by the instability of the mechanical stages. On the other hand, the slowly modulated signal resembles the dc condition, which is representative for the characterization of the device quasi-dc performance. The waveguide output power is monitored and collected with a sampling speed of 10 Hz, fast enough to capture the modulation feature. By tuning the dc current of the LDC and the electric signal amplitude, the target light power can be altered and thus the sensitivity of the device to different power level can be found. Figure 4-37 shows the waveform of the waveguide output power, $P_{\mathrm{wg,\,out}}$, as a function of time and target light power, P_{R}. The traces are biased at different positions for clarity. In fact, all the traces have similar average power around 43 μW. The ticks on the right y-axis label the target light amplitudes. As the radiation power becomes larger, the waveform of P_{wg} shows a clear sign of the modulation. The case when P_{R} is 0 corresponds to the non-illumination condition. Under such condition, the detector is in free-running status, and fluctuation of the $P_{\mathrm{wg,out}}$ is caused by noise.

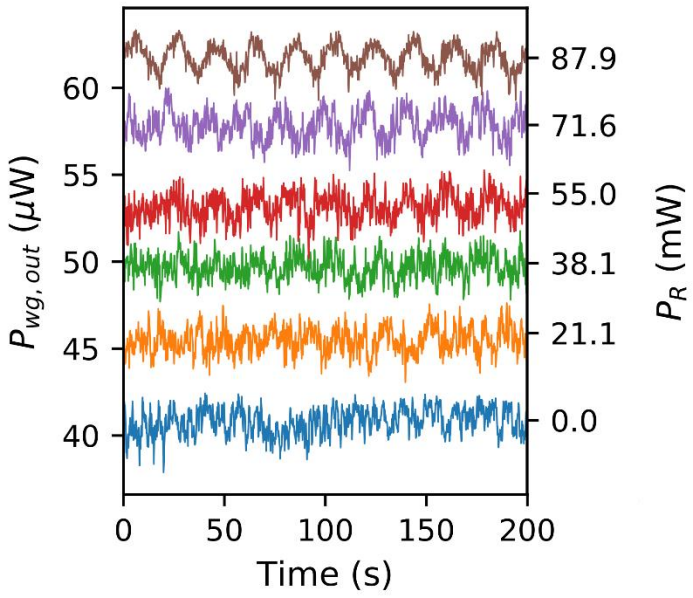

Figure 4-37. Time traces of the waveguide output power $P_{wg,\,out}$ as a function of time and the radiation power P_R. Time traces of $P_{wg,\,out}$ at different biases should have similar average power but are offset along the *y*-axis for clarity. The ticks in the right *y*-axis label the target light amplitudes used in the experiments. Tick 0 represents the non-illumination case.

To quantify the responsivity of the detector, the ratio of the modulation index on the waveguide output power to the radiation intensity is employed. By taking the Fourier transform of the temporal waveforms, the coefficient at the modulation frequency, 0.05 Hz, can be found. The modulation index is calculated by normalizing the coefficient at +0.05 Hz to its dc coefficient, which is equivalent to one half of the ratio of modulation amplitude (*max-min*) to the waveform average value. The spot diameter of the radiation beam is estimated to be 300 μm. Since the spot size is much larger than the device area (12.54 μm × 10 μm), and the beam is assumed to follow Gaussian profile, the light intensity that the device receives is treated to be equal to the peak intensity in the center of the beam, governed by the following equation

$$I_p = \frac{P_{avg}}{\pi w^2 / 2} \tag{4.4.1}$$

where P_{avg} is the average optical power, w is the beam radius and I_p is the peak intensity. Guided by the definition, the sensitivity of the detector is plotted as follows.

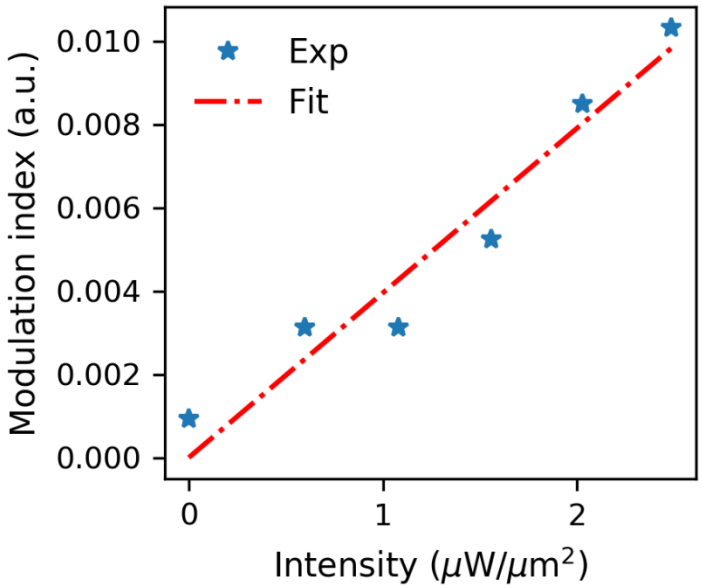

Figure 4-38. Modulation index as a function of the peak intensity. The inset shows the definition of the modulation index. Only positive frequency is used in the calculation.

As can be seen from Figure 4-38, the fitted curve (red dashed line) has a slope of 0.003954 $\mu m^2/\mu W$, which is the responsivity of the device, indicating that 1 $\mu W/\mu m^2$ radiation intensity change will result in an increment of 0.003954 modulation index. Theoretically, the case when there is no intensity should have zero modulation index, but in fact, exhibits non-zero value that is caused by noise. The noise performance and noise equivalent power of the detector are analyzed in the next session.

4.4.4 Noise Equivalent Power

Noise equivalent power (NEP) is the common metric that quantifies a photodetector's sensitivity or the power generated by the noise source. It is defined as the input signal power that results in a signal-to-noise ratio (SNR) of 1 in a 1 Hz output bandwidth. In our characterization, the SNR is examined in frequency domain due to the ease of band filtering. Fourier transform is applied to the temporal waveform when there is no radiation (blue curve in Figure 4-37). Since the variation also depends on the power level, a higher power may have larger variation, the relative variation rather than the absolute variation should be used for fair comparison. To quantify the relative variation, the frequency components are scaled to it dc component for normalization.

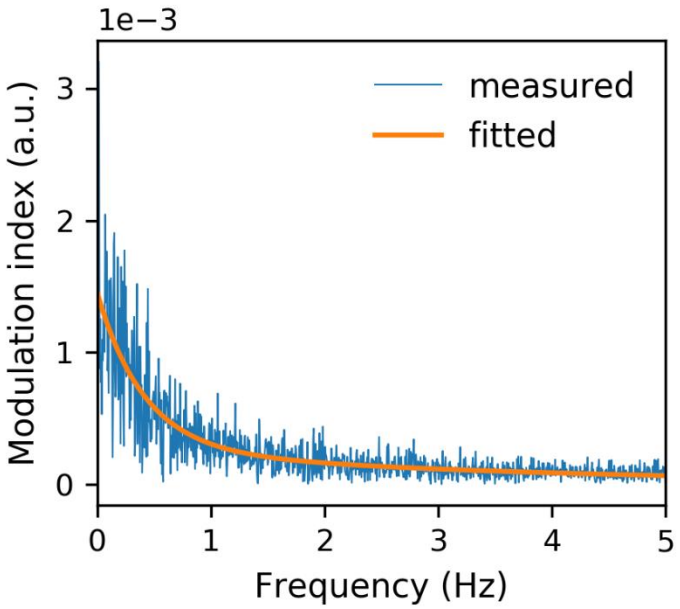

Figure 4-39. The modulation index (normalized noise power spectrum) as a function of the frequency.

Figure 4-39 presents the noise modulation index, also known as the normalized noise power spectrum, as a function of frequency. Since the sampling speed is 10 Hz, the

bandwidth of the whole system is 5 Hz. The averaged noise modulation index within 5 Hz is 2.44×10^{-4}. To achieve SNR =1, the radiation-induced modulation index should be at least the same as the averaged noise modulation index, which requires the minimum radiation intensity to be 0.0617 μW/μm^2. Take the device area into consideration, the NEP is $0.0617\times12.54\times10/\sqrt{5}$ = 3.46 μW/$\sqrt{\text{Hz}}$. A close scrutiny shows that there are significant low-frequency components, which may come from $1/f$ noise, contributing to the total noise. To reduce the impact caused by the $1/f$ noise, the noise modulation index is averaged at 4 Hz within 1 Hz bandwidth, which yields 9.5×10^{-5}. The corresponding NEP is $9.5\times10^{-5}/3.945\times10^{-3}\times12.54\times10/\sqrt{1}$ = 3.02 μW/$\sqrt{\text{Hz}}$, lower than the previous value because of the reduction of $1/f$ noise.

4.4.5 Noise Sources

There are two main sources for the noise, namely, device noise and system noise. The fundamental sources of the device noise are the thermal fluctuation noise, background fluctuation noise, and thermomechanical noise. The system noise can be attributed to laser relative intensity noise, detector noise, and mechanical vibration noise.

4.4.5.1 Device Noise

The thermal fluctuation noise accounts for the random fluctuation in temperature due to the statistical nature of heat exchange between the nanowires and the environment [98].

$$\overline{P_{th}} = \sqrt{4k_B T^2 G} \tag{4.4.2}$$

where k_B is the Boltzmann constant 1.38×10^{-23} m^2·kg·s^{-2}·K^{-1}. The ambient temperature T is assumed to be 300 K. G is the total thermal conductance from the suspended nanowire to

the environment: $G = 13G_{wire} + G_{bottom} + G_{top}$. G_{wire} stands for the conductance through the beam, $G_{wire} = 4w(k_{Au}t_{Au}+k_{Ni}t_{Ni})/l$. Here w is the nanowire width. l is the wire length, k_{Au} =170 W/(m·K) [99] and k_{Ni} = 60 W/(m·K) [100] are the thermal conductivity of the gold and nickel film, and t_{Au} and t_{Ni} are the film thickness of the gold and nickel, respectively. The single wire thermal conductance is multiplied by 13 because there are 13 wires in the device. G_{bottom} accounts for the heat convection through the air gap to the substrate. Though air and SiO_2 are good thermal isolators, they still conduct a significant amount of heat due to the thin film thicknesses. Assuming that the bottom Si substrate acts as a heat sink, the heat transfer coefficient h_{bottom} is estimated to be 5.6×10^4 W/(m²·K) from the following equation.

$$\frac{1}{h_{bottom}} = \frac{1}{h_{air}} + \frac{1}{h_{SiO_2}} \tag{4.4.3}$$

where $h_{air} = k_{air} / t_{air}$, k_{air} is the air thermal conductivity and is 0.024 W/(m·K), t_{air} is the air gap and is 360 nm. $h_{SiO2} = k_{SiO2} / t_{SiO2}$, k_{SiO2} is the SiO_2 thermal conductivity and is 1.4 W/(m·K), t_{SiO2} is the SiO_2 film thickness and is 4 μm. Then $G_{bottom} = A_D \cdot FF \cdot h_{bottom}$. A_D is the device area and is 12.54 × 8.58 μm². Since the wires are periodically spaced and only the wire area will exchange heat, the filling factor FF is required to rule out the spacing. FF equals 0.2 in our design. The same ideal can be applied to the wire top surface thermal conductance, $G_{top} = A_D \cdot FF \cdot h_{top}$, here the top environment is semi-infinite air, so h_{top} is 10 W/(m²·K). The total thermal conductance $G = 13\times2\times10^{-7} + 1.2\times10^{-6} + 2.15\times10^{-10} = 3.8\times10^{-6}$ W/K, and $\overline{P_{th}}$ =4.345 pW/√Hz.

The fluctuation noise originates from the radiative heat exchange with the environment. It can be regulated by the following equation

$$\overline{P_{rad}} = \sqrt{16 A_D \cdot FF \cdot \varepsilon \sigma k_B T^5} \tag{4.4.4}$$

where σ is the permittivity which is assumed to be 1, σ= 5.67×10^{-8} W·m^{-2}·K^{-4} is the Stefan-Boltzmann constant. T = 300 K. $\overline{P_{rad}}$ is found to be 25.57 fW/√Hz.

The thermo-mechanical noise comes from the random vibration of the nanowire. The vibration noise in y-direction $\overline{y_{vib}}$ arising from the thermal energy can be calculated as [101]

$$\overline{y_{vib}} = \sqrt{\frac{4k_B T}{mQ} \frac{\omega_0}{\left(\omega^2 - \omega_0^2\right)^2 + \left(\omega\omega_0/Q\right)^2}} \tag{4.4.5}$$

where ω_0 is the resonant frequency. Q is the quality factor. Q =3.054×10^6 and ω_0 =8.169×10^5 Hz are extracted from simulations (COMSOL Multiphysics). m is the effective mass. For the off-resonance vibration when $\omega \ll \omega_0$, the vibration noise can be simplified as

$$\overline{y_{vib}} = \sqrt{\frac{4k_B T}{k\omega_0 Q}} \tag{4.4.6}$$

where $k = m\omega_0^2$ is the spring constant of the nanowire. For a point-loaded double-clamped beam at the center, its spring constant is [102]

$$k = \frac{\pi^4}{6} \frac{Ewt^3}{L^3} \tag{4.4.7}$$

Here $E = \left(E_{Au} t_{Au} + E_{Ni} t_{Ni}\right) / \left(t_{Au} + t_{Ni}\right)$ is the equivalent Young's modulus of the nanowire, and it equals 126.8 GPa. $t = t_{Au} + t_{Ni}$ is the thickness of the nanowire. L is the length of the wire. k is calculated to be 0.013. Correspondingly $\overline{y_{vib}}$ =0.7145 fm/√Hz.

Recall from Session 4.2.9 that η_{TI} = 2.175 K/(μW/μm^2) is the temperature-IR power density conversion ratio and η_{DT} = 0.113 nm/K is the displacement-temperature

conversion ratio, the noise equivalent power induced by thermo-mechanical noise can be deduced from

$$\overline{P_{vib}} = \frac{\overline{y_{vib}}}{\eta_{DT}\eta_{TI}} A_D \tag{4.4.8}$$

where $\overline{P_{vib}}$ is the noise equivalent power and is 312.7 pW/√Hz.

The total noise equivalent power from the detector itself is

$$\overline{P} = \sqrt{\left(\frac{\overline{P_{th}}}{C_{absp}}\right)^2 + \left(\frac{\overline{P_{rad}}}{C_{absp}}\right)^2 + \overline{P_{vib}}^2} \tag{4.4.9}$$

where C_{absp} is the antenna absorption coefficient (Session 4.2.4) and is assumed to be 0.35 (Figure 4-11). The total noise equivalent power and its components are summarized in the following table

Table 4-7. Total noise equivalent power and its components from the device.

Thermal fluctuation	**Background fluctuation**	**Thermomechanical**	**Total**
12.41 pW/√Hz	73.06 fW/√Hz	312.7 pW/√Hz	312.9 pW/√Hz

It is worth noting that the NEP from the device is a lower boundary estimation, because the *Q* factor of the nanowire should be much smaller due to thin-film gas damping and surface imperfections, whereas only the thermoelastic damping is considered in simulations. Thermomechanical noise is dominant among all the device noise sources and can be reduced by shortening the wire length.

4.4.5.2 System Noise

Besides the noise from the detector, noise from the experiment system also affects the measurements. During the experiment, the system noise originating from the waveguide coupling is found to be the most detrimental. The following figure compares the normalized noise spectrums of the collected power (a) from laser directly, (b) passing through a waveguide without an antenna, and (c) passing through a waveguide with antennas but not exposed to radiation.

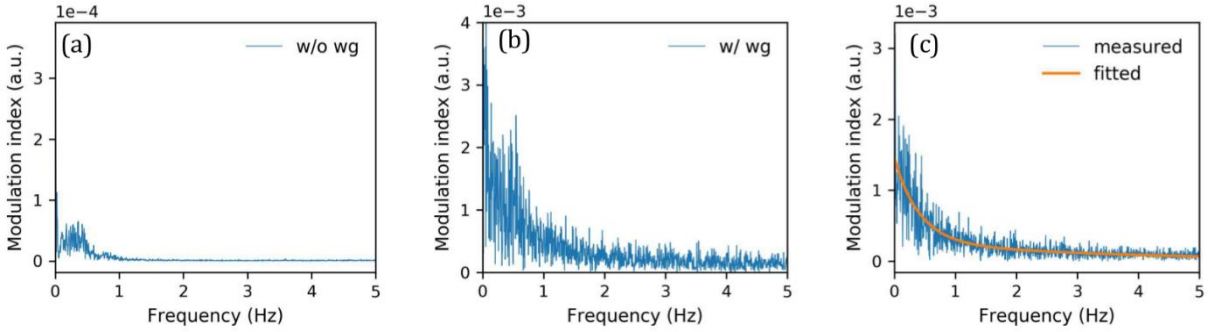

Figure 4-40. The normalized noise spectrums of (a) directly measured the laser power, (b) optical power coupled from a waveguide without antennas, and (c) optical power coupled from a waveguide with antennas but not exposed to radiation. (c) is the same as Figure 4-39.

Figure 4-40(a) reflects the noise spectrum of the laser and the optical power meter. Compared to Figure 4-39, the noise spectrum is one order of magnitude smaller, thus the laser and optical power meter are not the main sources of the system noise. Instead, the coupling noise arising from the vibration of the tapered lensed fiber is the ruling source as shown in Figure 4-40(b). The vibration is even exaggerated by the fan in the laminar flow chamber. The noise spectrum of the optical power in Figure 4-40(b) is in the same order as in Figure 4-40(c), indicating that the waveguide coupling is the main noise source.

The noise equivalent power of the device mainly comes from the system, to be specific, the waveguide coupling. Because the laminar flow chamber sits on the optical table, the mechanical vibration of the fans is conducted to the optical table which affects the performance of the optical components, especially the waveguide butt-coupling. Since the TLF extrudes over the mounting stage, it acts as a cantilever. The vibration-induced displacement of the TLF will jeopardize launching light into and collecting light out of the waveguide. Turning off the laminar flow chamber can remove the noise source, but it also loses the protection of the device from dust. Putting the device into a vacuum chamber can be a better solution in the future, provided that the fibers and cables can access the chamber.

4.5 Summary

In this chapter, we discussed the structure of the fishbone nanowire unit cell, the settings of the electromagnetic simulations, and optimum structures for the wavelengths of 4.3 μm and 785 nm, and the effect of the gap variation on the absorption coefficients. The optimum unit cell for the 4.3 μm wavelength has a strip length L_s = 1.77 μm, a strip width W_s = 100 nm, a beam width W_b = 100 nm, periods in x and z direction $P_x = P_z$ = 3.1 μm, and an absorption coefficient of 42.4%. The optimum unit cell for 785 nm wavelength has L_s = 350 nm, W_s = 100 nm, W_b = 100 nm, $P_x = P_z$ = 660 nm, and an absorption coefficient of 33.8%. It is worth noting that the incident light is linearly polarized along the z-direction. For unpolarized light, the absorption coefficient should be reduced by half.

For demonstration purposes, the proof-of-concept device adopts the parameters of the antenna for 785 nm wavelength, because the radiation light is on the edge of the visible spectrum which facilitates beam alignment in experiments. The device is composed of 13

fishbone nanowires with a period of 660 nm. With the help of HF vapor etching, the wires are suspended 62 nm above the waveguide. Each wire is 12.54 μm long and consists of 16 nanoantennas with a period of 660 nm. The fabricated device has been optically characterized. Instead of using a 785 nm laser as the radiation source, the 660 nm laser is employed due to its high power and better modulation effect on the device. The wavelength response is found to be blue shifted, and the device can respond to the 660 nm wavelength and even white LED. Under 660 nm polarized light illumination, the device shows a responsivity of 3.954×10^{-3} $\mu m^2/\mu W$. The noise equivalent power, dominated by the waveguide coupling instability, is 3.01 $\mu W/\sqrt{Hz}$. The 3dB bandwidth of the device is 9.6 Hz corresponding to a time constant of 16.6 ms. To reduce the system noise, the TLF should extrude as little as possible. In addition, the experiment setup should be placed in a vacuum chamber to avoid the usage of a noisy air flow cabinet. This can also help reduce the thermal fluctuation noise at the device level.

Chapter 5

Silicon Nitride Trench Waveguide

5.1 Introduction

Trench waveguides are built on the channels, with their guiding regions below the substrate surface. Silicon can be used as the substrate material to provide V groove trenches that can be achieved by anisotropic etching [103]–[107]. Trench waveguides built on V grooves first emerged in the 1970s with bilayer configurations. The first layer deposited on the silicon substrate has a lower refractive index to serve as the cladding, and the second layer with a higher refractive index is deposited on top of the first layer and sometimes etched to confine the light. Different waveguiding materials have been studied such as epoxy [108], plastic [109], [110], glass [111], [112], and polymer [113], [114]. These earlier works were all passive devices, mainly aiming to lower the propagation loss, to improve the fiber to waveguide coupling coefficient, and to redirect light. Since the first demonstration of E7 nematic liquid crystal channel waveguide in SiO_2-Si V grooves [115], there has been a thrust in using liquid crystals as the guiding material in the V groove [116]–[120] or semicircular groove [121] trench waveguides as potential candidates for low-cost, highly functional photonic elements. The liquid crystals, whose optical properties rely on the applied voltage, are encapsulated by the grooves and the Indium Tin Oxide (ITO) layer, forming a microscale triangle channel waveguide for electro-optical modulation. Although widely employed as passive and active devices, all the previously demonstrated trench waveguides had large cross-sections, which were incompatible with nanophotonics.

For nanophotonics, it is preferable to find a fabrication method that is scalable and repeatable. Recently, the V groove trench waveguide has been reexamined in the field of nanophotonics due to its capability of controlling the sidewall angles and the self-stopping etching feature in triangle waveguides. The interest of using V groove trench waveguides lies in but not limited to the following reasons, (i) the surface roughness on the sidewall is smoothened by preferential etching process on silicon, (ii) high degree precision ensured by self-aligning obtained from anisotropic etching with low cost, (iii) large-area production of sub-micron features, and (iv) inborn advantage of combining photonics and microfluidics with the help of the V groove channels. These features render the V groove trench waveguides suitable for low loss, high confinement, and optofluidic applications.

In this chapter, the study of the Si_3N_4 trench waveguide starts from simulation modeling, followed by fabrication procedure. The optical properties of the trench waveguide, including the model distribution, the evanescent intensity ratio (*EIR*), the dispersion, the propagation loss, and the nonlinearity, will be explored. Gold nanoantennas can be integrated on the waveguide to enhance the waveguide nonlinearity or the evanescent fields, which can be used for nonlinear and optical trapping applications.

5.2 Si_3N_4 Trench Waveguide Modeling

The fundamental step to understand and design the Si_3N_4 trench waveguide is to solve the mode solutions. The cross-sections of the trench waveguides are irregular, with their core region varying from triangle to trapezoidal shapes. In the past, theoretical analysis based on the FEM method [122], the effective index method [123], the Rayleigh principle and least-squared method [124], and the weighted residual method [125] have been put forward to study the mode properties in trapezoidal waveguides. However, the conclusions

drawn from those analyses cannot be generalized for all the trench waveguides because the waveguiding layer is non-flat. Therefore, a customized study is necessary to examine their optical properties thoroughly.

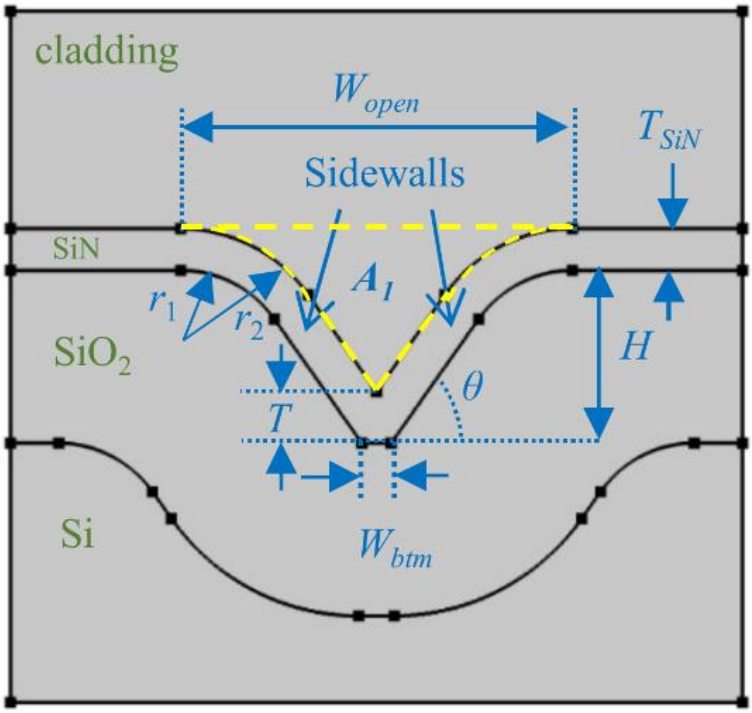

Figure 5-1. The silicon nitride trench waveguide cross section. The region surrounded by the yellow dashed line is the sensing region, and the area of this region is denoted as A_1. The total simulation area is denoted as A_{tot}.

The theoretical model, which is based on the fabrication results that will be elaborated in the next session, is shown in Figure 5-1. The sidewall angle θ of the waveguide is 54.7°, consistent with the silicon wet etching properties. Unlike my preliminary model that used Bezier curves [126], the connections between the silicon nitride sidewalls and the top flat slabs are smoothened with arcs of r_1 = 2 μm and r_2 = 2 μm + T_{SiN} to mimic the actual fabrication images, where T_{SiN} is the silicon nitride deposition thickness. The size of the trench waveguide is characterized by the waveguide bottom width W_{btm} and the actual

waveguide T. W_{btm} and T can be derived from the fabrication parameters, W_{open}, H, and T_{SiN}, where W_{open} is the opening window width and H is the etching depth. W_{btm} is governed by $W_{\mathrm{btm}} = W_{\mathrm{open}} - 2\cot(\theta) \cdot H$. If $W_{\mathrm{open}} < 2\cot(\theta) \cdot H$, W_{btm} will be 0, and a triangle trench will be carved out. Otherwise, the trenches will be trapezoidal. The actual waveguide thickness T is affected by the silicon nitride deposition process which grows faster in corners. T has the following relation with the silicon nitride deposition thickness T_{SiN} and the waveguide bottom width W_{btm}.

$$\begin{cases} T = T_{SiN}, & \text{if } W_{btm} \geq 2T_{SiN}\tan\left(\dfrac{\theta}{2}\right) \\ T = \dfrac{T_{SiN}}{\cos(\theta)} - \dfrac{W_{btm}}{2}\tan(\theta), & \text{if } W_{btm} < 2T_{SiN}\tan\left(\dfrac{\theta}{2}\right) \end{cases} \tag{5.2.1}$$

In the simulations, H and T_{SiN} are set to be 3 μm and 0.725 μm respectively based on the fabrication results that will be presented shortly. It is worth mentioning that the shape of the real devices may not follow Eq. (5.2.1) strictly due to imperfect fabrication, and thus causes inevitable mismatches between simulated and experimental results. The irregularity in the trench bottom region depends on the fabrication process and may vary from device to device. Therefore, it is difficult to abstract and to generalize the deformation into a simple geometric model. However, using straight lines in the trenches without considering the deformation greatly simplifies the structure without losing the representativeness, and the approach has also been used in other literature, e.g., Ref. [116]. Thus, the theoretical model is still accurate in characterizing the mode properties.

The simulations are carried out in a frequency domain finite element method (FEM) solver (COMSOL Multiphysics). The refractive index of the low-stress silicon nitride is a function of wavelength and is defined as $n^2(\lambda) = 1 + 3.585\lambda^2/(\lambda^2 - 0.1316^2)$ [62], where λ

is in the unit of micrometer. The refractive index of the SiO_2 is adopted from Ref. [127]. Perfectly matched layer boundary conditions are used to minimize the back scattering at boundaries. All the simulations are performed at 1550 nm wavelength unless specified otherwise.

5.3 Si_3N_4 Trench Waveguide Fabrication

Fabrication of the V groove trench waveguides does not require E-beam lithography but merely relies on optical lithography followed by the anisotropic potassium hydroxide etching. Using this method, even sub-micron waveguide dimension can be achieved with a MEMS-grade photomask. The anisotropic potassium hydroxide (KOH) etching on a <100> silicon wafer carves a trapezoidal or triangular trench with an angle of 54.7° with respect to the substrate surface. Etching time and aqueous alkaline concentration are the key parameters to control the etching depth. The total etch time of 10 min allows us to achieve waveguide dimensions with 100 nm precision in a standard clean room environment. If further precision is required, a highly doped boron-silicon layer [128] should be inserted or *p*-*n* junction layer [129] should be added as an etching stopper to achieve desired precision. The shape of the waveguide is determined by the etching depth H, the opening window width W_{open} and the silicon nitride deposition thickness T_{SiN}. Low-pressure-chemical-vapor-deposition (LPCVD) was used to deposit a T_{SiN} = 725 nm layer of silicon nitride in two cycles to avoid cracking. Detailed fabrication procedure can be found in Ref. [62]. Here, we show two waveguides with their bottom regions being in triangle or trapezoidal shapes. The two trench waveguides have the same etching depth of 3 μm, but their W_{open}s are 4 μm, and 5 μm in Figure 5-2(a) and (b), respectively.

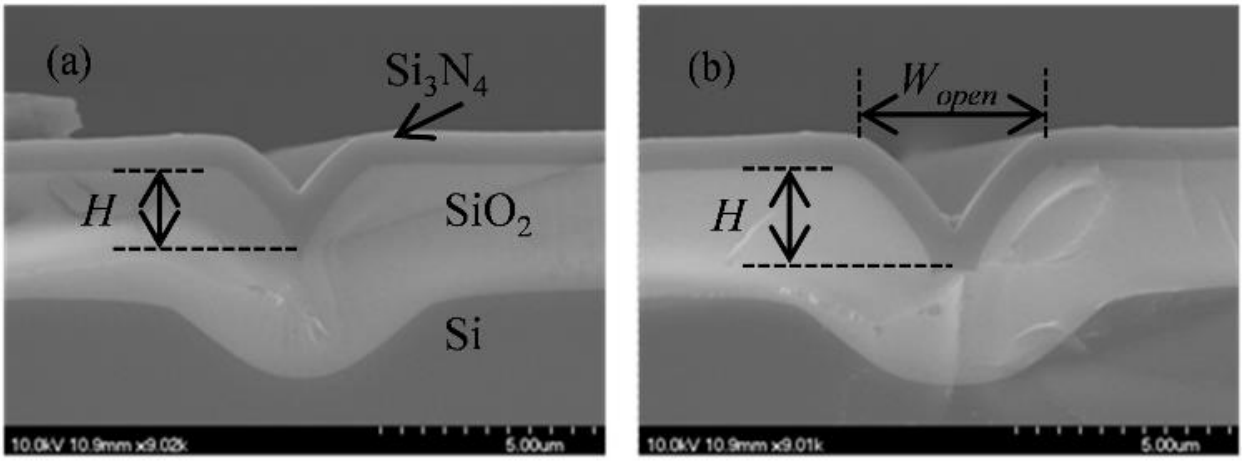

Figure 5-2. SEM images for fabricated silicon nitride trench waveguides with thickness T_{SiN} = 725 nm, etching depth H = 3 μm, and top opening window (a) W_{open} = 4 μm, and (b) W_{open} = 5 μm.

5.4 Si_3N_4 Trench Waveguide Characterization

5.4.1 Trench Waveguide Mode Properties

The trench waveguide has its modes guided in the core region. Due to the inclined sidewalls, it does not support pure TE or TM modes that are commonly found in rectangular waveguides. Instead, its modes are hybrid and have both x and y components. The fundamental mode of a triangle trench waveguide (W_{btm} = 0) is a quasi-TM mode with a TM fraction of 82.0%. The TM fraction is defined as

$$\frac{\iint |E_y|^2 \, dxdy}{\iint \left(|E_x|^2 + |E_y|^2 \right) dxdy} \tag{5.4.1}$$

The TE fraction can be defined in a similar way by changing the E_y with E_x in the numerator. Figure 5-3 shows the quasi-TM and quasi-TE modes of a triangle trench waveguide (W_{btm} = 0). The quasi-TE mode has a TE fraction of 73.4%.

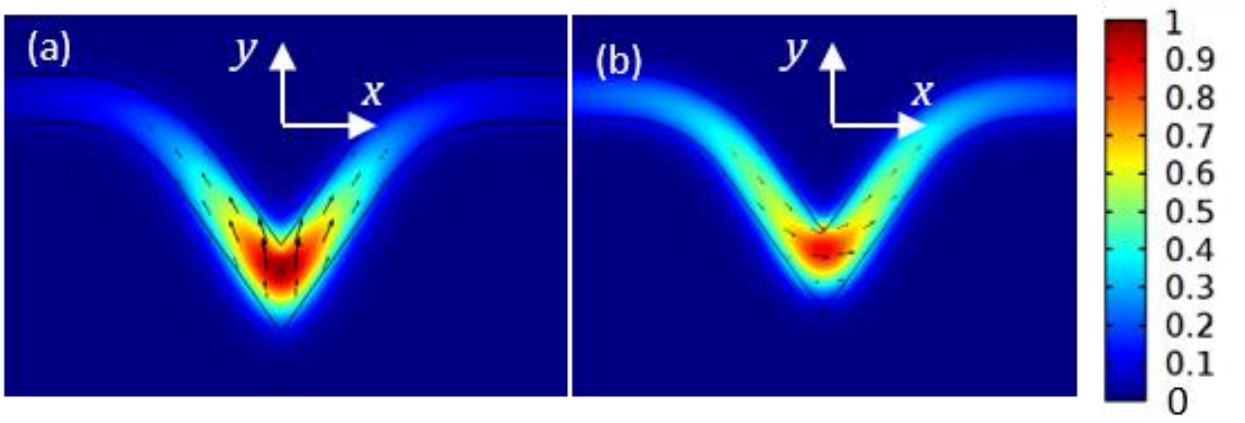

Figure 5-3. (a) Normalized quasi-TM mode and (b) normalized quasi-TE mode profile in a triangle trench waveguide. The black arrows represent the electric fields.

As can be seen from the mode profiles, the trench waveguide is analogous to a rib waveguide in the way that the trench bottom region provides a higher effective refractive index than the sidewalls and the top slabs. In other words, the guiding mechanism in the waveguide relies on the effective refractive index difference between the trench bottom region and the adjacent slabs. Due to the silicon nitride deposition property, the trench bottom region is thicker than the slab regions when the trench waveguide is narrow, and thereby the bottom region has a higher local effective refractive index. Especially, the triangle trench waveguide has the largest thickness to be $T_{SiN}/\cos(\theta)$. Based on Eq. (5.2.1), as W_{btm} increases, T decreases, and finally becomes equal to T_{SiN}, resulting in a reduction in the effective refractive index difference and causing the modes to leak into the slab regions. The change of the W_{btm} will affect the mode properties. Figure 5-4 (a) and (b) shows the effective refractive indices (n_{eff}) and effective mode areas (A_{eff}) of the quasi-TM and quasi-TE modes as a function of W_{btm}. As the W_{btm} increases from 0 to 0.7 μm, the A_{eff} expands from 2.8 μm^2 to 6.7 μm^2 for the quasi-TM mode, and from 4.1 μm^2 to 8.9 μm^2 for the quasi-

TE mode. n_{eff} for the quasi-TM mode drops more quickly than the quasi-TE mode because guiding the quasi-TM mode relies more on the layer thickness in the trench bottom. The n_{eff} drops while the A_{eff} increases as the W_{btm} increases, indicating that the mode guidance is weakened when the waveguide becomes wide. Figure 5-4 (c) and (d) particularly compare the normalized quasi-TM electric field profiles of a triangle trench waveguide with W_{btm} = 0, and a trapezoidal trench waveguide with W_{btm} = 0.7 μm. In terms of better confinement and low loss propagation applications, one should target at the triangle trench waveguides.

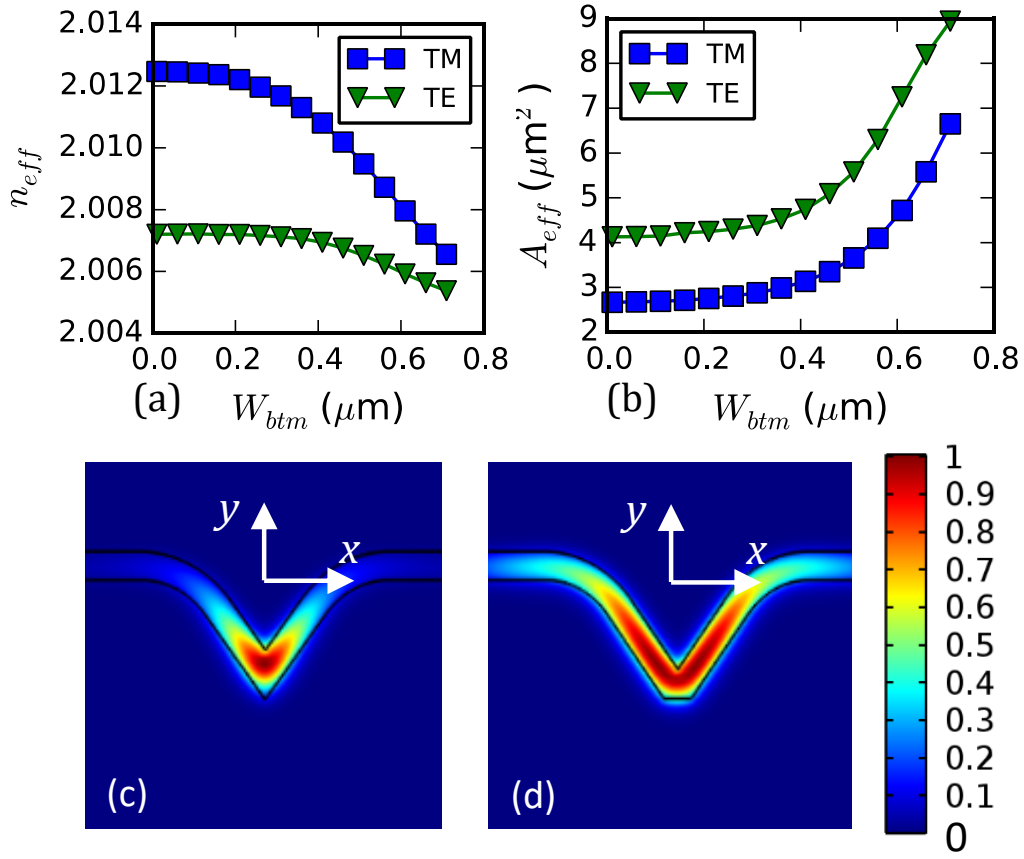

Figure 5-4. (a) n_{eff} and (b) A_{eff} of the quasi-TM and quasi-TE modes as a function of W_{btm}. The normalized quasi-TM electric field profiles of a triangle trench waveguide with (c) W_{btm} = 0 and with (d) W_{btm} = 0.7 μm.

5.4.2 Trench Waveguide Evanescent Intensity Ratio

The trench waveguide has an inborn advantage for sensing because the trench valley can work as a container for liquids. Therefore, no cap layer was deposited on top of the silicon nitride guiding layer, so that the evanescent fields from the core region directly interact with the analyte in the sensing region (enclosed by the yellow dashed line in Figure 5-1). The more evanescent field extending into the sensing region, the more light-matter interactions there will be. To quantify the evanescent field strength, we define the evanescent intensity ratio *EIR* as

$$EIR = \frac{\iint_{A_1} \left|E\left(x,y\right)\right|^2 dxdy}{\iint_{A_{tot}} \left|E\left(x,y\right)\right|^2 dxdy} \tag{5.4.2}$$

where A_1 is the area of the trench channel and A_{tot} is the total simulation area that includes A_1. *EIR* highly depends on the waveguide geometry, e.g., on the width of the waveguide bottom, W_{btm}, the deposition thickness of the silicon nitride, T_{SiN}, the polarization state of the light, and the refractive index of the upper cladding layer. For instance, the *EIR* dependency on W_{btm} is presented in Figure 5-5. Here, the impact of the mode polarization and waveguide geometry on *EIR* is studied for a trench waveguide with T_{SiN} = 725 nm and H = 3 μm. As the W_{btm} increases from 0 to 0.7 μm, the *EIR* for the quasi-TE mode decreases from 2.26% to 1.81% in an air-cladding waveguide, and from 3.04% to 2.57% in a water-cladding waveguide. On the contrary, the *EIR* for the quasi-TM mode increases, and reaches peak values of 3.17% in the water-cladding waveguide when W_{btm} = 0.56 μm and 2.35% in the air-cladding waveguide when W_{btm} = 0.51 μm. The variation in *EIR* with respect to the cladding material is expected. Water cladding gives larger *EIR* than

air cladding due to a lower index contrast. Thus, for sensing applications, W_{btm} = 0.56 μm is an optimum value for the water-cladding trench waveguide with T_{SiN} = 725 nm.

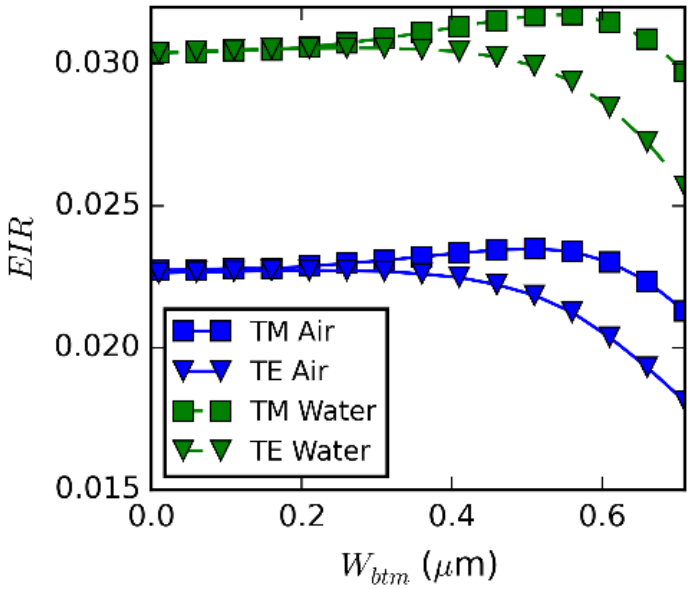

Figure 5-5. The *EIR* as a function of W_{btm} for a trench waveguide with T_{SiN} = 725 nm and H = 3 μm. The blue curves are for the waveguide with air cladding, while the green curves are for the waveguides with water cladding.

5.4.3 Trench Waveguide Propagation Loss

Simulations show that the TM mode is better guided than the TE mode because it has higher effective mode index and smaller mode area, which indicates that the TM mode will have lower propagation loss. To verify the simulation results, we measure the propagation loss of the trench waveguides for both TE and TM modes. The waveguides are diced into three segments with different lengths. The waveguide ends have been polished by lapping films for optical quality facets (<0.1 μm grain size). We then characterize the waveguide loss using the cut-back method. As shown in Figure 5-6(b), we measure the total loss of the

5 μm wide waveguides with three different lengths: L=0.5 cm, 1 cm, and 1.5 cm respectively. From the slope, The waveguide propagation loss is derived to be 0.8±0.26 dB/cm for TM mode. As expected, the fabricated waveguides are polarization sensitive and the TE mode has higher propagation loss of 3.13±0.37 dB/cm. Compared with other works summarized in Table 5-1, our waveguide propagation loss is moderate and within the normal region. Unlike high aspect ratio waveguides in which most of the mode energy propagates in the cladding region [15], the mode of the waveguides reported here is tightly confined in the waveguide core region, and hence, makes modes more susceptible to losses induced by surface roughness [130] at the top layer. To reduce the propagation loss, an oxide cap layer can be deposited to passivate the waveguide surface. However, oxide cap layer has not been deposited intentionally, because these waveguides will be used for sensory applications. The second reason for reported losses arises from the mode leakage to slab region. This can be minimized by increasing the etch depth of trenches. Moreover, the waveguide loss can be further reduced by using stoichiometric nitride which is known to be more transparent than silicon rich nitride [15] and optimizing the post-annealing temperature and time to reduce the Si-H and N-H absorption [131]. A tapered lens fiber is used for butt-coupling, and the estimated insertion loss is ~ 8 dB without any optimization.

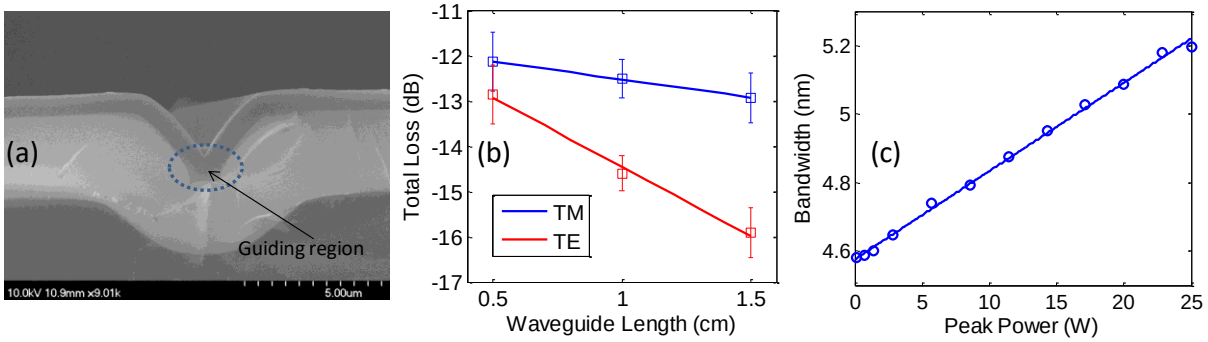

Figure 5-6. (a) SEM of the fabricated waveguide with W_{open} = 5 μm. (b) Total loss of the waveguide with different length using cut-back method. (c) SPM broadening at different input peak power levels. A nonlinear refractive index of n_2=1.39×10^{-19}m^2/W was derived from the curve.

Table 5-1. Comparison between our work and previous publications.

Waveguide dimension (silicon nitride region)	Propagation loss	Wavelength	Year
w≈ 0.8 μm, h = 0.9 μm	0.8 ± 0.26 dB/cm	1550 nm	Our work
w = 4 μm, h = 0.12 μm	0.3 dB/cm	1.3-1.6 μm	1987 [8]
w = 12.8 μm, h = 200 nm	4.8 ± 0.5dB/cm	1544 nm	2004 [132]
w >10 μm, h = 500 nm multilayer	1.5 ± 0.2 dB/cm	1550 nm	2005 [13]
w = h ≈ 1.1 μm	0.06~0.08 dB/cm	1460-1530 nm	2007 [133]
w = 1 μm, h = 0.5 μm	~4 dB/cm	1550 nm	2008 [26]
w = 1.45 μm, h = 725 nm, 23° wall angle	0.5 dB/cm	1550 nm	2010 [134]
w = 2.8 μm, h = 80 nm, 2 mm bending radius	0.03 dB/cm	1550 nm	2011 [15]

5.4.4 Trench Waveguide Nonlinearity

Silicon nitride can be used in high power applications because of the absence of two-photon absorption and free carrier absorption[134]. Waveguides made of silicon nitride can be designed to have high effective nonlinear parameter γ [135], which is defined as $\gamma = (2\pi n_2)/(\lambda A_{eff})$[136]. Here, the nonlinear refractive index n_2 is fixed by the uniform guiding layer of silicon nitride, but A_{eff} can be varied by adjusting waveguide geometry and wavelength to facilitate large effective nonlinearity γ.

To possibly facilitate nonlinear applications in these waveguides, we also want to characterize the nonlinear property of the waveguides. Particularly we pursued the

nonlinear refractive index, n_2, of the silicon nitride, which is related to the third order susceptibility of Si_3N_4. Here, the nonlinear refractive index is measured by utilizing the spectral broadening caused by self-phase-modulation (SPM) of high energy pulses in the nonlinear medium [137], [138]. According to [137], [139], under the Gaussian beam excitation assumption, the spectral broadening caused by SPM can be theoretically expressed as

$$\Delta\lambda = \Delta\lambda_i + 4\sqrt{\frac{2\ln 2}{e}} \cdot \frac{\lambda_0 n_2 L_{eff}}{cA_{eff}} \frac{P}{t_p} \tag{5.4.3}$$

Here, $\Delta\lambda_i$ is the bandwidth of the input laser pulse, λ_0 is the center wavelength, n_2 is the nonlinear refractive index, L_{eff} is the effective length defined by $L_{eff} = \left(1-\exp(-\alpha L)\right)/\alpha$ with α being waveguide loss coefficient and L being waveguide length, A_{eff} is the effective mode area, P is the peak pulse power and t_p is the full-width-at-half-maximum (FWHM) pulse width, and it is 550 fs in our case. According to Eq. (5.4.3), the spectral broadening caused by SPM is linearly related to the pulse peak power and the slope coefficient is also linearly related to the nonlinear refractive index n_2. If we can determine the spectral broadening for different input power levels, we can derive the nonlinear refractive index from the slope coefficient of the curve. To accomplish this, high power optical pulses are coupled into the 1.5 cm long Si_3N_4 waveguides and the 3dB bandwidth of the output pulses is measured. Figure 5-6(c) shows the 3dB bandwidth of the femtosecond laser pulse at waveguide output with different input peak power. With the propagation loss of 0.8 dB/cm from loss measurement and an effective mode area of A_{eff} = 1.9 μm^2, the nonlinear refractive index value n_2 is estimated to be 1.39×10^{-19} m^2/W from the slope of the fitted linear curve. This

value agrees well with the values reported in other literature [138], [140]. This corresponds to a nonlinear parameter of $\gamma = (\omega n_2)/(cA_{eff}) = 0.3W^{-1}/m$ for the waveguide, which is >100 times larger than that in single-mode fibers. It is worth noting that the effective mode area A_{eff} varies for difference waveguides because of the irregular shapes.

The measured nonlinear index n_2 of our low-stress silicon nitride waveguides is compared with other experimental results at telecommunication wavelengths from different waveguide dimensions in Table 5-2. In addition, the n_2 of SiO_2 and Si are also added as reference values. Our measured value falls among the others as shown in Table 5-2, which is anticipated by taking the waveguide geometry and material properties into considerations. On one hand, low confinement waveguides have more power extending in the SiO_2 cladding region, leading to a lower effective n_2, on the other hand, increasing the silicon content results in an increase in material nonlinearity.

Table 5-2. Comparison of nonlinear Kerr coefficient n_2 for silicon nitride waveguides with different fabrication methods and waveguide geometries.

Composition	n_2(m^2/W)	geometry
SiO_2 [141]	2.16×10^{-20}	optical fibers
Si_3N_4 (LPCVD) [142]	9×10^{-20}	2.8 μm × 80 nm
Si_xN_y (LPCVD) [62]	1.39×10^{-19}	trench waveguide
Si_3N_4 (PECVD) [143]	2.4×10^{-19}	1 μm × 500 nm
Si_xN_y (LPCVD) [144]	1.4×10^{-18}	1.65 μm × 700 nm
Si [145]	4×10^{-18}	bulk crystalline Si

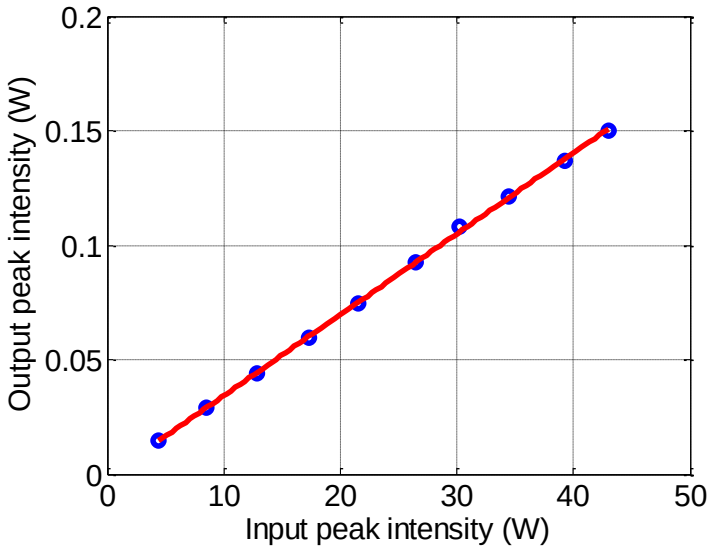

Figure 5-7. The measured output peak power vs. input peak power for a silicon nitride trench waveguide with W_{open} = 7 μm. The blue circles are measured data while the red curve is a fitting for the experimental data. The input and output losses have been counted and compensated in the measurement.

To guarantee there is no nonlinear loss of the waveguides, we monitor the power after the attenuator as the input power and the power after collimator as output power. A linear relation between the input and the output peak power is obtained from a waveguide with W_{open} = 7 μm, implying the absence of the nonlinear loss. The experiment confirms that two-photon absorption (TPA) does not occur in silicon nitride around 1.55 μm because photo energies at this wavelength are less than $E_{g(SiN)}/2$, where the energy bandgap of silicon nitride $E_{g(SiN)}$ is 5.3 eV [146]. To trigger the TPA in silicon nitride, wavelengths must be smaller than 470 nm. This demonstrated linear relation between the output power and the input power indicates the silicon nitride waveguide is a good candidate for high power nonlinear applications.

To pursue a better nonlinear performance, we theoretically optimized the nonlinear parameter γ. Nonlinear effects can occur over a broad spectrum range. Both A_{eff} and n_2 are

functions of λ and so is γ. The dispersion of n_2 over wavelength can be estimated accurately based on the linear refractive indices by using Miller's rule [147],

$$n_2(SI) = k\frac{40\pi^2}{cn^2(\lambda)}\chi^{(3)}(esu) \tag{5.4.4}$$

$$\chi^{(3)}(esu) = \left[\chi^{(1)}(esu)\right]^4 \times 10^{-10} \tag{5.4.5}$$

$$n^2(\lambda) = 1 + 4\pi\chi^{(1)}(esu) \tag{5.4.6}$$

where c is the speed of light, $n(\lambda)$ is the wavelength-dependent refractive index in SI units and is given in Section 5.4.1. $\chi^{(1)}$ is the first order susceptibility, $\chi^{(3)}$ is the third order susceptibility, both $\chi^{(1)}$ and $\chi^{(3)}$ are in electrostatic units, k is a parameter to fit the experimental results and is estimated to be 0.7143 in our calculations.

As illustrated in Figure 5-4(b), for a trench waveguide with a fixed thickness, it has the smallest A_{eff} when W_{btm} = 0, which is in favor of nonlinear applications. Therefore, we give priority to consider the triangle trench waveguides for nonlinear applications. Given the n_2 for SiO_2 from literature and the calculated n_2 for silicon nitride in the wavelength range from 1.35 μm to 1.65 μm, the nonlinear parameter γ has been simulated for the trench waveguides with different deposition thicknesses over the spectrum range, as presented in Figure 5-8, which shows the results for the quasi-TM mode in triangle trench waveguides with air cladding. The trench waveguides have higher γ at shorter wavelengths. Waveguides with T_{SiN} between 400 nm and 700 nm have larger γ due to tight mode confinement. The largest γ is 0.327 $W^{-1}m^{-1}$ when T_{SiN} = 540 nm at a wavelength of 1350 nm. At 1550 nm wavelength, the γ is maximized to be 0.219 $W^{-1}m^{-1}$ when T_{SiN} = 600 nm.

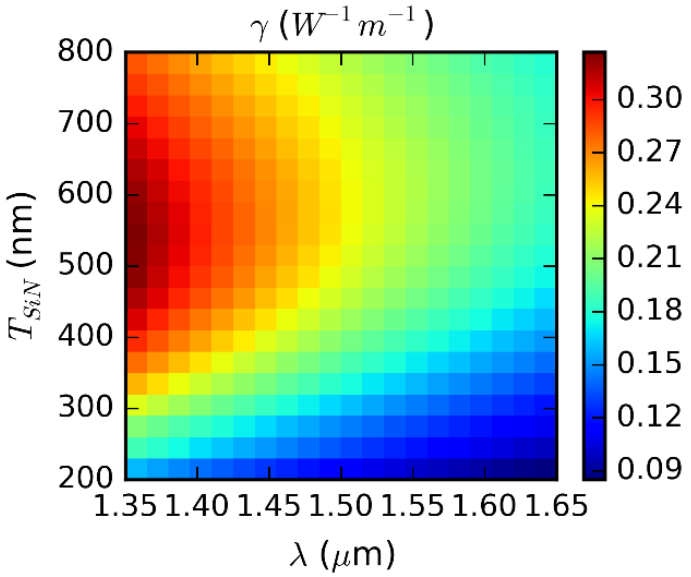

Figure 5-8. Simulation of the nonlinear parameter γ as a function of the silicon nitride deposition thickness T_{SiN} and the wavelength λ for the fundamental quasi-TM modes in the trench waveguides with W_{btm} = 0 and air cladding.

5.4.5 Trench Waveguide Dispersion

In nonlinear applications, the phase mismatch will limit the efficiency of the nonlinear process. To obtain phase-matching for broadband wavelength conversion, the waveguide dispersion D should be engineered by tailoring the waveguide dimensions, so that the pump wavelength is in the anomalous region and is close to the zero dispersion wavelength. To study the dispersion of the waveguides we simulate the effective refractive index n_{eff} for various wavelengths, which takes both the material dispersion and the waveguide dispersion into considerations. Our simulation results presented in Figure 5-9 show that the dispersion D can be tuned from -800 ps·nm^{-1}·km^{-1} to 20 ps·nm^{-1}·km^{-1} by changing the T_{SiN} from 280 nm to 800 nm. Thick silicon nitride trench waveguides (T_{SiN} > 670 nm) can

have their dispersion in the anomalous region and close to zero, which is in agreement with experimental work in Ref. [148]. However, growing thick silicon nitride films will be subject to film cracking risk due to tensile stress [149], and hence multiple deposition and annealing steps may be required. The waveguide with T_{SiN} = 687 nm has zero dispersion at 1550 nm with a zero-dispersion slope of 8×10^{-2} ps·nm^{-2}·km^{-1}. Close scrutiny of the simulation results predicts that FWM may be efficient in the triangle trench waveguide with T_{SiN} = 680 nm. For this geometry, the group velocity dispersion at the pump wavelength at E-band (near 1450 nm) is close to 2.15 ps·nm^{-1}·km^{-1} with a dispersion slope of -1.725×10^{-2} ps·nm^{-2}·km^{-1}. If choosing the pump wavelength λ_2 to be 1.44 μm, the pump wavelength will be in the anomalous region and stay close to zero. For the degenerate FWM with Stokes and anti-Stokes wavelengths at λ_3 = 1.53 μm and λ_1 = 1.36 μm, respectively, the phase mismatch will be $\Delta k = \beta_1 + \beta_3 - 2\beta_2$ = 11.09 m^{-1}. Correspondingly, the maximum parametric gain is $g_{max} = \gamma P_0 = \Delta k/2$ = 5.545 m^{-1} with undepleted pump approximation [150], where P_0 is the peak pump power at the input of the waveguide. Given the nonlinear parameter γ = 0.2597 W^{-1}m^{-1} at the pump wavelength, P_0 should be around 21.4 W, which is easily attainable by using mode-locked lasers. The peak power level is safe for silicon nitride waveguides. Similar or even larger peak powers have already been used in silicon nitride waveguides [151]. Such wavelength converters are particularly useful for frequency band conversion between the C-band and the E-band. Besides broadband FWM, the same waveguide can also be used for narrowband FWM within the C-band, where λ_1 = 1.54 μm, λ_2 = 1.55 μm, and λ_3 = 1.5613 μm. This configuration yields a maximum parametric gain of 0.13 m^{-1} with γ = 0.215 W^{-1}m^{-1} and P_0 = 604 mW at 1550 nm pump wavelength. In this calculation, we assume there is no loss. However, in the presence of loss, the parametric

gain will be reduced due to a reduction of the pump power. The influence of the loss can be reflected from the effective length of the waveguide that is expressed as L_{eff} = (1 - exp(-αL))/α, where L is the waveguide length, and α is the propagation loss (m^{-1}). For example, the propagation loss for the TM mode in the triangle trench waveguides with T_{SiN} = 725 nm is measured to be 1.66 dB/cm [150]. Correspondingly, the effective length of a 2 cm long waveguide is only 1.4 cm.

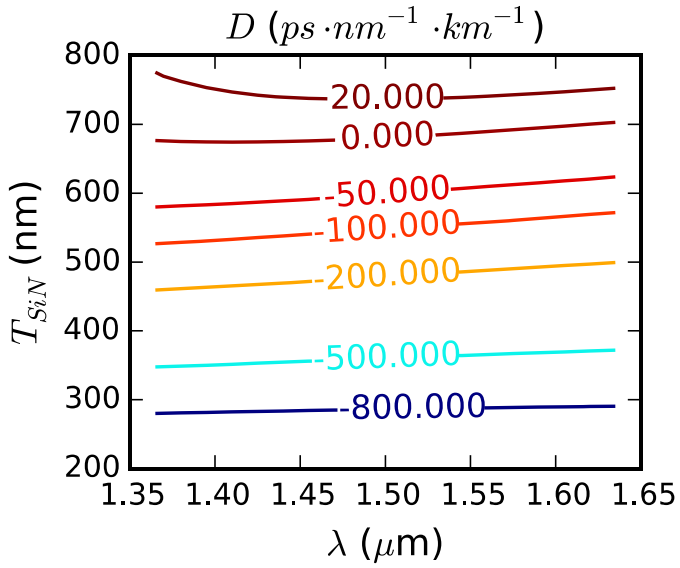

Figure 5-9. Simulation of dispersion D as a function of silicon nitride deposition thickness T_{SiN} and wavelength for the fundamental quasi-TM mode in trench waveguides with W_{btm} = 0 and air cladding.

In addition to changing the waveguide thickness, varying the trench waveguide width is an attractive approach to manipulating the waveguide dispersion, because it is more practical in actual fabrication. Quasi-phase-matching can be achieved by alternating waveguide width to compensate the phase mismatch [152], [153]. The concept can also be applied in the trench waveguides. Figure 5-10 presents the dispersion D as a function of the W_{btm} for the trench waveguide with T_{SiN} = 700 nm and H = 3 μm at 1550 nm. The

waveguide has zero dispersion when W_{btm} = 0.34 μm. Below that value, the waveguide is in anomalous dispersion region, and above that, the waveguide is in normal dispersion region.

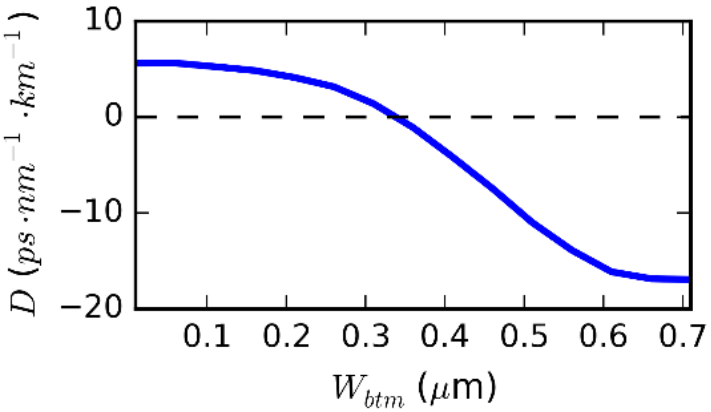

Figure 5-10. The group velocity dispersion D as a function of the W_{btm} for the trench waveguide with T_{SiN} = 700 nm and H = 3 μm.

5.5 Applications of the Si_3N_4 Trench Waveguides

5.5.1 Nonlinear Enhancement by Coating Gold-Nanoparticles

As presented in Session 5.4.4, the nonlinear properties of the trench waveguides indicate they are suitable for nonlinear applications due to the relatively high nonlinear refractive index n_2. To further increase the nonlinear response of the waveguides, plasmonic effects can be used. Such effects arise from coherent oscillations of conduction electrons near the surface of noble metal structures. Carefully designed structures provide field enhancement near the metal-dielectric interface. Among the vastly investigated metal structures, nanoparticles and nanoclusters are widely used in medical diagnostics [154], solar cells [155], [156], surface-enhanced Raman scattering sensors [157], [158] and etc.

Fabrications of self-organized clusters of metal particles are developing towards low-cost and highly reproducible ways [159]. For metal nanoparticles, the enhancement associated with the excitation of the localized surface plasmons (LSPs). Localized surface plasmons result from plasma oscillation in confined geometries like nanoparticles, or subwavelength features on a metal surface, e.g., bowtie antennas. The LSP resonance depends on the particle size, shape, spacing and surrounding medium. Since it is confined to a small volume, thereby tremendous enhancement can be achieved near the nanoparticle. The resulting strong fields enhance the nonlinear response locally, which is equivalent to increasing the nonlinearity of a material adjacent to a metal [160]. Experimental studies have shown that noble nanoparticles enhance the optical nonlinearity in nanocomposite films [161], [162] and nanobelts [163].

Planar assemblies of nanoparticle clusters allow scientists and engineers to harness electromagnetic field enhancements for nonlinear applications. Gold nanoparticle clusters are assembled onto the trench waveguides to enhance their nonlinearity. By using a chemical template, the metal nanoparticles are confined into tightly spaced clusters in a cheap but robust way, with high throughput [159]. As illustrated in Figure 5-11, a poly (styrene-b-methyl methacrylate) (PS-b-PMMA) (Mn=170-b-144 kg mol^{-1}) diblock copolymer is spun coated onto the trench waveguides, followed by annealing to generate a PS-b-PMMA template with lamellar PMMA domains. The PMMA domains are then functionalized with an amine end group, by immersing the substrate in an ethylenediamine/dimethyl sulfoxide (ED/DMSO) solution for 2 hours. 20 nm Au nanoparticles are functionalized with thioctic acid ligands, and a 1-ethyl-3-[3-(dimethylamino)propyl]-carbodiimide hydrochloride/ N-hydroxysulfosuccinimide (EDC/S-

NHS) crosslinker is used to facilitate a reaction between the amine group of the PMMA and the carboxylic group on the thiotic acid. Due to the size of the functionalized PMMA domain, which is about 40 nm in width, only a few nanoparticles can be attached to any one domain, resulting in cluster spacings below 7 nm. For the gold nanoparticle attachment, the functionalized PS-b-PMMA template is immersed in a solution of the functionalized nanoparticles. Two methods can be used. In the first, particles diffuse toward the surface in a gold nanoparticle solution with crosslinkers, at 40 °C. An alternative method uses electrophoresis to drive the nanoparticles toward the target. In the diffusion case, cluster spacings between 2 and 7 nm are generated, whereas in the electrophoretic case, spacings smaller than 1 nm have been found. In our case, diffusion was used since the silicon nitride is a dielectric material.

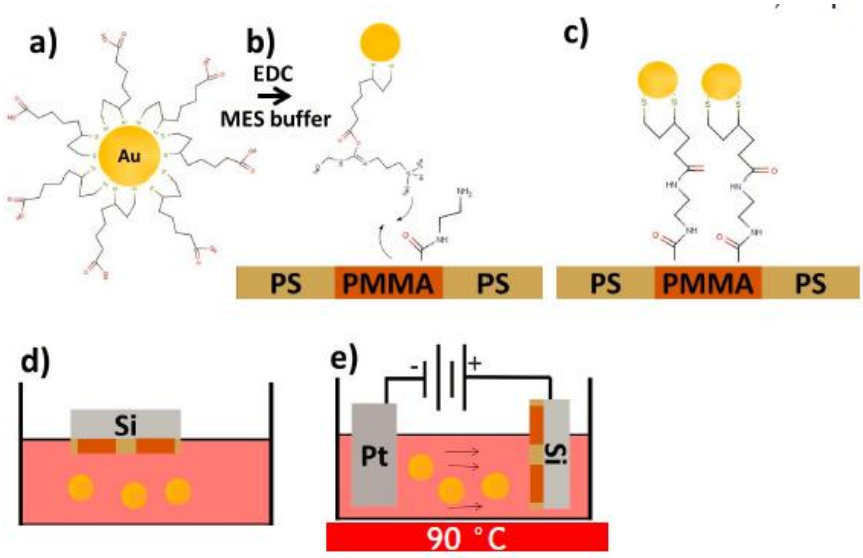

Figure 5-11. Gold nanoparticle deposition procedure.

Figure 5-12 shows the silicon trench waveguide coated with gold nanoparticle clusters. The nanoparticles are closely packed in the form of dimers, trimers, quadrumers or even hexagonally clusters. The localized surface plasmon strongly relies on the geometries and

spacing between the nanoparticles. It can be generalized that discrete clusters (dimers, trimers, and quadrumers) have better field enhancement than hexagonal close-packed (HCP) structures. For discrete clusters, higher cluster numbers and closer spacing are desirable. Detailed simulation results are also available in [159]. Since the nanoparticles are randomly distributed on the waveguides, plasmon-enhanced nonlinearity may vary at different locations. Therefore, only the average effect of the plasmon enhancement can be detected on a macro scale.

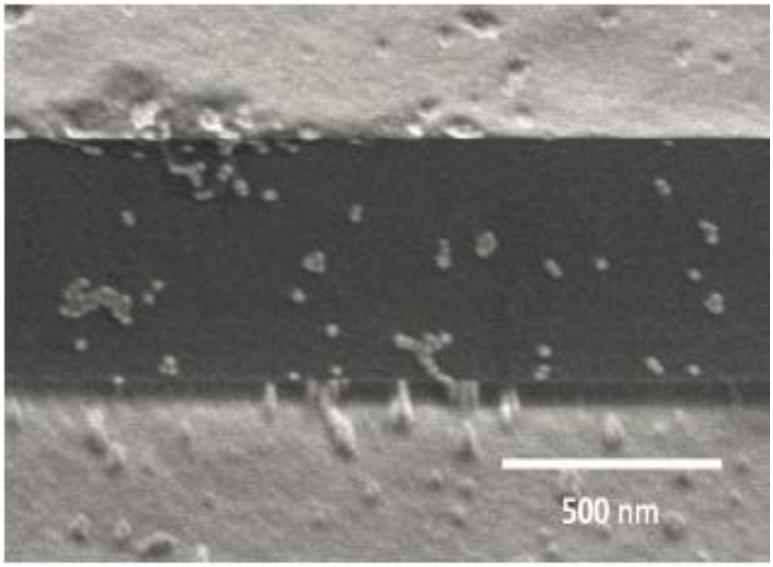

Figure 5-12. SEM images of Au nanoparticles deposited on one silicon nitride trench waveguide.

The nonlinearity of the gold nanoparticle coated Si_3N_4 waveguide is measured by the self-phase modulation as elaborated in Session 5.4.4. We use a femtosecond pulsed laser (Calmar Laser), τ_p = 550 fs, to provide a high-intensity source. An attenuator is connected to the pulsed laser to adjust the power. A 50:50 power splitter is used to split the power into the waveguide and an optical power meter (Newport 1830-C) is used to monitor the input power. The light is coupled from fiber to waveguide using a taper-lensed fiber (OZ Optics Ltd). The estimated coupling loss is ~ 7dB at the input facet. An objective lens

(Newport 20X) is placed close to the waveguide to collect power from the waveguide and to collimate the beam to be collected by the collimator. An optical spectrum analyzer (ANDO AQ6317B) followed the collimator to analyze the spectrum of the light from the waveguide. The whole experimental setup is illustrated in Figure 5-13. The results of two waveguide with W_{open} = 5 μm and W_{open} = 7 μm are shown in Figure 5-14.

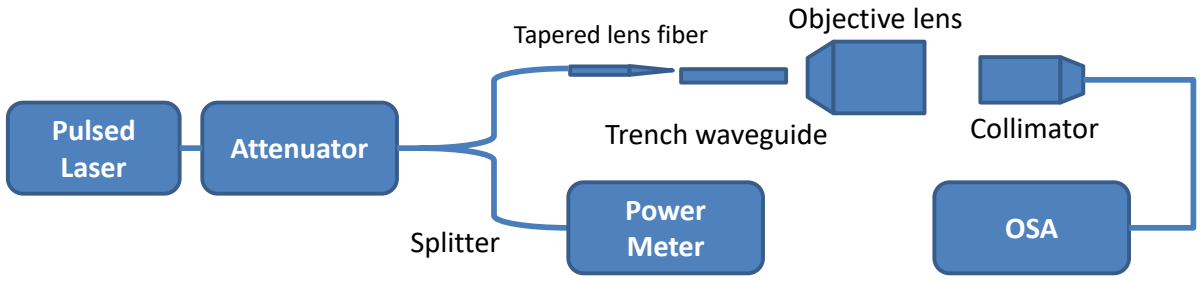

Figure 5-13. Experiment setup for characterizing nonlinear refractive index of silicon nitride waveguide.

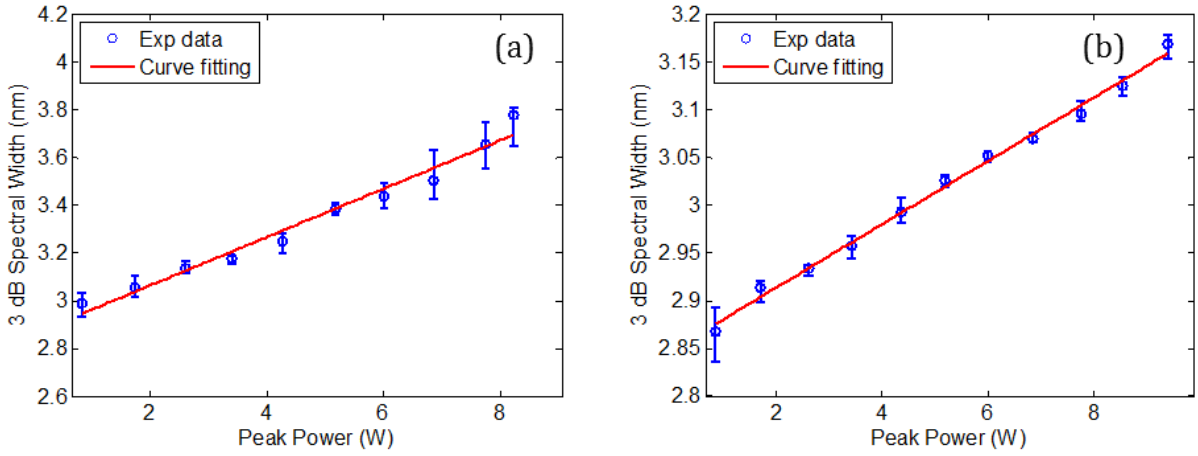

Figure 5-14. Spectral broadening as a function of input peak power in the waveguide (a) W_{open} = 5 μm, and (b) W_{open} = 7 μm. The blue error bars are experiment data, and each point was measured 10 times. The red line is a linear fitting of the data.

The input peak power is calculated by measuring the average power. By assuming Gaussian pulses, the peak intensity can be derived as follows.

$$P_0 = 2\sqrt{\frac{\ln 2}{\pi}}\frac{P_{avg}}{\tau_p R} \tag{5.5.1}$$

where P_{avg} is the averaged input power, R is the pulse repetition rate. Based on our previous experimental and numerical characterization [62], [164], we assume the propagation loss and effective mode area to be 0.8 dB/cm (TM mode) and A_{eff} = 1.9 μm^2 respectively in waveguides with W_{open} = 5 μm. Taken the 7 dB coupling loss into consideration, n_2 is calculated as 7.0719×10^{-19} m^2/W. The group velocity dispersion (GVD) β_2 at λ = 1550 nm was numerically analyzed to be 701 fs^2/cm. This value results in a dispersion length $L_D = \tau_p^2/\beta^2$ = 431.5 cm, which is much larger than the sample length (L = 1.12 cm) indicating negligible impact of dispersion at λ = 1550 nm. For waveguide with W_{open} = 7 μm, its structure aspect ratio favors TE mode instead of TM mode. Our previous experiments demonstrated that TE mode propagation loss in W_{open} = 5 μm and W_{open} = 6 μm waveguides were 3.13 dB/cm and 2.95 dB/cm, respectively. The propagation loss in the waveguide of W_{open} = 7 μm is calculated using linear extrapolation and estimated to be 2.77 dB/cm. Numerical studies show its effective mode area A_{eff} = 2.2 μm^2. Based on these derived parameters, n_2 of the 7 μm waveguide is approximately 3.3976×10^{-19} m^2/W.

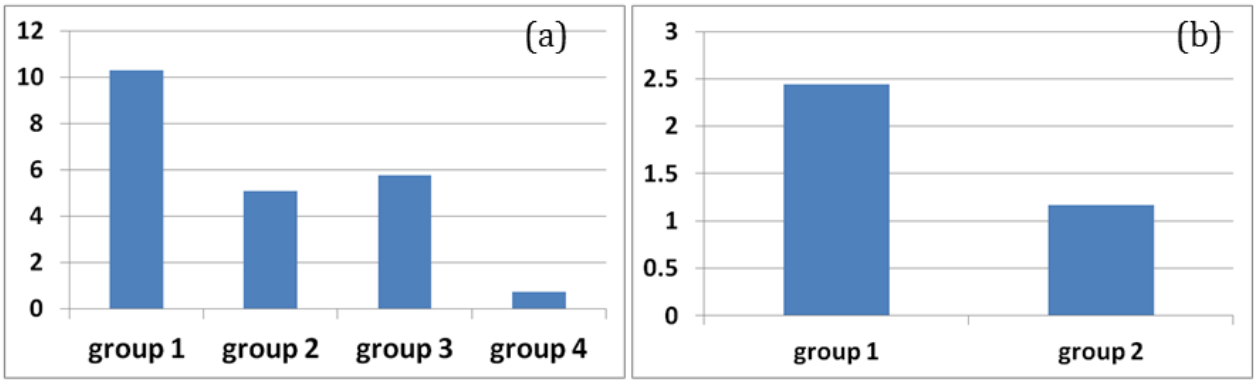

Figure 5-15. (a) Enhancement of third-order nonlinearity in waveguides with W_{open} = 5 μm. (b) Enhancement of third-order nonlinearity in the waveguides with W_{open} = 7 μm.

Compared to previously reported nonlinear refractive index $n_2 = 1.39\times10^{-19}$ m^2/W, the measured gold nanoparticles deposited waveguides have an enhancement of 5.09 for W_{open} = 5 μm waveguide and 2.44 for W_{open} = 7 μm waveguide. The enhancement caused by nanoparticle deposition is impressive. However, considering the random distribution of the nanoparticles on the wafer, the enhancement may vary at different locations. Therefore, a set of waveguides with same structures but at different locations on the wafer are measured and compared. We measure 4 waveguides whose top width W_{open} = 5 μm and two waveguides whose top width W_{open} = 7 μm. The samples include waveguides both at the center of the wafer and at the edge, thus are representative for statistics. The measured results are normalized and compared in Figure 5-15. It can be concluded that narrower waveguides (W_{open} = 5 μm) have higher nonlinearity than wider waveguides (W_{open} = 7 μm) because of smaller effective mode area. The enhancement varies at different groups (locations) indicating the randomness of the nanoparticle distribution. However, Group 1 seems to have better enhancement than other groups regardless of the waveguide sizes. The maximum enhancement, which 10 times large, occurs in the waveguide with W_{open} = 5 μm in Group 1.

In summary, the gold nanoparticles can enhance the optical nonlinearity of silicon nitride trench waveguides. The conclusion is supported by the experimental results done on several waveguides with different locations on one wafer. Narrower waveguides have better enhancement effects due to their smaller mode areas.

5.5.2 Plasmon Optical Trapping by Boosting Evanescent Intensity Ratio

5.5.2.1 Introduction to Waveguide-Based Optical Trapping

Since the demonstration of the optical manipulation on small objects exploited by Ashkin [165], there have been enormous improvements in optical tweezing, which has the ability to trap and transport particles from several micrometers to a few hundred nanometers [166]–[168]. Many researchers and commercial products in this field have focused on free-space laser beam trapping which usually requires high-numerical-aperture lenses [169]. However, the high-numerical-aperture leads to a relatively narrow field of view and a very short focal length which prevents continuous transportation of nanoparticles. Alternatively, low-numerical-aperture can also be used in optical trapping[170]. This approach has been experimentally demonstrated by utilizing the interference patterns from multiple beams [170], two counter-propagating beams [165], and surface tension[171] to balance the axial scattering force. Nevertheless, no matter high- or low-numerical-aperture, these diffraction-limited systems have some fundamental drawbacks. To be specific, diffraction limits how tightly the beam can be focused, which affects the focal point intensity and intensity gradient, and thereby limits the total trapping strength. Besides, the lens-involved system is usually bulky, which is incompatible with the integrated lab-on-chip platform. In an attempt to address these issues, waveguide-based near-field methods [172]–[175] have been developed in the past decade.

Due to the lack of beam foci, waveguide-based systems rely on the gradient force in evanescent fields [176]. The evanescent field partially polarizes the particle resulting in an extremely strong Lorenz force analogous to the trapping force in the traditional optical

tweezers. However, these approaches suffer from the inefficient use of power since the evanescent field decays quickly outside the waveguide. This makes trapping particles smaller than 100 nm diameter difficult due to the weak light-matter interaction. To solve the problem, metallic structures are utilized to create local surface plasmons that enhance trapping strength [153], [177]. The enhanced near-field method has been widely used in optical tweezing such as nanoparticle trapping [178], molecules sensing [153], bio cell control [179], and particle transportation [180]–[182]. The use of an integrated planar waveguide for optical tweezing is often combined with optofluidic [183]–[185] to deliver particles. However, extra steps must be implemented to build microfluidic channels for these hybrid integrated plasmonic-photonic waveguides [186], [187]. Our Si_3N_4 trench waveguide has the capability to combine microfluidic channels and waveguides together [62], [188]. In this application presented here, analyte contained in the trapezoidal trench interacts with the field tailing away from the trench waveguide, which can be enhanced by a plasmonic bowtie antenna as shown in Figure 5-16.

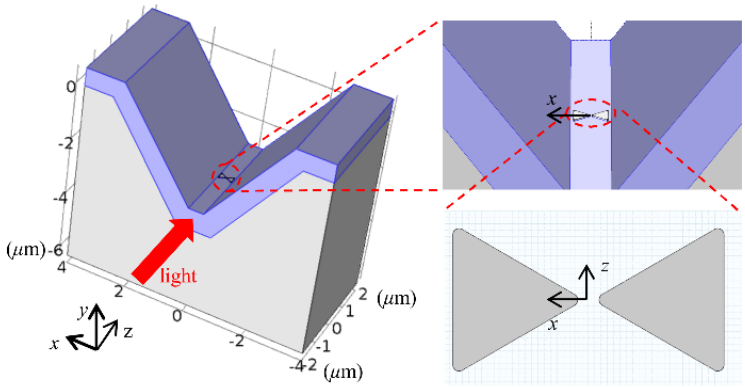

Figure 5-16. Schematic illustration of the proposed Si_3N_4 trench waveguide with a bowtie antenna for optical trapping. The gray colored region is the SiO_2 substrate, and the blue colored V-shaped volume is the Si_3N_4 guiding layer. The top cladding region is assumed to be water, and it is not shown in the figure to permit the bowtie antenna to be visible. The bowtie antenna is in the trench valley, sitting on top of the Si_3N_4 layer.

5.5.2.2 Nanoantenna Design

The optical gradient forces experienced by nanoparticles are typically very weak (some femtonewtons or less, and limited by the power handling capability), because the dipolar polarizability scales with the third power of the particle size [189]. Therefore, to confine nanoparticles against destabilizing effects such as the thermal fluctuations, a significantly higher optical power is in general required. Fortunately, the plasmonic nature of metal nanostructures and the scattering effects of nanoantennas can enhance the electrical field intensity and its gradient, such that stable trapping can be achieved at a much lower power. Bowtie antenna is one of the promising solutions to enhance the optical trapping force.

In recent years, bowtie antenna arrays for particle manipulation in objective lens configuration have been extensively studied [190]. When the incident light is linearly polarized across the gap of a bowtie antenna, capacitive effects lead to a confined and intense electric field spot in the antenna near-field, particularly within the gap. This hot spot both increases the field intensity and significantly boosts the intensity gradient. A bowtie antenna, made of two equilateral triangle gold patches separated by a gap along the *x*-direction, can be deposited using nanosphere lithography [191], [192]. The relative permittivity of the gold in this study is $\varepsilon_{r,Au}$ = -96.99 + *i*11.05 at 1550 nm wavelength according to the Brendel-Bormann model [34].

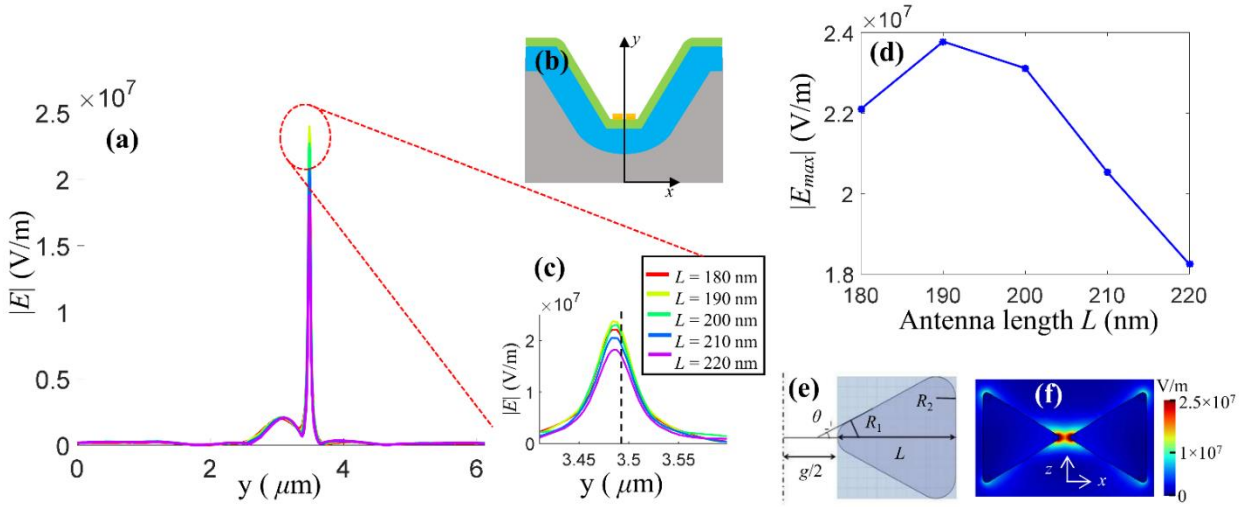

Figure 5-17. (a) Electrical field profile along the *y*-oriented cutline (*y*-axis) with different antenna lengths. The cutline is the *y*-axis in (b). The circled region in (a) is zoomed out in (c). The black dashed line in (c) represents the y-position corresponding to the antenna top surface. (d) The curve shows the maximum electric field with respect to different antenna lengths. (e) Half structure of a bowtie antenna, with g = 30 nm, R_1 = R_2 = 10 nm, θ = 30° in our case. (f) Electric field profile at the top surface of the antenna, in the *x*-*z* plane.

As shown in Figure 5-17(a), the electric field is greatly enhanced by the bowtie antenna. The sharp peak represents the resonant field in the antenna gap, whereas the smoother peak around y = 3 μm represents the maximum of the electric modal field inside the waveguide. The field distributions are plotted along the *y*-axis, Figure 5-17(b), and the origin is set to be at the bottom of the structure. The peak region circled in Figure 5-17(a) is zoomed out in Figure 5-17(c), illustrating the effect of the antenna length. The *y*-position of the antenna top surface is denoted as the dashed line in Figure 5-17(c). By manipulating the antenna length L shown in Figure 5-17(e), the maximum electric field strength in the antenna gap can be altered as shown in Figure 5-17(d). We choose L = 190 nm in our design as an optimum value. Although a smaller gap leads to a stronger field, the gap of the bowtie antenna is set to be 30 nm for the sake of particle trapping and relieving fabrication

limitations. The sharpness of the antenna tip will also affect the field strength. A smaller radius of curvature R_1 will lead to a higher field enhancement. Considering fabrication imperfections, we assume R_1 and R_2 to be 10 nm. The apex angle θ will play a role in the field enhancement, too. However, we fix θ to be 30° for simplicity. The antenna thickness has been optimized to be 20 nm in order to maximize the optical trapping force, which will be discussed later. In the simulation of 10 mW launched power at 1550 nm wavelength, the peak intensity in the antenna gap (10 nm above the waveguide) can be 60 times larger than the case when there is no antenna at the same location.

5.5.2.3 Optical Trapping Performance

The optical trapping system is composed of a trench waveguide with T = 725 nm, W_{btm} = 1.15 μm, and D = 3.5 μm and a bowtie antenna with L = 190 nm, g = 30 nm and T_m = 20 nm, where T_m is the metal thickness. The simulation results are obtained by using the built-in Maxwell stress tensor (MST) function in the RF module in the FEM-based solver COMSOL Multiphysics.

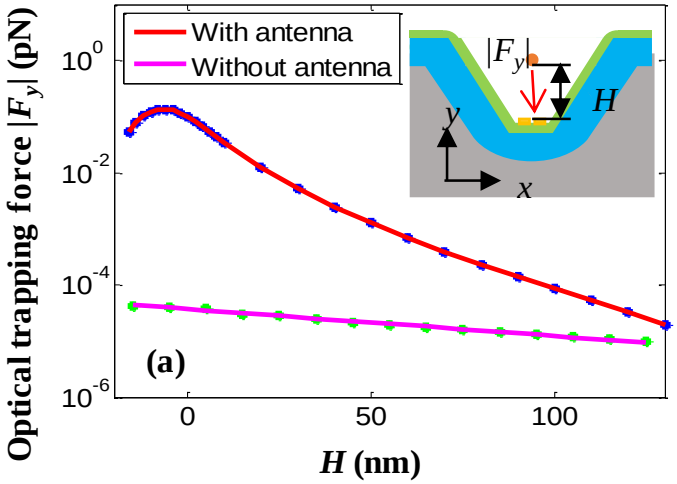

Figure 5-18. The magnitude of the downward trapping force along the negative *y*-direction versus the vertical distance *H*, from the particle bottom surface to the antenna top surface. The force enhanced by the bowtie antenna is compared with the one without a bowtie antenna, showing orders of magnitude force increases.

A polystyrene particle with 10 nm radius immersed in water is placed in the proximity of the gap of a bowtie plasmonic nanoantenna. The origin of the *y*-axis is set at the top surface of the bowtie nanoantennas. The vertical distance from the particle's bottom to the bowtie antenna top surface is denoted by *H*. Shown as the red curve in Figure 5-18, the force direction in the negative *y*-direction, and thus it is a pulling force which can be used for trapping. Note that the force is proportional to the guided power in the waveguide, and in the numerical analysis we assume the waveguide to be excited by a TE mode with a power of 10 mW. The trapping force magnitude increases first when it is in the antenna gap, for increasing *y*, and then decreases as the nanoparticle is located farther away from the antenna. Without the antenna, the optical force caused by the gradient of the evanescent wave decays exponentially as the particle lifts away from the waveguide, and it is several orders of magnitude weaker than the one with the bowtie antennas. With the enhancement, the maximum force occurs when the particle bottom surface is 6 nm below the antenna top surface, right in the gap of the antenna. At this position, the trapping force is boosted by 3 orders of magnitude compared to that occurring without antenna enhancement.

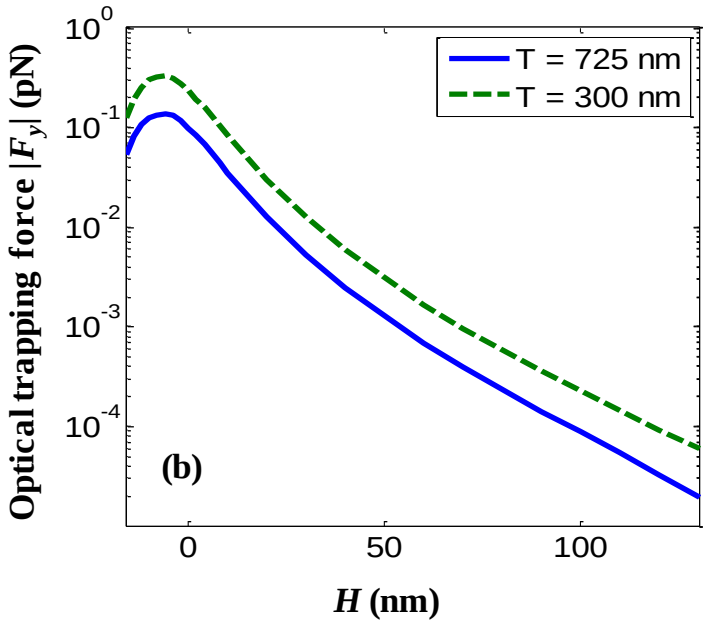

Figure 5-19. The magnitude of the vertical trapping force as a function of the vertical distance H and waveguide thickness T.

The thickness T of the waveguide affects *EIR*, which in turn influences optical forces. To quantify the influence, we compare the vertical trapping forces magnitude $|F_y|$ upon the same polystyrene particle on two different waveguides with different thicknesses as shown in Figure 5-19. $|F_y|$ is boosted nearly 3 times as the waveguide thickness shrinks from 725 nm to 300 nm. The result agrees with the aforementioned *EIR* study that higher *EIR* leads to strong light-matter interaction. The maximum force is 33 pN/W for our 300 nm thick waveguide, which is close to the value reported in [177] with the same antenna gap g = 30 nm and particle diameter 20 nm but a thinner waveguide h = 250 nm. We conclude that reducing our waveguide thickness will further improve the trapping force strength, and the results will be superior to previous work.

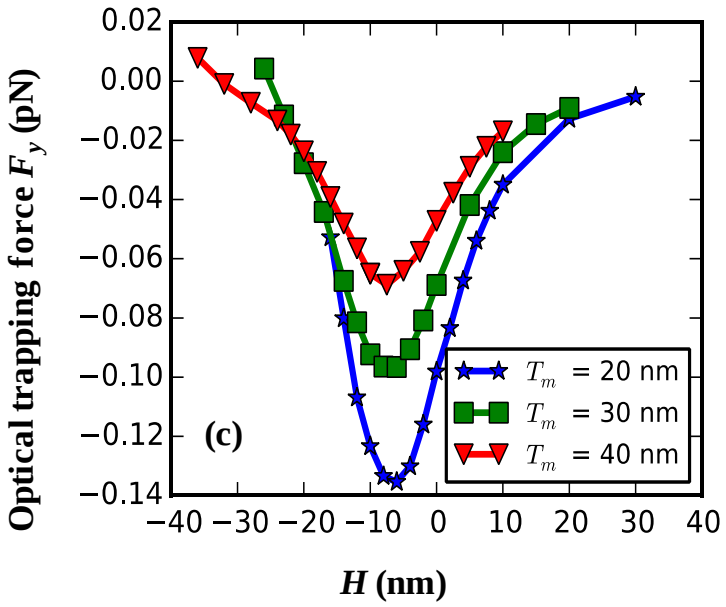

Figure 5-20. Effect of the antenna thickness on the vertical trapping forces: T_{m} stands for the bowtie metal thickness. The origin of the *y*-axis is set to be at the top surface of each antenna, and *H* is counted from the base of the particle to the origin. The results are generated for the trench waveguide with T = 725 nm, W_{top} = 500 nm, and W_{btm} = 1.15 μm.

The effect of the antenna thickness on the vertical trapping force has also been studied, and the results are illustrated in Figure 5-20. The origin of the *y*-axis is set to be the top surface of each antenna, and *H* is counted from the particle bottom surface with respect to the origin. We simulate the cases when the particle is in the gaps of the antennas that have three different thicknesses, 20 nm, 30 nm, and 40 nm. All the maxima occur when the particle bottom surface is around 6 nm below the antenna top surface. Thinner antenna gives stronger force magnitude. The comparison verifies that 20 nm metal thickness will facilitate optical trapping in our design. For given parameters, we find that there is a net gradient force that is always in the –*y*-direction for antenna thicknesses < 30 nm, that is pulling the particle toward the waveguide surface. There is no force repealing the particle

away from the waveguide. In addition, the buoyant force is smaller than the particle gravity of the polystyrene beads. Hence, it is safe to assume that the particle will be trapped at the waveguide surface. However, for a thick bowtie antenna (≥ 30 nm in Figure 5-20), there will be a net gradient force in the +*y*-direction as the particle gets closer to the waveguide surface. Thus, the particle may not be trapped on the waveguide surface.

Besides particle trapping the vertical direction, the scenarios of a flowing nanoparticle passing through the antenna gap are also studied. It is assumed that the nanoparticle keeps the same height, 5 nm above the nanoantennas top surface (H = 5 nm), during its movement in the *z*- and *x*-direction. Several situations are considered as shown in Figure 5-21(a): the nanoparticle passing along a trajectory coinciding with the *z*-axis, along the antenna center (x = 0); the particle passing near the symmetric axis of the antenna (x = 10 nm, x = 30 nm and x = 50 nm); the particle passing along the *x*-axis. The optical force components in the *x*, *y* and *z* directions are computed numerically and curve-fitted as the nanoparticle moves along the trajectories as shown in Figure 5-21(b), (c), (d), (e), and (f).

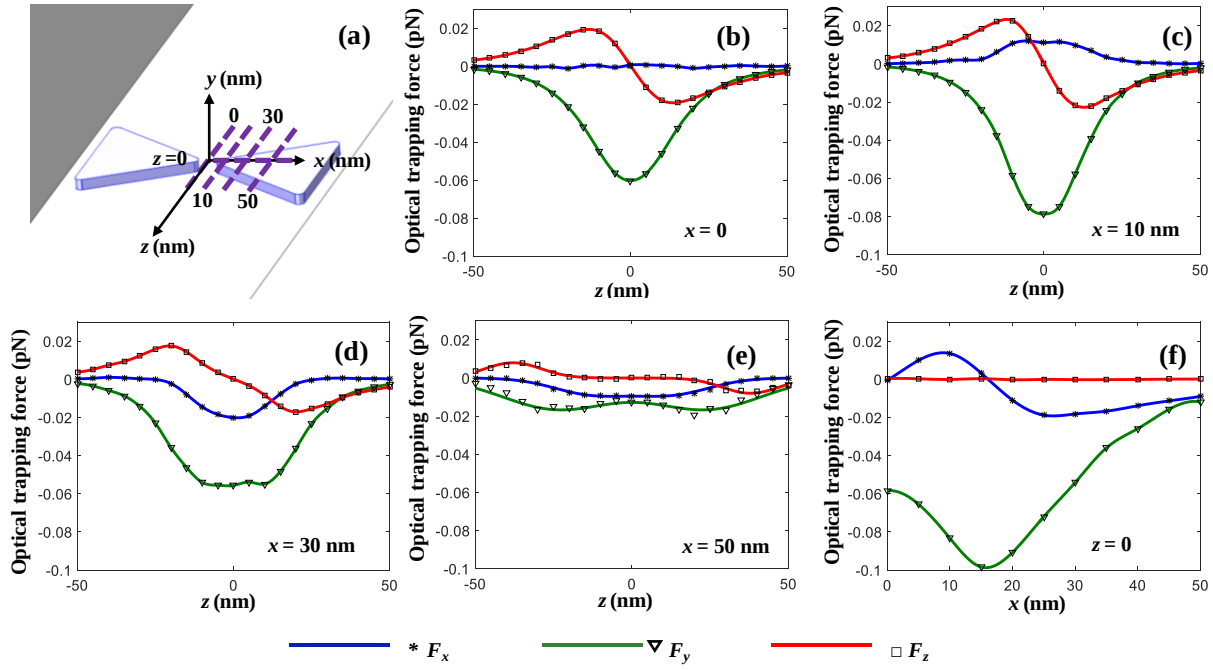

Figure 5-21. Simulation of the optical trapping forces on a nanoparticle flowing in the z direction and in the x-direction with 10 mW input power. (a) The nanoparticle moves along the dashed z-oriented lines from z = -50 nm to z = 50 nm and the dashed x-oriented line from x = 0 to x = 50 nm. The four z-oriented dashed lines represent the cases when the particle is in the center (x = 0) and away from the antenna central symmetric axis (x = 10 nm, x = 30 nm, x = 50 nm). The x-oriented dashed line represents the case when the particle moves along the x-axis (z = 0). The vertical distance H is kept the same in all cases, with the nanoparticle bottom surface 5 nm above the antenna top surface (H = 5 nm). Optical trapping force components upon the nanoparticle when x = 0 (b), x = 10 nm (c), x = 30 nm (d), x = 50 nm (e) and z = 0 (f).

When the nanoparticle flows along the z-axis (x = 0) as shown in Figure 5-21(b), the vertical optical force F_y remains negative, indicating the force is pulling the particle downwards. The longitudinal force F_z changes its sign corresponding to the particle position. In particular, when z is positive, F_z is negative, and vice versa, which means the optical force F_z tends to attract the nanoparticle back when it moves away from the antenna center. The maximum F_z occurs when the particle is 10 nm away from the center.

The horizontal force F_x is negligible compared to the other two components, and it is expected to be zero ideally because of symmetry reasons. Ripples in F_x may arise from numerical errors due to finite mesh size and nonsymmetrical mesh. The force profiles in the case when x = 10 nm (Figure 5-21(c)) are similar to the case when x = 0, except that F_x becomes significant compared to the other force components. F_x is initially positive when x is positive, meaning that the force repels the particle away from the antenna gap in the +x direction. When the particle is further away from the antenna center, i.e., x = 30 nm, as shown in Figure 5-21(d), F_y and F_z become weaker. However, F_x changes its sign. F_x becomes negative when x is positive, indicating that the force pulls the particle towards the antenna gap in the -x-direction. When the particle is even further away from the antenna gap, i.e., x = 50 nm, as shown in Figure 5-21(e), the force profiles resemble those in Figure 5-21(d), but have smaller magnitudes. The opposite F_x force profiles in Figure 5-21(c) and Figure 5-21(d) imply that the particle might be trapped at the antenna tips. To further investigate the trapping locations, we simulate the case when the particle position is swept along the x-axis (z = 0). As shown in Figure 5-21(f), F_x changes its sign and F_y reaches the maximum magnitude at x = 15 nm. F_z remains close to zero during the movement due to the symmetry of the structure and the subwavelength size of the nanoantenna. The profiles indicate that the nanoparticle will be trapped to the antenna tips, because the antenna tips in our design are located at x = ±15 nm. The results are reasonable, since the gradient force tends to drive the particle towards the highest intensity region if the particle is optically denser than the surrounding medium. Therefore, the particles will be trapped to the antenna tips. This conclusion can also be confirmed by the intensity profile of the antenna as shown in Figure 5-17(f).

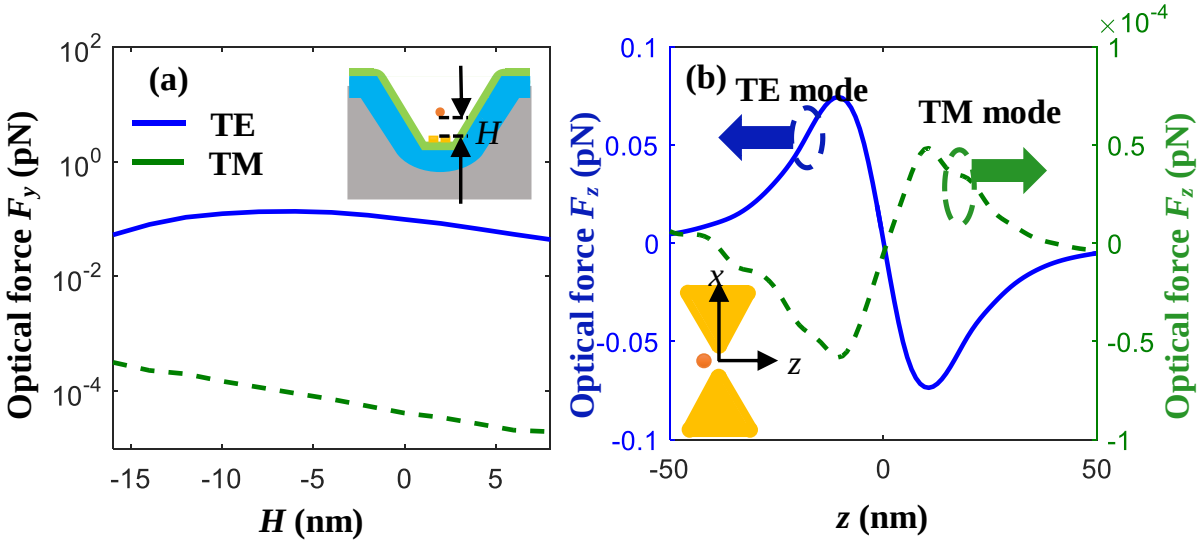

Figure 5-22. (a) Magnitude of vertical optical forces F_y generated by the TE and TM propagation modes in the Si_3N_4 trench waveguide with W_{top} = 500 nm and T = 725 nm. The particle is at the antenna center in the x-z plane, but moves vertically from H = -15 nm to H = 8 nm. (b) The longitudinal optical force F_z generated by the TE and TM propagation modes in the same waveguide. The particle remains the same height H = -6 nm and flows along the center line of the antenna from z = -50 nm to z = 50 nm. The input power is 10 mW.

The aforementioned optical forces are generated by the antenna scattering excited by a propagating TE mode in the waveguide. We also investigated the optical trapping force generated by a TM mode propagating in the same waveguide. The vertical forces caused by different propagation modes near the antenna region are compared and illustrated in Figure 5-22(a). The simulation mainly covers the case when the particle falls into the antenna gap, i.e., for H ranging from -15 nm to 8 nm, where the trapping force is the strongest. The vertical force F_y generated by the TE wave is at least 2 orders of magnitude larger than that generated by the TM wave. Here we recall that the bowtie nanoantenna orientation is set to match with the electric field of the TE mode, whereas the TM mode fails to excite the nanoantenna leading to much weaker scattering and near field. The

longitudinal force F_z is also simulated in Figure 5-22(b) by moving the particle along the center line of the antenna along the z-direction while keeping the same height H = -6 nm. Compared to the TE mode, the longitudinal force F_z in the TM mode is negligible. Importantly, the force F_z has the same sign as position z, indicating it is a repelling force and loses the trapping functionality. Thereby, the mode polarization severely affects the trapping functionality. In general, TE mode is used for optical trapping, while switching to TM mode can help release the particle from the antenna.

5.5.2.4 Semi-Analytical Verification

The optical trapping performances, presented in the last session, are simulated by a FEM solver using the Maxwell stress tensor (MST) method. To simulate the optical force at each particle position, the software has to solve the mode distribution and integrate the Maxwell stress tensor, which takes tremendous computing resources to simulate the nanostructures in a micro-size model. An analytical method is discussed here to relieve the computation efforts by extracting the field distributions from a one-time full-wave simulation and calculating the optical force relying on the extracted fields. For optical trapping in Rayleigh regime, i.e., when the particle size is much smaller than the wavelength, a dipole approximation can be used to analytically describe the force upon the particle [193], [194]. The induced dipole polarizability influences the interaction strength with an optical field. For a sphere of radius a and relative electric permittivity ε_{r1}, using SI units, the point-like particle polarizability α_0 is approximately given by the Clausius-Mossotti relation [193],

$$\alpha_0 = 4\pi\varepsilon_0\varepsilon_{r2}a^3\frac{\varepsilon_{r1}-\varepsilon_{r2}}{\varepsilon_{r1}+2\varepsilon_{r2}} \tag{5.5.2}$$

where ε_{r1} = 2.46 is the polystyrene nanoparticle's relative permittivity, ε_{r2} = 1.77 is the host medium relative permittivity, and ε_0 is the vacuum permittivity. If taken the reaction of a finite-size dipole to the scattered field at its own location into consideration, i.e., accounting for radiation losses, the Clausius-Mossotti relation can be corrected as follows [194]:

$$\alpha = \frac{\alpha_0}{1-\frac{ik_2{}^3\alpha_0}{6\pi\varepsilon_{r2}\varepsilon_0}} \tag{5.5.3}$$

where k_2 is the wavenumber in the host medium.

The explicit form of the time-averaged force acting on such a dipole is in Ref.[194],

$$\langle\mathbf{F}\rangle = \frac{1}{4}\mathrm{Re}(\alpha)\nabla|\mathbf{E}|^2 + \frac{\sigma}{2c}\mathrm{Re}\left(\mathbf{E}\times\mathbf{H}^*\right) + \frac{\sigma c\varepsilon_2}{4\omega i}\nabla\times\left(\mathbf{E}\times\mathbf{E}^*\right) \tag{5.5.4}$$

where the total (or extinction) cross-section of the particle $\sigma = k_2\,\mathrm{Im}\{\alpha\}/\varepsilon_2$ [195]. The first term on the right-hand side of the equation is the optical gradient force, the second term represents radiation pressure and the third one is the polarization gradient force. The particle cross section σ scales with a^6 (a is particle radius) when the particle size is smaller than the wavelength [196], thus the magnitude of the radiation pressure and polarization gradient force is several orders smaller than the optical gradient force and can be neglected. Given that the particle size is sufficiently small (a = 10 nm) compared to the wavelength (1550 nm), perturbation theory can be applied such that the field experienced by the nanoparticle can be calculated from the evanescent fields in the cladding without the existence of the particle. In addition, we do not consider the case where the particle falls into the antenna gap to avoid self-induced back-action [197]. Thus, the electric field experienced by the nanoparticle is approximately represented by the scattering field of the antenna itself [195]. We scrutinize the vertical optical force F_y in the region where the

polystyrene sphere is lifted from H = 10 nm to H = 110 nm (we recall H is the distance from the bowtie top surface to the bottom of the nanoparticle). Thereby, by retaining only the first term of the Eq. (5.5.4), it can be written in the following way in favor of calculating F_y.

$$\left\langle F_y \right\rangle \approx \frac{1}{4}\mathrm{Re}(\alpha)\frac{\partial}{\partial y}\left(\left|E_x\right|^2+\left|E_y\right|^2+\left|E_z\right|^2\right) \tag{5.5.5}$$

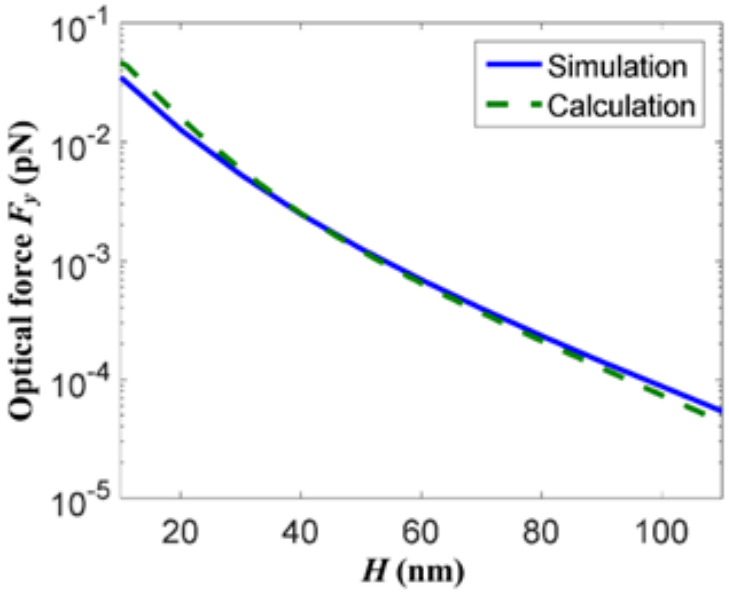

Figure 5-23. Comparison of force computations. The analytic optical force is evaluated based on Eq. (5.5.5) and compared with the total force simulated by using a FEM-based full-wave method combined with a Maxwell stress tensor method.

In the data processing, we extract the electric fields in the cladding for simplicity and calculate the fields experienced by the nanoparticle using the electric displacement continuity equation. To reduce the noise effect that comes from numerical errors, the data are fitted by exponential curves. We calculate the optical trapping force in the y-direction, and compare it with the previous full-wave results obtained by using the MST method in COMSOL, as shown in Figure 5-23. The calculated optical gradient force well matches the full-wave simulated force. Both methods (full-wave and semi-analytical) are in agreement

at all locations. Despite a small discrepancy which may result from imperfect curve fitting, the trend versus distance is the same and the results show consistency. The semi-analytical method used in this section is not limited to trench waveguides but can be applied to other waveguide-based trapping systems as well. It provides a fast approach for estimating optical forces on particles in the Rayleigh regime. Instead of solving for the field distribution and calculating the optical force at every particle position, one can extract the field distribution from a simulation and use it to calculate the force gradient and thus the optical force. The limitation of the approach, however, is that the presence of the particle should behave as a small perturbation to the local fields and not perturbs the field distribution significantly.

5.6 Summary

In summary, Si_3N_4 trench waveguide is thoroughly investigated and studied in this chapter. The trench waveguide shape relies on the silicon wet etching properties. By controlling the etching time and the top opening window, the core region of the trench waveguide can be in triangle or trapezoidal shapes. Triangle trench waveguide has better mode confinement and its fundamental mode is quasi-TM mode. Thus TM mode has lower propagation loss than its TE counterparts. Experimental results show that the propagation loss of the TM mode can be as low as 0.8 dB/cm. Since TM mode has smaller mode area, it is better for nonlinear applications. The nonlinear parameter of the waveguide is measured to be 0.3 W^{-1}/m. Coating gold nanoparticles can enhance the waveguide nonlinearity because the localized hot spots generate the intense electric field, which boosts the nonlinear response of the waveguides. The trench waveguide can be used for sensing and

optical trapping applications, thanks to its unique cross-section. Both TM and TE modes can be used since they are similar *EIR*. It is worth noting that TE mode is favored when the waveguide is integrated with antennas because planar antenna structures need a tangential electric field for excitation. Explorations on the trapezoidal trench waveguide and bowtie antennas show that the platform is suitable for trapping nanoparticles. Switching between trapping and releasing the particles can be done by changing the mode polarization states from the TE mode to the TM mode.

Conclusion

In summary, this dissertation has investigated the prospects of the Si_3N_4 waveguide-based devices as a platform for integrated optical communication and sensing applications. The benefits of using Si_3N_4 material are elaborated in Chapter 1. Although Si_3N_4 is utilized in different applications for various reasons, it is its compatibility with Si and SiO_2 platforms that renders the material ubiquitous in optical planar devices. The thesis covers three Si_3N_4 waveguide-based integrated devices, being optical leaky wave antennas, a plasmo-thermomechanical radiation detector, and trench waveguides.

The early part of the thesis focuses on optical leaky wave antennas. The leaky wave theory, device fabrication, and device characterization are reported. The quasi-far-field radiation pattern of the OLWA has been experimentally characterized. The OLWA had a single directive radiation peak at the angle 85.1° in the range from 65° to 112° at the wavelength of 1550 nm. The sidelobe level is at least 7 dB lower than the main peak. The peak radiation angle moves to the broad side as the wavelength increases. The device can find promising applications in optical communications, especially for multi-wavelength space division applications owing to its capability of beam scanning with frequency, e.g. launching different wavelengths to multi-core fibers. As for radiation beam modulation, the Si nanowires can be utilized for optical and electronic modulation. We proposed using doped Si wires to form *p*-*n* junctions embedded inside the Si_3N_4 waveguide. Refractive index around the *p*-*n* junction regions can be altered by the carrier plasma effect, thus changing the radiation intensity at a specific angle. The electrical modulation effects can be

further boosted by integrating the OLWA into resonators. This study elaborates the emission properties of the OLWA and potential modulation methods on the radiation pattern.

The second part of the thesis presents the plasmo-thermomechanical radiation detector, including the design procedure, fabrication flow, and experimental characterization. Two structures have been designed and optimized for 4.3 μm and 785 nm target wavelengths. The optimum unit cell for the 4.3 μm wavelength has a strip length L_s = 1.77 μm, a strip width W_s = 100 nm, a beam width W_b = 100 nm, periods in x and z direction $P_x = P_z$ = 3.1 μm, and an absorption coefficient of 42.4%. The optimum unit cell for 785 nm wavelength has L_s = 350 nm, W_s = 100 nm, W_b = 100 nm, $P_x = P_z$ = 660 nm, and an absorption coefficient of 33.8%. For demonstration purposes, only the antenna for 785 nm wavelength is fabricated. The device is composed of 13 fishbone nanowires with a period of 660 nm. With the help of HF vapor etching, the wires are suspended 62 nm above the waveguide. Each wire is 12.54 μm long and consists of 16 nanoantennas with a period of 660 nm. During the optical characterization experiments, the 660 nm laser, instead of 785 nm laser, is employed due to its high power and the fact that the device wavelength response is blue shifted. Under 660 nm polarized light illumination, the device shows a responsivity of 3.954×10^{-3} $\mu m^2/\mu W$. The noise equivalent power, dominated by the waveguide coupling instability, is 3.01 $\mu W/\sqrt{Hz}$. The 3dB bandwidth of the device is 9.6 Hz corresponding to a time constant of 16.6 ms. The threshold of the device is limited by noise. Reducing the system noise can further improve the signal-to-noise ratio, thus lowering the noise equivalent power. This work verifies that the thermo-mechanical vibration can be detected by on-chip waveguide-based optical readout system.

The third part of the thesis emphasizes on Si_3N_4 trench waveguides. The trench waveguide shape relies on the silicon wet etching properties. By controlling the etching time and the top opening window, the core region of the trench waveguide can be in either triangle or trapezoidal shapes. The triangle trench waveguide has better mode confinement and its fundamental mode is quasi-TM mode. Thus, TM mode has lower propagation loss than its TE counterparts. Experimental results show that the propagation loss of the TM mode can be as low as 0.8 dB/cm. Since the TM mode has a smaller mode area, it is better for nonlinear applications. The nonlinear parameter of the waveguide is measured to be 0.3 W^{-1}/m. Coating gold nanoparticles can enhance the waveguide nonlinearity because the localized hot spots generate an intense electrical field, which boosts the nonlinear response of the waveguides. The trench waveguide can be used for sensing and optical trapping applications, thanks to its unique cross-section. Both TM and TE modes can be used since they are similar *EIR*. It is worth noting that TE mode is favored when the waveguide is integrated with antennas because planar antenna structures need a tangential electric field for excitation. Explorations on the trapezoidal trench waveguide and bowtie antennas show that the platform is suitable for trapping nanoparticles. Switching between trapping and releasing the particles can be done by changing the mode polarization states from the TE mode to the TM mode.

These results prove that silicon nitride is a versatile material for photonics integration. The wide application of silicon nitride not only benefits from CMOS fabrication compatibility, but also attributes to its excellent optical properties. Silicon nitride has the capability to add new functionalities to conventional Si photonics. Future work following

the dissertation can benefit the fields of 3D photonics integration and biosensing by exploiting novel device design and Raman spectroscopy.

Reference

[1] S. E. Miller, "Integrated optics: An introduction," *Bell Syst. Tech. J.*, vol. 48, no. 7, pp. 2059–2069, Sep. 1969.

[2] T. Baehr-Jones, T. Pinguet, P. Lo Guo-Qiang, S. Danziger, D. Prather, and M. Hochberg, "Myths and rumours of silicon photonics," *Nat. Photonics*, vol. 6, no. 4, pp. 206–208, Apr. 2012.

[3] A. Rickman, "The commercialization of silicon photonics," *Nat. Photonics*, vol. 8, no. 8, pp. 579–582, Aug. 2014.

[4] L. Vivien and L. Pavesi, *Handbook of Silicon Photonics*. Taylor & Francis, 2016.

[5] W. Stutius and W. Streifer, "Silicon nitride films on silicon for optical waveguides," *Appl. Opt.*, vol. 16, no. 12, pp. 3218–3222, Dec. 1977.

[6] C.-E. Morosanu, "The preparation, characterization and applications of silicon nitride thin films," *Thin Solid Films*, vol. 65, no. 2, pp. 171–208, Jan. 1980.

[7] S. Sriram, W. D. Partlow, and C. S. Liu, "Low-loss optical waveguides using plasma-deposited silicon nitride," *Appl. Opt.*, vol. 22, p. 3664, Dec. 1983.

[8] C. H. Henry, R. F. Kazarinov, H. J. Lee, K. J. Orlowsky, and L. E. Katz, "Low loss Si3N4?SiO2 optical waveguides on Si," *Appl. Opt.*, vol. 26, no. 13, pp. 2621–2624, Jul. 1987.

[9] H. J. Lee, C. H. Henry, K. J. Orlowsky, R. F. Kazarinov, and T. Y. Kometani, "Refractive-index dispersion of phosphosilicate glass, thermal oxide, and silicon nitride films on silicon," *Appl. Opt.*, vol. 27, no. 19, pp. 4104–4109, Oct. 1988.

[10] R. G. Heideman, R. P. H. Kooyman, and J. Greve, "Performance of a highly sensitive optical waveguide Mach-Zehnder interferometer immunosensor," *Sens. Actuators B Chem.*, vol. 10, no. 3, pp. 209–217, Feb. 1993.

[11] E. F. Schipper, A. M. Brugman, C. Dominguez, L. M. Lechuga, R. P. H. Kooyman, and J. Greve, "The realization of an integrated Mach-Zehnder waveguide immunosensor in silicon technology," *Sens. Actuators B Chem.*, vol. 40, no. 2, pp. 147–153, May 1997.

[12] C. T. Sullivan, S. D. Habermehl, G. A. Vawter, J. Guo, and M. J. Shaw, "Fabrication Techniques for Low Loss Silicon Nitride Waveguides.," Sandia National Laboratories, SAND2005–0434C, Jan. 2005.

[13] M. Melchiorri *et al.*, "Propagation losses of silicon nitride waveguides in the near-infrared range," *Appl. Phys. Lett.*, vol. 86, no. 12, p. 121111, Mar. 2005.

[14] S. C. Mao *et al.*, "Low propagation loss SiN optical waveguide prepared by optimal low-hydrogen module," *Opt. Express*, vol. 16, no. 25, pp. 20809–20816, Dec. 2008.

[15] J. F. Bauters *et al.*, "Ultra-low-loss high-aspect-ratio Si3N4 waveguides," *Opt. Express*, vol. 19, no. 4, pp. 3163–3174, Feb. 2011.

[16] J. F. Bauters *et al.*, "Planar waveguides with less than 0.1 dB/m propagation loss fabricated with wafer bonding," *Opt. Express*, vol. 19, no. 24, pp. 24090–24101, Nov. 2011.

[17] S. Romero-García, F. Merget, F. Zhong, H. Finkelstein, and J. Witzens, "Silicon nitride CMOS-compatible platform for integrated photonics applications at visible

wavelengths," *Opt. Express*, vol. 21, no. 12, pp. 14036–14046, Jun. 2013.
[18] A. Z. Subramanian *et al.*, "Low-Loss Singlemode PECVD Silicon Nitride Photonic Wire Waveguides for 532 #x2013;900 nm Wavelength Window Fabricated Within a CMOS Pilot Line," *IEEE Photonics J.*, vol. 5, no. 6, pp. 2202809–2202809, Dec. 2013.
[19] K. Luke, Y. Okawachi, M. R. E. Lamont, A. L. Gaeta, and M. Lipson, "Broadband mid-infrared frequency comb generation in a Si_3N_4 microresonator," *Opt. Lett.*, vol. 40, no. 21, p. 4823, Nov. 2015.
[20] L. Chen, C. R. Doerr, L. Buhl, Y. Baeyens, and R. A. Aroca, "Monolithically Integrated 40-Wavelength Demultiplexer and Photodetector Array on Silicon," *IEEE Photonics Technol. Lett.*, vol. 23, no. 13, pp. 869–871, Jul. 2011.
[21] W. D. Sacher *et al.*, "Polarization rotator-splitters and controllers in a Si_3N_4-on-SOI integrated photonics platform," *Opt. Express*, vol. 22, no. 9, pp. 11167–11174, May 2014.
[22] M. Sodagar, R. Pourabolghasem, A. A. Eftekhar, and A. Adibi, "High-efficiency and wideband interlayer grating couplers in multilayer Si/SiO_2/SiN platform for 3D integration of optical functionalities," *Opt. Express*, vol. 22, no. 14, p. 16767, Jul. 2014.
[23] W. D. Sacher, Y. Huang, G.-Q. Lo, and J. K. S. Poon, "Multilayer Silicon Nitride-on-Silicon Integrated Photonic Platforms and Devices," *J. Light. Technol.*, vol. 33, no. 4, pp. 901–910, Feb. 2015.
[24] Q. Zhao, C. Guclu, Y. Huang, F. Capolino, and O. Boyraz, "Experimental Demonstration of Directive Si3N4 Optical Leaky Wave Antennas With Semiconductor Perturbations," *J. Light. Technol.*, vol. 34, no. 21, pp. 4864–4871, Nov. 2016.
[25] Q. Zhao, M. Rajaei, and O. Boyraz, "Silicon Nitride on Silicon-on-Insulator: a Platform for Integration Active Control over Passive Components," 2016, p. JW2A.125.
[26] K. Ikeda, R. E. Saperstein, N. Alic, and Y. Fainman, "Thermal and Kerr nonlinear properties of plasma-deposited silicon nitride/ silicon dioxide waveguides," *Opt. Express*, vol. 16, no. 17, p. 12987, Aug. 2008.
[27] R. Amatya *et al.*, "Low Power Thermal Tuning of Second-order Microring Resonators," in *2007 Conference on Lasers and Electro-Optics (CLEO)*, 2007, pp. 1–2.
[28] J. C. Maxwell, *A treatise on electricity and magnetism*. Oxford : Clarendon Press, 1873.
[29] S. H. Hall and H. L. Heck, *Advanced Signal Integrity for High-Speed Digital Designs*. John Wiley & Sons, 2011.
[30] J. H. Poynting, "On the Transfer of Energy in the Electromagnetic Field," *Philos. Trans. R. Soc. Lond.*, vol. 175, pp. 343–361, Jan. 1884.
[31] A. Yariv and P. Yeh, *Photonics: Optical Electronics in Modern Communications*. Oxford University Press, 2007.
[32] G. B. Hocker and W. K. Burns, "Mode dispersion in diffused channel waveguides by the effective index method," *Appl. Opt.*, vol. 16, no. 1, pp. 113–118, Jan. 1977.
[33] C. Bishop, "The Relationship Between Loss, Conductivity, and Dielectric Constant," *Adv. Eng. Electromagn.*, 2001.
[34] A. D. Rakic, A. B. Djurišic, J. M. Elazar, and M. L. Majewski, "Optical Properties of Metallic Films for Vertical-Cavity Optoelectronic Devices," *Appl. Opt.*, vol. 37, no. 22, pp. 5271–5283, Aug. 1998.
[35] S. A. Maier, *Plasmonics: Fundamentals and Applications*. Springer Science & Business Media, 2007.

[36] U. Kreibig and M. Vollmer, “Theoretical Considerations,” in *Optical Properties of Metal Clusters*, Springer, Berlin, Heidelberg, 1995, pp. 13–201.
[37] E. Hutter and J. H. Fendler, “Exploitation of Localized Surface Plasmon Resonance,” *Adv. Mater.*, vol. 16, no. 19, pp. 1685–1706, Oct. 2004.
[38] V. Giannini, A. I. Fernández-Domínguez, S. C. Heck, and S. A. Maier, “Plasmonic Nanoantennas: Fundamentals and Their Use in Controlling the Radiative Properties of Nanoemitters,” *Chem. Rev.*, vol. 111, no. 6, pp. 3888–3912, Jun. 2011.
[39] D. R. Jackson and A. A. Oliner, “Leaky-wave antennas,” *Mod. Antenna Handb.*, vol. 1, pp. 325–368, 2008.
[40] W. W. Hansen, “Radiating electromagnetic wave guide,” US2402622 A, 25-Jun-1946.
[41] A. A. Oliner, “Leaky-Wave Antennas,” in *Antenna Engineering Handbook*, R. C. Hohnson, Ed., New York: McGraw Hill, 1993.
[42] A. Andreone, “Linear and Planar Periodic Arrays of Metallic Nanospheres: Fabrication, Optical Properties and Applications,” in *Photonic Crystals and Metamaterials*, World Scientific, 2011.
[43] T. Thio, K. M. Pellerin, R. A. Linke, H. J. Lezec, and T. W. Ebbesen, “Enhanced light transmission through a single subwavelength aperture,” *Opt. Lett.*, vol. 26, no. 24, p. 1972, Dec. 2001.
[44] T. Thio *et al.*, “Giant optical transmission of sub-wavelength apertures: physics and applications,” *Nanotechnology*, vol. 13, no. 3, p. 429, Jun. 2002.
[45] A. Degiron and T. W. Ebbesen, “Analysis of the transmission process through single apertures surrounded by periodic corrugations,” *Opt. Express*, vol. 12, no. 16, p. 3694, 2004.
[46] D. R. Jackson *et al.*, “The Fundamental Physics of Directive Beaming at Microwave and Optical Frequencies and the Role of Leaky Waves,” *Proc. IEEE*, vol. 99, no. 10, pp. 1780–1805, Oct. 2011.
[47] D. R. Jackson, J. Chen, R. Qiang, F. Capolino, and A. A. Oliner, “The role of leaky plasmon waves in thedirective beaming of light through asubwavelength aperture,” *Opt. Express*, vol. 16, no. 26, pp. 21271–21281, Dec. 2008.
[48] X.-X. Liu and A. Alù, “Subwavelength leaky-wave optical nanoantennas: Directive radiation from linear arrays of plasmonic nanoparticles,” *Phys. Rev. B*, vol. 82, no. 14, p. 144305, Oct. 2010.
[49] S. Campione, S. Steshenko, and F. Capolino, “Complex bound and leaky modes in chains of plasmonic nanospheres,” *Opt. Express*, vol. 19, no. 19, pp. 18345–18363, Sep. 2011.
[50] S. Campione and F. Capolino, “Waveguide and radiation applications of modes in linear chains of plasmonic nanospheres,” in *Proceedings of 2013 URSI International Symposium on Electromagnetic Theory (EMTS)*, 2013, pp. 172–175.
[51] F. K. Schwering and S.-T. Peng, “Design of Dielectric Grating Antennas for Millimeter-Wave Applications,” *IEEE Trans. Microw. Theory Tech.*, vol. 31, no. 2, pp. 199–209, Feb. 1983.
[52] A. Alphones and M. Tsutsumi, “Leaky wave radiation from a periodically photoexcited semiconductor slab waveguide,” *IEEE Trans. Microw. Theory Tech.*, vol. 43, no. 9, pp. 2435–2441, Sep. 1995.
[53] A. Rofougaran and M. Rofougaran, “Method and system for a smart antenna utilizing leaky wave antennas,” US8432326 B2, 30-Apr-2013.

[54] D. J. Richardson, J. M. Fini, and L. E. Nelson, “Space-division multiplexing in optical fibres,” *Nat. Photonics*, vol. 7, no. 5, pp. 354–362, May 2013.
[55] J. Sakaguchi *et al.*, “305 Tb/s Space Division Multiplexed Transmission Using Homogeneous 19-Core Fiber,” *J. Light. Technol.*, vol. 31, no. 4, pp. 554–562, Feb. 2013.
[56] P. Baues, H. Mahlein, A. Reichelt, and G. Winzer, “Controllable, electro-optical grating coupler,” US4006963 A, 08-Feb-1977.
[57] D. Taillaert *et al.*, “An out-of-plane grating coupler for efficient butt-coupling between compact planar waveguides and single-mode fibers,” *IEEE J. Quantum Electron.*, vol. 38, no. 7, pp. 949–955, Jul. 2002.
[58] Q. Song, S. Campione, O. Boyraz, and F. Capolino, “Silicon-based optical leaky wave antenna with narrow beam radiation,” *Opt. Express*, vol. 19, no. 9, pp. 8735–8749, Apr. 2011.
[59] S. Campione, C. Guclu, Q. Song, O. Boyraz, and F. Capolino, “An optical leaky wave antenna with Si perturbations inside a resonator for enhanced optical control of the radiation,” *Opt. Express*, vol. 20, no. 19, pp. 21305–21317, Sep. 2012.
[60] C. Guclu, S. Campione, O. Boyraz, and F. Capolino, “Theory of a Directive Optical Leaky Wave Antenna Integrated into a Resonator and Enhancement of Radiation Control,” *J. Light. Technol.*, vol. 32, no. 9, pp. 1741–1749, May 2014.
[61] M. J. R. Heck, J. F. Bauters, M. L. Davenport, D. T. Spencer, and J. E. Bowers, “Ultra-low loss waveguide platform and its integration with silicon photonics,” *Laser Photonics Rev.*, vol. 8, no. 5, pp. 667–686, Sep. 2014.
[62] Y. Huang, Q. Zhao, L. Kamyab, A. Rostami, F. Capolino, and O. Boyraz, “Sub-micron silicon nitride waveguide fabrication using conventional optical lithography,” *Opt. Express*, vol. 23, no. 5, pp. 6780–6786, Mar. 2015.
[63] G. K. Celler and S. Cristoloveanu, “Frontiers of silicon-on-insulator,” *J. Appl. Phys.*, vol. 93, no. 9, pp. 4955–4978, May 2003.
[64] C. A. Balanis, “Chapter 4 Linear Wire Antennas,” in *Antenna Theory: Analysis and Design*, 3rd ed., John Wiley & Sons, 2005, p. 170.
[65] G. T. Reed, G. Mashanovich, F. Y. Gardes, and D. J. Thomson, “Silicon optical modulators,” *Nat. Photonics*, vol. 4, no. 8, pp. 518–526, Aug. 2010.
[66] A. Liu *et al.*, “A high-speed silicon optical modulator based on a metal–oxide–semiconductor capacitor,” *Nature*, vol. 427, no. 6975, pp. 615–618, Feb. 2004.
[67] A. Liu *et al.*, “High-speed optical modulation based on carrier depletion in a silicon waveguide,” *Opt. Express*, vol. 15, no. 2, pp. 660–668, Jan. 2007.
[68] B. O. Seraphin and N. Bottka, “Franz-Keldysh Effect of the Refractive Index in Semiconductors,” *Phys. Rev.*, vol. 139, no. 2A, pp. A560–A565, Jul. 1965.
[69] M. J. Kerr and A. Cuevas, “Recombination at the interface between silicon and stoichiometric plasma silicon nitride,” *Semicond. Sci. Technol.*, vol. 17, no. 2, p. 166, Feb. 2002.
[70] Q. Xu, S. Manipatruni, B. Schmidt, J. Shakya, and M. Lipson, “12.5 Gbit/s carrier-injection-based silicon micro-ring silicon modulators,” *Opt. Express*, vol. 15, no. 2, p. 430, Jan. 2007.
[71] A. Rogalski, “Infrared detectors: status and trends,” *Prog. Quantum Electron.*, vol. 27, no. 2–3, pp. 59–210, 2003.
[72] N. J. Hogan, A. S. Urban, C. Ayala-Orozco, A. Pimpinelli, P. Nordlander, and N. J. Halas,

"Nanoparticles Heat through Light Localization," *Nano Lett.*, vol. 14, no. 8, pp. 4640–4645, Aug. 2014.
[73] G. Sebald, E. Lefeuvre, and D. Guyomar, "Pyroelectric energy conversion: Optimization principles," *IEEE Trans. Ultrason. Ferroelectr. Freq. Control*, vol. 55, no. 3, pp. 538–551, Mar. 2008.
[74] J. P. Carmo, L. M. Goncalves, and J. H. Correia, "Thermoelectric Microconverter for Energy Harvesting Systems," *IEEE Trans. Ind. Electron.*, vol. 57, no. 3, pp. 861–867, Mar. 2010.
[75] J. B. Herzog, M. W. Knight, and D. Natelson, "Thermoplasmonics: Quantifying Plasmonic Heating in Single Nanowires," *Nano Lett.*, vol. 14, no. 2, pp. 499–503, Feb. 2014.
[76] M. R. Watts, M. J. Shaw, and G. N. Nielson, "Optical resonators: Microphotonic thermal imaging," *Nat. Photonics*, vol. 1, no. 11, pp. 632–634, Nov. 2007.
[77] J. Zhu, S. Ozdemir, and L. Yang, "Infrared light detection using a whispering-gallery-mode optical microcavity," *Appl. Phys. Lett.*, vol. 104, no. 17, p. 171114, Apr. 2014.
[78] T. W. Kenny, W. J. Kaiser, S. B. Waltman, and J. K. Reynolds, "Novel infrared detector based on a tunneling displacement transducer," *Appl. Phys. Lett.*, vol. 59, no. 15, pp. 1820–1822, Oct. 1991.
[79] F. Zhang *et al.*, "Infrared Detection Based on Localized Modification of Morpho Butterfly Wings," *Adv. Mater.*, vol. 27, no. 6, pp. 1077–1082, Feb. 2015.
[80] H. Zhu, F. Yi, and E. Cubukcu, "Plasmonic metamaterial absorber for broadband manipulation of mechanical resonances," *Nat. Photonics*, vol. 10, no. 11, pp. 709–714, Nov. 2016.
[81] J. R. Barnes *et al.*, "A femtojoule calorimeter using micromechanical sensors," *Rev. Sci. Instrum.*, vol. 65, no. 12, pp. 3793–3798, Dec. 1994.
[82] J. Lai, T. Perazzo, Z. Shi, and A. Majumdar, "Optimization and performance of high-resolution micro-optomechanical thermal sensors," *Sens. Actuators Phys.*, vol. 58, no. 2, pp. 113–119, Feb. 1997.
[83] R. Lefevre *et al.*, "Numerical study of bimetallic actuated micro-membrane with large deformations," *J. Micromechanics Microengineering*, vol. 23, no. 1, p. 015011, 2013.
[84] F. Yi, H. Zhu, J. C. Reed, and E. Cubukcu, "Plasmonically Enhanced Thermomechanical Detection of Infrared Radiation," *Nano Lett.*, p. 130320090705008, Mar. 2013.
[85] J. Agustí Batlle and G. Abadal Berini, *Nonlinear micro/nano-optomechanical oscillators for energy transduction from IR sources*. Universitat Autònoma de Barcelona, 2015.
[86] G. A. Magel, "Integrated optic devices using micromachined metal membranes," in *Proc. SPIE 2686, Integrated Optics and Microstructures III,* 1996, vol. 2686, pp. 54–63.
[87] M. Toda, T. Ono, F. Liu, and I. Voiculescu, "Evaluation of bimaterial cantilever beam for heat sensing at atmospheric pressure," *Rev. Sci. Instrum.*, vol. 81, no. 5, p. 055104, May 2010.
[88] R. J. Roark and W. C. Young, *Formulas for Stress and Strain*, 5 ed. McGraw-Hill, 1975.
[89] M. Manna, F. Magistrali, M. Maini, and D. Reichenbach, "Finite element method applied to stress simulation of high power 980nm pump lasers," *Microelectron. Reliab.*, vol. 37, no. 10–11, pp. 1667–1670, Oct. 1997.
[90] W. M. Haynes, Ed., *CRC Handbook of Chemistry and Physics*, 97 edition. CRC Press, 2016.
[91] "WebElements Periodic Table»Young's modulus»periodicity." [Online]. Available: https://www.webelements.com/periodicity/youngs_modulus/.

[92] "WebElements Periodic Table»Linear expansion coefficient»periodicity." [Online]. Available: https://www.webelements.com/periodicity/coeff_thermal_expansion/.
[93] "Using Perfectly Matched Layers and Scattering Boundary Conditions for Wave Electromagnetics Problems," *COMSOL Multiphysics©*. .
[94] J. Kischkat *et al.*, "Mid-infrared optical properties of thin films of aluminum oxide, titanium dioxide, silicon dioxide, aluminum nitride, and silicon nitride," *Appl. Opt.*, vol. 51, no. 28, pp. 6789–6798, Oct. 2012.
[95] "WebElements Periodic Table»Electrical resistivity»periodicity." [Online]. Available: https://www.webelements.com/periodicity/electrical_resistivity/.
[96] S. Franssila, *Introduction to Microfabrication*. John Wiley & Sons, 2010.
[97] P. Eriksson, J. Y. Andersson, and G. Stemme, "Thermal characterization of surface-micromachined silicon nitride membranes for thermal infrared detectors," *J. Microelectromechanical Syst.*, vol. 6, no. 1, pp. 55–61, Mar. 1997.
[98] "Uncooled Thermal Imaging Arrays, Systems, and Applications | (2001) | Kruse | Publications | Spie." [Online]. Available: https://spie.org/publications/book/415351?SSO=1. [Accessed: 29-Nov-2017].
[99] B. Feng, Z. Li, and X. Zhang, "Prediction of size effect on thermal conductivity of nanoscale metallic films," *Thin Solid Films*, vol. 517, no. 8, pp. 2803–2807, Feb. 2009.
[100] Y. Shiping and J. Peixue, "Thermal conductivity of nanoscale thin nickel films," *Prog. Nat. Sci.*, vol. 15, no. 10, pp. 922–929, Oct. 2005.
[101] E. Majorana and Y. Ogawa, "Mechanical thermal noise in coupled oscillators," *Phys. Lett. A*, vol. 233, no. 3, pp. 162–168, Aug. 1997.
[102] A. Hajati, "Ultra wide-bandwidth micro energy harvester," Thesis, Massachusetts Institute of Technology, 2011.
[103] K. E. Petersen, "Silicon as a mechanical material," *Proc. IEEE*, vol. 70, no. 5, pp. 420–457, May 1982.
[104] L. P. Boivin, "Thin-Film Laser-to-Fiber Coupler," *Appl. Opt.*, vol. 13, no. 2, pp. 391–395, Feb. 1974.
[105] M. J. Wale and C. Edge, "Self-aligned flip-chip assembly of protonic devices with electrical and optical connections," *IEEE Trans. Compon. Hybrids Manuf. Technol.*, vol. 13, no. 4, pp. 780–786, Dec. 1990.
[106] S. Kaneko *et al.*, "Novel fiber alignment method using a partially metal-coated fiber in a silicon V-groove," *IEEE Photonics Technol. Lett.*, vol. 12, no. 6, pp. 645–647, Jun. 2000.
[107] A. Priyadarshi, L. H. Fen, S. G. Mhaisalkar, V. Kripesh, and A. K. Asundi, "Fiber misalignment in silicon V-groove based optical modules," *Opt. Fiber Technol.*, vol. 12, no. 2, pp. 170–184, Apr. 2006.
[108] P. F. Heidrich, J. S. Harper, E. G. Lean, and H. N. Yu, "High density multichannel optical waveguides with integrated couplers," in *Electron Devices Meeting, 1975 International*, 1975, pp. 602–603.
[109] W.-T. Tsang, C.-C. Tseng, and S. Wang, "Optical Waveguides Fabricated by Preferential Etching," *Appl. Opt.*, vol. 14, no. 5, pp. 1200–1206, May 1975.
[110] Y. Kokubun, T. Baba, and K. Iga, "Silicon optical printed circuit board for three-dimensional integrated optics," *Electron. Lett.*, vol. 21, no. 11, pp. 508–509, May 1985.
[111] S. Chen and J. T. Boyd, "Integrated optical beam splitters formed in glass channel

waveguides having variable weighting as determined by mask dimensions," *IEEE J. Quantum Electron.*, vol. 18, no. 7, pp. 1072–1077, Jul. 1982.
[112] R. Narendra and J. N. McMullin, "Single-mode, phosphorus-doped silica waveguides in silicon V-grooves," *IEEE Photonics Technol. Lett.*, vol. 5, no. 1, pp. 43–46, Jan. 1993.
[113] S. Kumar, R. I. MacDonald, and J. N. McMullin, "Low-loss multimode polymer waveguides with serial out-of-plane taps," 1992, p. FA8.
[114] R. Narendra, I. N. McMullin, B. P. Keyworth, and R. I. MacDonald, "Dispensed Dual-polymer Waveguides In Silicon V-grooves," in *Optical Microwave Interactions/Visible Semiconductor Lasers/Impact of Fiber Nonlinearities on Lightwave Systems/Hybrid Optoelectronic Integration and Packaging/Gigabit Networks., LEOS 1993 Summer Topi*, 1993, pp. H39–H40.
[115] A. D'Alessandro, B. D. Donisi, R. Beccherelli, and R. Asquini, "Nematic Liquid Crystal Optical Channel Waveguides on Silicon," *IEEE J. Quantum Electron.*, vol. 42, no. 10, pp. 1084–1090, Oct. 2006.
[116] B. Bellini and R. Beccherelli, "Modelling, design and analysis of liquid crystal waveguides in preferentially etched silicon grooves," *J. Phys. Appl. Phys.*, vol. 42, no. 4, p. 045111, 2009.
[117] R. Asquini *et al.*, "Realization of a Liquid Crystal Electrically Controlled Optical Waveguide on Micromachined Silicon," *Mol. Cryst. Liq. Cryst.*, vol. 500, no. 1, pp. 23–30, Mar. 2009.
[118] A. d'Alessandro, R. Asquini, M. Trotta, G. Gilardi, R. Beccherelli, and I. C. Khoo, "All-optical intensity modulation of near infrared light in a liquid crystal channel waveguide," *Appl. Phys. Lett.*, vol. 97, no. 9, p. 093302, Aug. 2010.
[119] D. Donisi *et al.*, "A Switchable Liquid-Crystal Optical Channel Waveguide on Silicon," *IEEE J. Quantum Electron.*, vol. 46, no. 5, pp. 762–768, May 2010.
[120] D. C. Zografopoulos, R. Asquini, E. E. Kriezis, A. d'Alessandro, and R. Beccherelli, "Guided-wave liquid-crystal photonics," *Lab. Chip*, vol. 12, no. 19, pp. 3598–3610, 2012.
[121] T.-J. Wang, C.-K. Chaung, W.-J. Li, T.-J. Chen, and B.-Y. Chen, "Electrically Tunable Liquid-Crystal-Core Optical Channel Waveguide," *J. Light. Technol.*, vol. 31, no. 22, pp. 3570–3574, Nov. 2013.
[122] P. M. Pelosi, P. Vandenbulcke, C. D. W. Wilkinson, and R. M. De La Rue, "Propagation characteristics of trapezoidal cross-section ridge optical waveguides: an experimental and theoretical investigation," *Appl. Opt.*, vol. 17, no. 8, pp. 1187–1193, Apr. 1978.
[123] J. G. Gallagher, "Mode dispersion of trapezoidal cross-section dielectric optical waveguides by the effective-index method," *Electron. Lett.*, vol. 15, no. 23, pp. 734–736, Nov. 1979.
[124] T. Miyamoto, "Numerical analysis of a rib optical waveguide with trapezoidal cross section," *Opt. Commun.*, vol. 34, no. 1, pp. 35–38, Jul. 1980.
[125] G. Yue-Jin, L. De-Jun, and A. D. Klemm, "Numerical investigation of a trapezoidal cross-section ridge optical waveguide," *Numer. Methods Partial Differ. Equ.*, vol. 12, no. 3, pp. 307–314, May 1996.
[126] Q. Zhao, Y. Huang, R. Torun, S. Rahman, T. C. Atasever, and O. Boyraz, "Numerical investigation of silicon nitride trench waveguide," in *SPIE*, 2015, vol. 9586, p. 95860O–95860O–8.
[127] I. H. Malitson, "Interspecimen Comparison of the Refractive Index of Fused Silica," *J.*

Opt. Soc. Am., vol. 55, no. 10, pp. 1205–1209, Oct. 1965.
[128] H. Seidel, L. Csepregi, A. Heuberger, and H. Baumgärtel, "Anisotropic Etching of Crystalline Silicon in Alkaline Solutions II . Influence of Dopants," *J. Electrochem. Soc.*, vol. 137, no. 11, pp. 3626–3632, Nov. 1990.
[129] B. Kloeck, S. D. Collins, N. F. de Rooij, and R. L. Smith, "Study of electrochemical etch-stop for high-precision thickness control of silicon membranes," *IEEE Trans. Electron Devices*, vol. 36, no. 4, pp. 663–669, Apr. 1989.
[130] F. P. Payne and J. P. R. Lacey, "A theoretical analysis of scattering loss from planar optical waveguides," *Opt. Quantum Electron.*, vol. 26, no. 10, pp. 977–986, Oct. 1994.
[131] K. Wörhoff, A. Driessen, P. V. Lambeck, L. T. H. Hilderink, P. W. C. Linders, and T. J. A. Popma, "Plasma enhanced chemical vapor deposition silicon oxynitride optimized for application in integrated optics," *Sens. Actuators Phys.*, vol. 74, no. 1–3, pp. 9–12, Apr. 1999.
[132] N. Daldosso *et al.*, "Fabrication and optical characterization of thin two-dimensional Si3N4 waveguides," *Mater. Sci. Semicond. Process.*, vol. 7, no. 4–6, pp. 453–458, 2004.
[133] A. Melloni *et al.*, "TriPleX: A new concept in optical waveguiding," in *13th Eur. Conf. Integrated Optics (ECIO), Copenhagen, Denmark*, 2007.
[134] J. S. Levy, A. Gondarenko, M. A. Foster, A. C. Turner-Foster, A. L. Gaeta, and M. Lipson, "CMOS-compatible multiple-wavelength oscillator for on-chip optical interconnects," *Nat. Photonics*, vol. 4, no. 1, pp. 37–40, Jan. 2010.
[135] K. Ikeda, R. E. Saperstein, N. Alic, and Y. Fainman, "Thermal and Kerr nonlinear properties of plasma-deposited silicon nitride/ silicon dioxide waveguides," *Opt. Express*, vol. 16, no. 17, pp. 12987–12994, Aug. 2008.
[136] G. P. Agrawal, *Nonlinear Fiber Optics*. Academic Press, 2007.
[137] C.-Y. Tai, J. S. Wilkinson, N. M. Perney, M. C. Netti, and J. J. Baumberg, "Self-phase modulation induced spectral broadening of ultrashort laser pulses in tantalum pentoxide (Ta) rib waveguide," 2003.
[138] J. Levy, "Integrated Nonlinear Optics In Silicon Nitride Waveguides And Resonators," Ph.D. dissertation, Cornell Univ., Ithaca, NY, USA, 2011.
[139] P. N. Kean, K. Smith, and W. Sibbett, "Spectral and temporal investigation of self-phase modulation and stimulated Raman scattering in a single-mode optical fibre," *Optoelectron. IEE Proc. J*, vol. 134, no. 3, pp. 163–170, Jun. 1987.
[140] K. Ikeda, R. E. Saperstein, N. Alic, and Y. Fainman, "Thermal and Kerr nonlinear properties of plasma-deposited silicon nitride/ silicon dioxide waveguides," *Opt. Express*, vol. 16, no. 17, pp. 12987–12994, Aug. 2008.
[141] A. Boskovic, L. Gruner-Nielsen, O. A. Levring, S. V. Chernikov, and J. R. Taylor, "Direct continuous-wave measurement of n2 in various types of telecommunication fiber at 155 μm," *Opt. Lett.*, vol. 21, no. 24, pp. 1966–1968, Dec. 1996.
[142] M.-C. Tien, J. F. Bauters, M. J. R. Heck, D. J. Blumenthal, and J. E. Bowers, "Ultra-low loss Si_3N_4 waveguides with low nonlinearity and high power handling capability," *Opt. Express*, vol. 18, no. 23, pp. 23562–23568, Nov. 2010.
[143] K. Ikeda, R. E. Saperstein, N. Alic, and Y. Fainman, "Thermal and Kerr nonlinear properties of plasma-deposited silicon nitride/ silicon dioxide waveguides," *Opt. Express*, vol. 16, no. 17, p. 12987, Aug. 2008.
[144] C. J. Krückel, A. Fülöp, T. Klintberg, J. Bengtsson, P. A. Andrekson, and V. Torres-

Company, “Linear and nonlinear characterization of low-stress high-confinement silicon-rich nitride waveguides,” *Opt. Express*, vol. 23, no. 20, pp. 25827–25837, Oct. 2015.
[145] M. Dinu, F. Quochi, and H. Garcia, “Third-order nonlinearities in silicon at telecom wavelengths,” *Appl. Phys. Lett.*, vol. 82, no. 18, pp. 2954–2956, May 2003.
[146] D. T. H. Tan, K. Ikeda, P. C. Sun, and Y. Fainman, “Group velocity dispersion and self phase modulation in silicon nitride waveguides,” *Appl. Phys. Lett.*, vol. 96, no. 6, p. 061101, Feb. 2010.
[147] T. M. Monro and H. Ebendorff-Heidepriem, “Progress in Microstructured Optical Fibers,” *Annu. Rev. Mater. Res.*, vol. 36, no. 1, pp. 467–495, 2006.
[148] J. P. Epping *et al.*, “High confinement, high yield Si3N4 waveguides for nonlinear optical applications,” *Opt. Express*, vol. 23, no. 2, pp. 642–648, Jan. 2015.
[149] K. Luke, A. Dutt, C. B. Poitras, and M. Lipson, “Overcoming Si_3N_4 film stress limitations for high quality factor ring resonators,” *Opt. Express*, vol. 21, no. 19, pp. 22829–22833, Sep. 2013.
[150] Y. Huang, *Integrated optical signal processing based on optical waveguides and wavefront-engineered planar devices*. Irvine, Calif: University of California, Irvine, 2014.
[151] A. G. Griffith *et al.*, “Silicon-chip mid-infrared frequency comb generation,” *Nat. Commun.*, vol. 6, p. 6299, Feb. 2015.
[152] Y. Huang *et al.*, “Quasi-phase matching in SOI and SOS based parametric wavelength converters,” 2011, vol. 8120, p. 81200F–81200F–7.
[153] M. L. Juan, M. Righini, and R. Quidant, “Plasmon nano-optical tweezers,” *Nat. Photonics*, vol. 5, no. 6, pp. 349–356, Jun. 2011.
[154] A. J. Haes and R. P. V. Duyne, “Preliminary studies and potential applications of localized surface plasmon resonance spectroscopy in medical diagnostics,” *Expert Rev. Mol. Diagn.*, vol. 4, no. 4, pp. 527–537, Jul. 2004.
[155] B. P. Rand, P. Peumans, and S. R. Forrest, “Long-range absorption enhancement in organic tandem thin-film solar cells containing silver nanoclusters,” *J. Appl. Phys.*, vol. 96, no. 12, pp. 7519–7526, Dec. 2004.
[156] S. Pillai, K. R. Catchpole, T. Trupke, and M. A. Green, “Surface plasmon enhanced silicon solar cells,” *J. Appl. Phys.*, vol. 101, no. 9, p. 093105, May 2007.
[157] S. Lal, S. Link, and N. J. Halas, “Nano-optics from sensing to waveguiding,” *Nat. Photonics*, vol. 1, no. 11, pp. 641–648, Nov. 2007.
[158] X.-M. Qian and S. M. Nie, “Single-molecule and single-nanoparticle SERS: from fundamental mechanisms to biomedical applications,” *Chem. Soc. Rev.*, vol. 37, no. 5, p. 912, 2008.
[159] S. M. Adams *et al.*, “Non-lithographic SERS Substrates: Tailoring Surface Chemistry for Au Nanoparticle Cluster Assembly,” *Small*, vol. 8, no. 14, pp. 2239–2249, Jul. 2012.
[160] M. Kauranen and A. V. Zayats, “Nonlinear plasmonics,” *Nat. Photonics*, vol. 6, no. 11, pp. 737–748, Nov. 2012.
[161] sudheesh palengara and C. Keloth, “Metal Nanoparticle Induced Enhancement in Third-Order Optical Nonlinearity of Phenylhydrazone/PMMA thin films,” in *International Conference on Fibre Optics and Photonics*, 2012, p. TPo.43.
[162] V. Singh and P. Aghamkar, “Surface plasmon enhanced third-order optical nonlinearity of Ag nanocomposite film,” *Appl. Phys. Lett.*, vol. 104, no. 11, p. 111112,

Mar. 2014.
[163] M. R. Parida, C. Vijayan, C. S. Rout, C. S. S. Sandeep, and R. Philip, “Enhanced optical nonlinearity in β-AgVO3 nanobelts on decoration with Ag nanoparticles,” *Appl. Phys. Lett.*, vol. 100, no. 12, p. 121119, Mar. 2012.
[164] Y. Huang, Q. Zhao, L. Kamyab, A. Rostami, F. Capolino, and O. Boyraz, “Sub-micron silicon nitride waveguide fabrication using conventional optical lithography,” in *Advanced Photonics for Communications*, 2014, p. JT3A.27.
[165] A. Ashkin, “Acceleration and Trapping of Particles by Radiation Pressure,” *Phys. Rev. Lett.*, vol. 24, no. 4, pp. 156–159, Jan. 1970.
[166] D. G. Grier, “A revolution in optical manipulation,” *Nature*, vol. 424, no. 6950, pp. 810–816, Aug. 2003.
[167] M. P. MacDonald, G. C. Spalding, and K. Dholakia, “Microfluidic sorting in an optical lattice,” *Nature*, vol. 426, no. 6965, pp. 421–424, Nov. 2003.
[168] A. N. Grigorenko, N. W. Roberts, M. R. Dickinson, and Y. Zhang, “Nanometric optical tweezers based on nanostructured substrates,” *Nat. Photonics*, vol. 2, no. 6, pp. 365–370, Jun. 2008.
[169] A. Ashkin, J. M. Dziedzic, J. E. Bjorkholm, and S. Chu, “Observation of a single-beam gradient force optical trap for dielectric particles,” *Opt. Lett.*, vol. 11, no. 5, pp. 288–290, May 1986.
[170] R. Dasgupta, S. Ahlawat, P. K. Gupta, J. Xavier, and J. Joseph, “Optical trapping with low numerical aperture objective lens,” in *Photonics Global Conference (PGC), 2012*, 2012, pp. 1–4.
[171] R. Dasgupta, S. Ahlawat, and P. K. Gupta, “Trapping of micron-sized objects at a liquid–air interface,” *J. Opt. Pure Appl. Opt.*, vol. 9, no. 8, pp. S189–S195, 2007.
[172] Y. Harada and T. Asakura, “Radiation forces on a dielectric sphere in the Rayleigh scattering regime,” *Opt. Commun.*, vol. 124, no. 5–6, pp. 529–541, Mar. 1996.
[173] A. H. J. Yang, S. D. Moore, B. S. Schmidt, M. Klug, M. Lipson, and D. Erickson, “Optical manipulation of nanoparticles and biomolecules in sub-wavelength slot waveguides,” *Nature*, vol. 457, no. 7225, pp. 71–75, Jan. 2009.
[174] D. Erickson, X. Serey, Y.-F. Chen, and S. Mandal, “Nanomanipulation using near field photonics,” *Lab. Chip*, vol. 11, no. 6, pp. 995–1009, Feb. 2011.
[175] M. Soltani *et al.*, “Nanophotonic trapping for precise manipulation of biomolecular arrays,” *Nat. Nanotechnol.*, vol. 9, no. 6, pp. 448–452, Jun. 2014.
[176] S. Kühn *et al.*, “Loss-based optical trap for on-chip particle analysis,” *Lab. Chip*, vol. 9, no. 15, pp. 2212–2216, Aug. 2009.
[177] P.-T. Lin, H.-Y. Chu, T.-W. Lu, and P.-T. Lee, “Trapping particles using waveguide-coupled gold bowtie plasmonic tweezers,” *Lab Chip*, vol. 14, no. 24, pp. 4647–4652, 2014.
[178] W. Zhang, L. Huang, C. Santschi, and O. J. F. Martin, “Trapping and Sensing 10 nm Metal Nanoparticles Using Plasmonic Dipole Antennas,” *Nano Lett.*, vol. 10, no. 3, pp. 1006–1011, Mar. 2010.
[179] M. Righini, P. Ghenuche, S. Cherukulappurath, V. Myroshnychenko, F. J. García de Abajo, and R. Quidant, “Nano-optical Trapping of Rayleigh Particles and Escherichia coli Bacteria with Resonant Optical Antennas,” *Nano Lett.*, vol. 9, no. 10, pp. 3387–3391, Oct. 2009.

[180] P. Hansen, Y. Zheng, J. Ryan, and L. Hesselink, "Nano-Optical Conveyor Belt, Part I: Theory," *Nano Lett.*, vol. 14, no. 6, pp. 2965–2970, Jun. 2014.
[181] Y. Zheng, J. Ryan, P. Hansen, Y.-T. Cheng, T.-J. Lu, and L. Hesselink, "Nano-Optical Conveyor Belt, Part II: Demonstration of Handoff Between Near-Field Optical Traps," *Nano Lett.*, vol. 14, no. 6, pp. 2971–2976, Jun. 2014.
[182] G. Wang, Z. Ying, H. Ho, Y. Huang, N. Zou, and X. Zhang, "Nano-optical conveyor belt with waveguide-coupled excitation," *Opt. Lett.*, vol. 41, no. 3, pp. 528–531, Feb. 2016.
[183] B. S. Schmidt, A. H. Yang, D. Erickson, and M. Lipson, "Optofluidic trapping and transport on solid core waveguides within a microfluidic device," *Opt. Express*, vol. 15, no. 22, p. 14322, 2007.
[184] S. Mandal and D. Erickson, "Optofluidic transport in liquid core waveguiding structures," *Appl. Phys. Lett.*, vol. 90, no. 18, p. 184103, Apr. 2007.
[185] X. Fan and I. M. White, "Optofluidic microsystems for chemical and biological analysis," *Nat. Photonics*, vol. 5, no. 10, pp. 591–597, Oct. 2011.
[186] M. Chamanzar, Z. Xia, S. Yegnanarayanan, and A. Adibi, "Hybrid integrated plasmonic-photonic waveguides for on-chip localized surface plasmon resonance (LSPR) sensing and spectroscopy," *Opt. Express*, vol. 21, no. 26, p. 32086, Dec. 2013.
[187] Y. Luo *et al.*, "On-Chip Hybrid Photonic–Plasmonic Light Concentrator for Nanofocusing in an Integrated Silicon Photonics Platform," *Nano Lett.*, vol. 15, no. 2, pp. 849–856, Feb. 2015.
[188] Y. Huang, Q. Zhao, N. Sharac, R. Ragan, and O. Boyraz, "Highly nonlinear sub-micro silicon nitride trench waveguide coated with gold nanoparticles," in *SPIE*, 2015, vol. 9503, p. 95030H–95030H–8.
[189] W. H. Wright, G. J. Sonek, and M. W. Berns, "Radiation trapping forces on microspheres with optical tweezers," *Appl. Phys. Lett.*, vol. 63, no. 6, pp. 715–717, Aug. 1993.
[190] B. J. Roxworthy *et al.*, "Application of Plasmonic Bowtie Nanoantenna Arrays for Optical Trapping, Stacking, and Sorting," *Nano Lett.*, vol. 12, no. 2, pp. 796–801, 2011.
[191] T. R. Jensen, M. D. Malinsky, C. L. Haynes, and R. P. Van Duyne, "Nanosphere Lithography: Tunable Localized Surface Plasmon Resonance Spectra of Silver Nanoparticles," *J. Phys. Chem. B*, vol. 104, no. 45, pp. 10549–10556, 2000.
[192] A. J. Haes, C. L. Haynes, A. D. McFarland, G. C. Schatz, R. P. Van Duyne, and S. Zou, "Plasmonic Materials for Surface-Enhanced Sensing and Spectroscopy," *MRS Bull.*, vol. 30, no. 05, pp. 368–375, May 2005.
[193] B. T. Draine, "The discrete-dipole approximation and its application to interstellar graphite grains," *Astrophys. J.*, vol. 333, pp. 848–872, Oct. 1988.
[194] O. M. Maragò, P. H. Jones, P. G. Gucciardi, G. Volpe, and A. C. Ferrari, "Optical trapping and manipulation of nanostructures," *Nat. Nanotechnol.*, vol. 8, no. 11, pp. 807–819, Nov. 2013.
[195] S. Albaladejo, M. I. Marqués, M. Laroche, and J. J. Sáenz, "Scattering Forces from the Curl of the Spin Angular Momentum of a Light Field," *Phys. Rev. Lett.*, vol. 102, no. 11, p. 113602, Mar. 2009.
[196] A. J. Cox, A. J. DeWeerd, and J. Linden, "An experiment to measure Mie and Rayleigh total scattering cross sections," *Am. J. Phys.*, vol. 70, no. 6, pp. 620–625, Jun. 2002.
[197] M. L. Juan, R. Gordon, Y. Pang, F. Eftekhari, and R. Quidant, "Self-induced back-action

optical trapping of dielectric nanoparticles," *Nat. Phys.*, vol. 5, no. 12, pp. 915–919, Dec. 2009.